การเตรียมคอลลอยด์และฟิล์มบางของ $LiCo_{1-x}Mn_xO_2$

นายกรุณา นนทวิศรุต

4972210223

PREPARATION OF COLLOID AND THIN FILM OF $LiCo_{1-x}Mn_xO_2$

Mr. Karuna Nonthawissarut

A Thesis Submitted in Partial Fulfillment of the Requirements

for the Degree of Master of Science Program in Petrochemistry and Polymer Science

Faculty of Science

Chulalongkorn University

Academic Year 2008

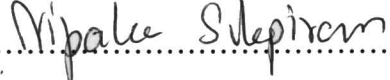Copyright of Chulalongkorn University

512102

Thesis Title   PREPARATION OF COLLOID AND THIN FILM OF
                   $LiCo_{1-x}Mn_xO_2$

By   Mr. Karuna Nonthawissarut

Field of Study   Petrochemistry and Polymer Science

Advisor   Nipaka Sukpirom, Ph.D.
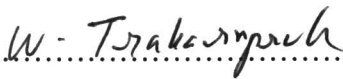
Accepted by the Faculty of Science, Chulalongkorn University in Partial Fulfillment of the Requirements for the Master's Degree

……………………………………..Dean of the Faculty of Science

(Professor Supot Hannongbua, Dr.rer.nat.)

THESIS COMMITTEE

……………………………………..Chairman

(Associate Professor Sirirat Kokpol, Ph.D.)

……………………………………..Advisor

(Nipaka Sukpirom, Ph.D.)

……………………………………..Examiner

(Associate Professor Wimonrat Trakarnpruk, Ph.D.)

……………………………………..External Examiner

(Waret Veerasai, Dr.rer.nat.)

กรุณา นนทวิศรุต : การเตรียมคอลลอยด์และฟิล์มบางของ $LiCo_{1-x}Mn_xO_2$. (PREPARATION OF COLLOID AND THIN FILM OF $LiCo_{1-x}Mn_xO_2$) อ. ที่ปรึกษาวิทยานิพนธ์หลัก: อ.ดร.นิปกา สุขภิรมย์, 112 หน้า.

แมงกานีสโดปลิเทียมโคบอลต์ออกไซด์ $LiCo_{1-x}Mn_xO_2$ (x = 0.0 - 1.0) เตรียมได้ด้วยวิธีโซล เจล โดยมีกรดซิตริกเป็นตัวคีเลต (CAS) จากการตรวจสอบโครงสร้างด้วยเทคนิคการเลี้ยวเบนของ รังสีเอกซ์ (XRD) พบว่า เมื่อโดปแมงกานีสน้อยกว่าหรือเท่ากับ 0.2 (x = 0.0 - 0.2) แล้วเผาที่ อุณหภูมิ 700 องศาเซลเซียส เป็นเวลา 6 ชั่วโมง จะได้สารประกอบ $LiCo_{1-x}Mn_xO_2$ (LCMx) ที่เป็น เฟสเดี่ยว การโดปแมงกานีสในสารประกอบออกไซด์นี้ทำให้ขนาดผลึกมีขนาดลดลงอย่างชัดเจน สารประกอบออกไซด์ที่เป็นเฟสเดี่ยวถูกเปลี่ยนให้อยู่ในรูปของโปรตอน (HCMx) โดยการกวนผง LCMx ในสารละลายกรดเป็นเวลานาน 24 ชั่วโมง คอลลอยด์ของสารเฟสเดี่ยว LCMx เตรียมได้จาก การกระจายแผ่นโครงสร้างด้วยอัลตราซาวด์ในสารละลายปรับสภาพพื้นผิวเททระบิวทิล แอมโมเนียมไฮดรอกไซด์ (TBAOH) ภาวะที่เหมาะสมที่สุดในการเตรียมคอลลอยด์ที่เสถียร คือ อัตราส่วนโดยโมลของ TBAOH ต่อ HCMx เท่ากับ 1 และอัลตราซาวด์ที่ 125 วัตต์ เป็นเวลานาน 30 นาที กล้องจุลทรรศน์อิเล็กตรอนแบบส่องผ่าน (TEM) แสดงให้เห็นถึงการกระจายตัวของ สารประกอบออกไซด์ที่เป็นชั้นเมื่อผ่านกระบวนการกระจายแผ่นโครงสร้าง ในส่วนของของแข็งที่ กระจายตัวอยู่ในคอลลอยด์ ประกอบด้วยสารประกอบออกไซด์อนุภาคระดับนาโนและแผ่น โครงสร้างระดับนาโนของสารประกอบออกไซด์ที่กระจายตัว สามารถเตรียมฟิล์มบางหลายชั้นของ แมงกานีสโดปสารประกอบออกไซด์ที่เป็นชั้นและพอลิไดอัลลิลไดเมทิลไดแอมโมเนียมไอออน (PDAD) ได้เป็นผลสำเร็จในลักษณะชั้นต่อชั้นบนตัวรองรับด้วยวิธีจุ่มเคลือบ ภาวะที่เหมาะสมที่สุด ในการขึ้นรูปฟิล์มคือใช้สารละลาย PDAD 10 มิลลิโมลาร์ที่มีเกลือโซเดียมคลอไรด์เข้มข้น 0.5 โม ลาร์และเวลาในการขึ้นรูปเท่ากับ 10 นาที FT-IR สเปกตรัมแสดงให้เห็นว่ามี PDAD เป็น องค์ประกอบของคอมโพสิตฟิล์ม การวิเคราะห์ด้วยเทคนิคยูวี-วิซิเบิลแอบซอร์พชันสเปคโทรสโก ปี กล้องจุลทรรศน์แรงอะตอม (AFM) และ XRD แสดงให้เห็นถึงการโตของฟิล์มบางอย่าง สม่ำเสมอในลักษณะชั้นต่อชั้น

สาขาวิชา ปิโตรเคมีและวิทยาศาสตร์พอลิเมอร์ ลายมือชื่อนิสิต _____

ปีการศึกษา _____2551_____ ลายมือชื่อ อ. ที่ปรึกษาวิทยานิพนธ์หลัก _____

4972210223: MAJOR PETROCHEMISTRY AND POLYMER SCIENCE
KEYWORDS: LITHIUM COBALT OXIDE/MANGANESE-DOPING/ COLLOID/ THIN FILM/LAYAR-BY-LAYER TECHNIQUE.

KARUNA NONTHAWISSARUT: PREPARATION OF COLLOID AND THIN FILM OF $LiCo_{1-x}Mn_xO_2$. ADVISOR: NIPAKA SUKPIROM, Ph.D., 112 pp.

Mn-doped layered lithium cobalt oxides, $LiCo_{1-x}Mn_xO_2$ (x = 0.0 - 1.0), were synthesized by citric acid-assisted sol-gel method (CAS). Characterized by X-ray diffraction (XRD), the single-phased $LiCo_{1-x}Mn_xO_2$ (LCMx) was observed for Mn doping up to x = 0.2 using the calcinations temperature of 700 °C for 6 h. The Mn doping apparently led to the reduction of crystallite size. The single-phased oxides were converted into proton-exchanged HCMx by stirring LCMx powders in acid solution for 24 h. The colloidal suspensions of single-phased LCMx (x = 0.0, 0.1, and 0.2) were obtained by exfoliation in tetrabutylammonium hydroxide (TBAOH) using ultrasound irradiation. The optimum condition for preparing the stable colloid was using the mole ratio of TBA/HCMx = 1.0 and the ultrasonic processor with the setting at 125 W for 30 min. Transmission electron microscopy (TEM) was used to reveal the dispersion of the layer oxide particles by the exfoliation process. The solid parts in a colloidal suspension were characterized as the mixture of oxide nanoparticles and exfoliated oxide nanosheets. Multilayer thin films of Mn-doped layered oxides and poly(diallyldimethylammonium) (PDAD) ions were successfully deposited layer-by layer (LBL) onto substrates by dipping coat technique. The optimum condition for thin film preparation was using 10 mM PDAD solution containing 0.5 M NaCl and dipping time at 10 min. FT-IR spectrum indicated the presence of PDAD on the attained composite films. UV-Vis absorption spectroscopy, Atomic force microscope (AFM) and XRD analysis were used to indicate the LBL growth of the thin films.

Field of Study: <u>Petrochemistry and Polymer Science</u> Student's Signature Karuna Nonthawisarut

Academic Year: <u>2008</u> Advisor's Signature Nipaka Sukpirom

ACKNOWLEDGEMENTS

CONTENTS

LIST OF TABLES

LIST OF FIGURES

LIST OF SCHEMES

LIST OF ABBREVIATIONS

°C	Degree Celsius
μm	Micrometer
nm	Nanometer
rpm	Rounds per minute
Å	Angstrom unit
h	Hour or hours
min	Minute or minutes
wt%	Percent by weight
M	Molar
R.T.	Room temperature
XRD	X-ray diffraction
UV-Vis	Ultraviolet visible spectroscopy
TEM	Transmission electron microscopy
AFM	Atomic force microscopy
FT-IR	Fourier transform infrared spectroscopy
ICP-AES	Inductively coupled plasma-atomic emission spectroscopy
LCMx	$LiCo_{1-x}Mn_xO_2$; x is the molar ratio of Mn to Mn+Co
HCMx	Proton-exchanged form ($HCo_{1-x}Mn_xO_2$)
Up-HCMx	Upper phase of colloidal suspension of HCMx
Dep-HCMx	Deposited phase of HCMx after exfoliation process
LIB	Lithium ion battery
PDAD	Poly(diallyldimethylammonium chloride)
TBAOH	Tetrabutylammonium hydroxide
NTU	Nephelometric turbidity units
LBL	Layer-by-layer

CHAPTER I

INTRODUCTION

1.1   Background

Nowadays, electronic devices have been modified to smaller sizes, while maintains a high performance for convenient requirement of consumers. Therefore, materials and chemicals must be developed in order to achieve the highest efficiency and reduce the manufactured cost. Transition metal oxides have attracted much interest because of their possible use as electrode materials in electronic devices. Especially, lithiated transition metal oxides, such as $LiMnO_2$, $LiMn_2O_4$, $LiNiO_2$, $LiCoO_2$ etc. have been studied extensively, because of their potential use as cathode materials for lithium ion batteries [1]. Lithium ion batteries (LIB) has become the most attractive energy source for electronic products with their light weights and the greatest amounts of energy.
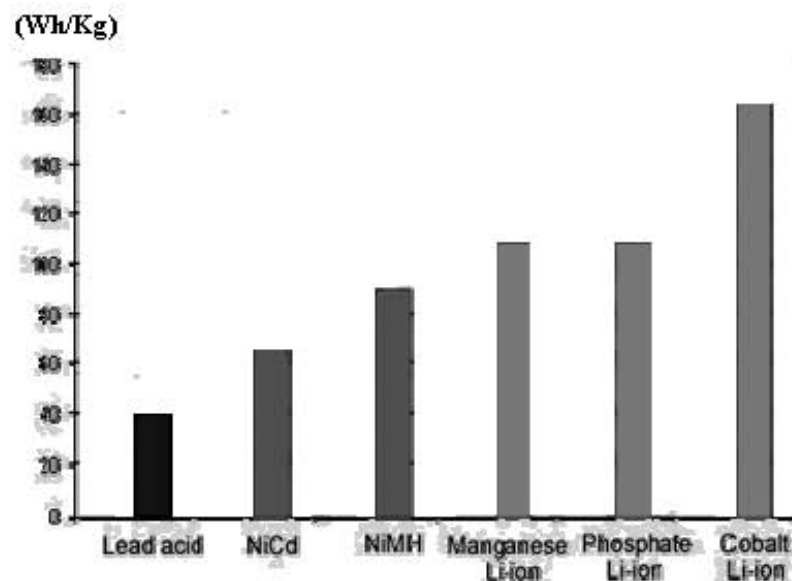
Figure 1.1 Energy densities of common battery chemistries [2].

Figure 1.1 compares the energy density of the three LIBs (Manganese Li-ion, Phosphate Li-ion and Cobalt Li-ion) and place them against the traditional lead acid,

nickel-cadmium (NiCd) and nickel-metal-hydride (NiMH). Cobalt LIB offers the highest energy, thus it is used in a small cell of portable electronic devices such as mobile phone, camera and notebook computers. The market for LIB has expanded rapidly because of the increase in demand for this electronics products. It is reported that the total sales of the cell in 2002 reached 6.5 billion dollars, and are more than 10 billion dollars in 2005 [3]. The project demands of LIB and other batteries for the world market are projected in Figure 1.2.
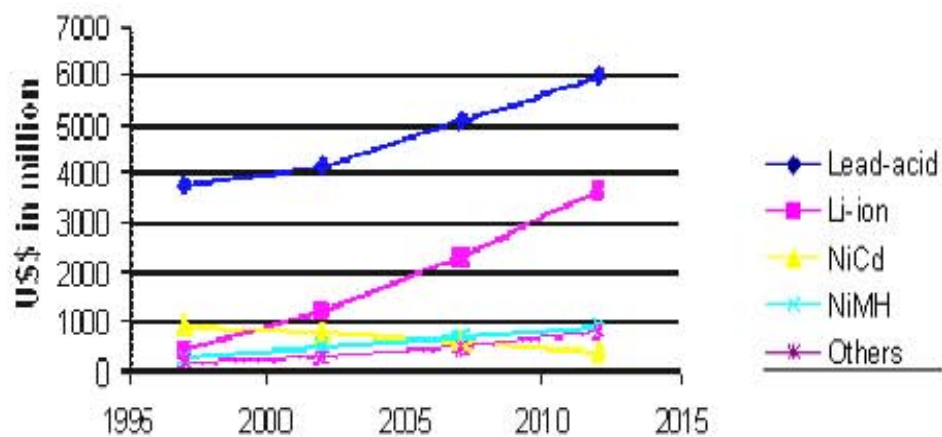
Figure 1.2 Projected demand for LIB and other secondary batteries [4].

Layered $LiCoO_2$ is the most studied cathode for LIB due to its characteristic properties, i.e. high voltage, good reversibility, high theoretical specific capacity [5-6]. Although the $LiCoO_2$ dominates the rechargeable LIB market, there is a limited availability of Co, which leads to a high price of LIB [7]. Furthermore Co is a rare element and toxic. Therefore, substitution of Co in $LiCoO_2$ with nontoxic and inexpensive transition metallic elements becomes an interesting issue. $LiCoO_2$ powders are usually prepared by solid state reaction of metal hydroxide, acetate or carbonates such as $LiOH$, Li_2CO_3 and $CoCO_3$ [8-9]. However, this method results to the powders with several disadvantages; irregular morphology, inhomogeneity, and larger particle size (ranging from 1-5 μm). Furthermore, high temperature and longer time of calcination are required to obtain the single-phased oxides. It has been reported that the performance of the battery depends on packing density and homogeneity of $LiCoO_2$ powders [10]. Thus, the preparation of submicron particles of $LiCoO_2$ with uniform morphology is desirable.

1.2 Literature reviews of $LiCoO_2$ and $LiCo_{1-x}M_xO_2$ synthesis

1.2.1 Synthesis of $LiCoO_2$

Several groups have reported the methods for $LiCoO_2$ synthesis. The most common route is the solid-state reaction (conventional method). Ganesan *et al.* [9] prepared $LiCoO_2$ by this method from the mixture of the Li_2CO_3 and $CoCO_3$. The mixture was calcined at 900 ^{o}C for 72 h to obtain the single-phased oxide. This method results to the average particle size with a diameter about 1.46 μm. Ding *et al.* [11] proposed a new gel route to synthesize $LiCoO_2$ by the radiated polymer gel (RPG) method. The pure phase of $LiCoO_2$ with the particle size about 2 μm was obtained at the calcination of 800°C for 8 h. Combustion method is another widely technique to prepare $LiCoO_2$. This process uses organic acids such as urea [12], diformyl hydrazine (DHF) [13] and starch [14] as a fuel during the formation process of oxide powders. The oxide powers showed the micro-particle size depending on a type of fuel and a condition of process. Chang *et al.* [15] prepared $LiCoO_2$ from the mixture of $Co(OH)_2$ and $LiOH\cdot H_2O$ in basic aqueous solution by hydrothermal and reflux reaction. The pure phase oxides were obtained at 130 ^{o}C for 48 h and exhibited a uniform particles size about 100 nm. Hanh *et al.* [6] prepared $LiCoO_2$ by sol-gel citrate method. The $LiCoO_2$ powder was synthesized from dissolving $LiNO_3$ and $Co(NO_3)_2$ in ethanol and using citric acid as a chelating agent. The single-phased oxides were obtained by preheating at 400 ^{o}C for 3 h and calcination at 700 ^{o}C for 12 h. The obtained $LiCoO_2$ has the average particle size of 100 nm and showed the paramagnetic property at room temperature. Peng *et al.* [16] synthesized $LiCoO_2$ by a sol-gel process. The gel was formed at 140 ^{o}C by mixing $Co(CH_3COO)_2$ and $LiCH_3COO$ with citric acid in ethylene glycol solution. Fine powder was produced by calcination at 350 – 750 ^{o}C for 10 h. The single-phased oxide was obtained at 550 ^{o}C for 10 h with the diameter of particles between 30 - 50 nm.

From literatures above, the sol-gel is a suitable method to prepare $LiCoO_2$, because of many advantages such as homogenous precursor mixture, ease at doping, short preparation period, low processing temperature and nanoparticle sized products [6, 16]. Thus in this research, sol-gel method was chosen as a method for $LiCoO_2$ and metal-doping $LiCoO_2$ synthesis.

1.2.2 Synthesis routes of $LiCo_{1-x}M_xO_2$

One of the modifications to improve its electrode performance is the substitution of Co with other metal ions which may stabilize the layered structure. Several researches have reported the application of metal doping in $LiCoO_2$. Julein et al. [17] prepared layered $LiCo_{0.4}Ni_{0.6}O_2$ by a sol-gel method using citric acid as a chelating agent. The single-phased oxide with micro-particles was obtained at at the calcination temperature of 700 °C for 4 h. Jin et al. [18] prepared Si-doped cobalt oxide; $LiCo_{1-x}Si_xO_2$ (x = 0.00 - 0.35) by the co-precipitation method. The stable single-phased oxides were found for Si-doping up to x = 0.2. The particle size decreases with the increase of Si content. The Si-doping leads to the lower impedance and better electrochemical performances of lithium cell. Khan et al. [19] synthesized $LiCo_{1-x}Al_xO_2$ (x = 0.0 - 0.7) by a sol-gel method using acrylic acid as a chelating agent. The Al-doping leads to the shrinkage of an interatomic distance within a CoO_2 layer and the increase of an interplanar distance between CoO_2 layers. Madhavi et al. [20] prepared $LiCo_{1-x}Cr_xO_2$ (x = 0.0 - 0.2 and 1) by a solid-state reaction. The Cr-doping layered $LiCoO_2$ of all samples showed the impuritie phases of LiOH and CoO. Gopukumar et al. [8] synthesized $LiCo_{1-x}Ti_xO_2$ (x = 0.0 - 0.5) by solid-state reaction. The single-phased oxides were found for Ti-doping up to x = 0.1. The initial charge and discharge capacities of $LiCo_{0.99}Ti_{0.01}O_2$ are higher of than those of $LiCoO_2$. Needham et al. [21] prepared layered $LiCo_{0.98}M_{0.02}O_2$ (M = Mo, V and Zr) by solid state reaction. All samples showed the secondary phases of molydates, Li_3VO_4 and Li_2ZrO_3. Julien et al. [22] synthesized $LiCo_{0.5}M_{0.5}O_2$ (M = Ni, Mg, Mn and Zn) by combustion method. Only XRD pattern of $LiCo_{0.5}Ni_{0.5}O_2$ presented the single-phased pattern showing a rhombohedral structure. Kim et al. [23] prepared $LiCo_{1-x}M_xO_2$ (x = 0.0 - 0.1; M = Mg and Zr) by sol-gel method using acrylic acid as a chelating agent. $LiCo_{1-x}Mg_xO_2$ (0.0 - 0.1) showed the pure phase. On the other hand, the pattern of $LiCo_{1-x}Zr_xO_2$ with x = 0.1 exhibited the impurity peaks of ZrO_2. $LiCoO_2$ doping with Mg and Zr were reported to improve charge-discharge cycling performance of the lithium cell. Caballero et al. [24] synthesized $LiCo_{1-x}Mn_xO_2$ (x = 0.0 and 0.2) by sol gel method using propionic acid as a chelating agent. Substitution of Co by Mn ions ($LiCo_{0.8}Mn_{0.2}O_2$) exhibited a good electrochemical performance as cathode in lithium cells. Waki et al. [25] prepared $LiCo_{1-x}Mn_xO_2$ (x = 0.0 - 0.5) by sol gel method using

citric acid as a chelating agent. The single-phased oxides were found for Mn-doping up to x = 0.2. The Mn-doping led to an improvement in cycle stability of the $LiCoO_2$.

Manganese has been considered to be a potential element with nontoxic nature. Partial substitution of Co by Mn has also been considered to enhance the stability of $LiCoO_2$ lattice [26] and affects the electrochemical properties such as an increase in capacity and in the cycling properties of the cell [24-25]. $LiMnO_2$ with a layered structure has attracted much attention due to its low cost, non-toxicity and high theoretical capacity. However, it has a main disadvantage, the cycle instability of Li-ion insertion and extraction [7, 27]. Thus, the preparation of Mn-doped layered $LiCoO_2$ with stability structure at high temperature is attractive.

1.3   Literature reviews of colloid and thin film preparation from intercalation-exfoliation process

The preparation of exfoliated colloids of layered compounds is a very interesting and important topic related to the production of organic-inorganic nanocomposites [28, 29] interstratified materials, high surface area catalysts and multilayers thin films [30]. In the last decade, thin films were widely studied because of their optical, electrochemical, electronic properties [31], as well as the applications in antifogging and self-cleaning merchandizes [32]. Several groups have reported the fabrication of multilayer films by the layer-by-layer (LBL) technique such as MnO_2 nanosheets [31-33], TiO_2 nanoparticles [34], titania nanosheets [35], clay materials [36], niobate and titanoniobate [37], metal disulfides [38], carbon nanotubes [39] and SnO_2 [40].

The preparation and characterization of colloid and thin film have been the topic of several literatures. Sukpirom and Lerner [28] prepared layered nanocomposites with poly(ethylene oxide), PEO, and poly(vinylpyrolidone), PVP, incorporated layers titanate $H_xTi_{2-x/4}\square_{x/4}O_4$ ($\square$ = Ti-vacancy). Colloidal titanates were obtained by exfoliation in aqueous solution of tetrabutylammonium hydroxide (TBAOH). Nanocomposites were prepared by adding aqueous polymer solutions to the colloids of exfoliated titanate sheets. In 2002 - 2003 [29, 41] they used ultrasound technique to assist the exfoliation process of titanate and layered tetratitanate.

Ultrasound technique enhances the rate of exfoliation of these layered titanates. After sonication, the dispersions of tetratitanate nanosheets were used as a precursor to prepare polymer nanocomposites.

Sasaki et al. [35, 42] prepared a multilayer titania ultrathin film by self-assembled layer-by-layer technique. The exfoliated titania nanosheets were obtained by shaking $H_{0.7}Ti_{0.825}\square_{0.175}O_4.H_2O$ in TBAOH at room temperature for 10 days. Multilayer ultrathin films were fabricated with poly(diallyldimethyl ammonium chloride) (PDDA) onto substrates. The films exhibited highly efficient optical absorption with a sharp peak at 266 nm and their UV-Vis spectra showed a progressive enhancement as a function of the deposition numbers.

Abe et al. [43] prepared thin film of a layered titanate by the exfoliation of $Cs_xTi_{(2-x/4)}\square_{x/4}O_4$. The exfoliation was carried out in TBAOH solution or ethylamine solution at room temperature for 24 h. Thin films composed of layered titanate were prepared by spin-coating technique.

Sasaki et al. prepared and characterized a multilayer ultrathin film by deposition of exfoliated MnO_2 nanosheets and poly(diallyldimethylammonium) (PDDA) [31] or aluminum polyoxocations $[AlO_4Al_{12}(OH)_{24}(H_2O)_{12}]^{7+}$ [33]. The colloidal suspension of MnO_2 nanosheets was obtained by dispersing $H_{0.13}$ $MnO_2.0.7H_2O$ in TBAOH solution for 10 days. Multilayer ultrathin films were exhibited characteristic absorption peak of MnO_2 nanosheet at 380 nm. A nearly linear enhancement of an absorbance at 380 nm was observed, indicating successful layer-by-layer growth. Furthermore, the multilayer films showed a very stable voltammogram involving reversible redox reaction of Mn^{III}/Mn^{IV}.

Zhang et al. [32] fabricated a multilayer thin film comprising negatively charged MnO_2 nanosheets and positively charged magnesium-aluminum layer double hydroxides (Mg-Al LDHs) sheets by electrostatic layer-by-layer adsorption technique. UV-Vis absorption spectra showed a characteristic MnO_2 sheets. And Mg-Al LDHs sheets can be deposited uniformly onto multilayer film. The resulting film will have potential applications in optical and electrochemical devices.

Prasad *et al.* [44] synthesized nanocomposites based on exfoliated $NbWO_6$ nanosheets and poly (N-methyl-2-ethynyl pyridinium iodide) (PNMe) or poly (N-octadecyl-2-ethynyl pyridinium bromide) (PNO) by exfoliation–reflocculation method. The colloidal suspension of $NbWO_6$ nanosheets was prepared by shaking of $HNbWO_6$ in aqueous solution of TBAOH for 3 days. A stable dispersion solution of $NbWO_6$ nanosheet was added to the PNMe or PNO solution in order to precipitate the nanocomposites. The products enhanced the thermal stability of the polymers.

Du *et al.* [45] prepared $KTiNbO_5$ nanosheets by a simple intercalation and exfoliation method. The colloidal suspension of exfoliated $KTiNbO_5$ nanosheets was obtained by mixing the $KTiNbO_5$ in an aqueous solution of TBAOH and stirring for 3 days. The particles have non-uniform morphology with sizes in the rage of 3-10 μm. They exhibited as a semiconductor with a wide gap about 3.2 eV.

Masuda *et al.* [46] developed an exfoliation process of layered structure Na_xCoO_2 (x=0.7) to prepare cobalt oxide sheets having nanometer-order thicknesses. Conceptual process for exfoliation-integration process is shown in Figure 1.3. Cobalt oxide sheets were obtained from $Na_{0.7}CoO_2$ powder after stirred in ethylamine solution for 10 days. The obtained upper colloid solution including a small amount of exfoliated sheet (< 10%) with the thickness and size of particles about 5 – 20 nm and 200 – 300 nm, respectively.
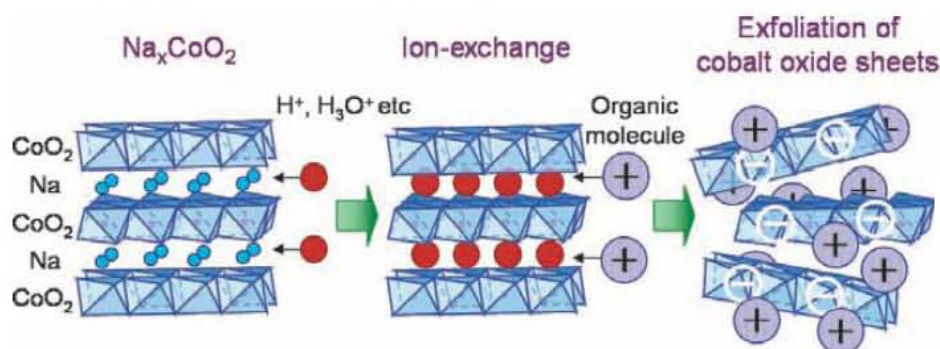
Figure 1.3 Conceptual process for exfoliation-integration process.

Kim *et al.* [36] prepared the colloid of exfoliated hectorite platelets through the process of coumarin dye intercalation by sonicating in water suspension. The colloidal suspension was composed of the exfoliated hectorite platelets and coumarin

dye with platelets about 10 - 40 nm width, 150 - 400 nm length, and 2 - 3 nm average thickness. It used as a precursor in order to prepare multilayered nanocomposite films derived of exfoliated hectorite platelets and poly(diallyldimethylammonium) chloride (PDAC) through electrostatic layer-by-layer assembly. The resulting films exhibited strong characteristic blue-green fluorescence due to coumarin dye molecules adhered to the exfoliated hectorite platelets.

Shiguihara et al. [30] reported the influence of the concentration of tetra(n-butyl)ammonium hydroxide (TBAOH) on the $H_2K_2Nb_6O_{17}$ exfoliation. A fixed amount of $H_2K_2Nb_6O_{17}$ was reacted with solutions containing various TBAOH concentrations (TBA^+/H^+-niobate molar ratios = 0.25, 0.50, 0.75 and 1.00). The deposited solids of samples have no organic species intercalated. The highest amount of exfoliated niobate particles was about 65 wt% when the TBA^+/H^+-niobate molar ratio was ≥ 0.50.

Ramachandran et al. [47] prepared the intercalation compounds of layered nikel dioxide and layered cobalt dioxide ($LiMO_2$; M = Ni, Co) with organocations. The compounds were obtained by reaction of lithiated hosts with persulfate aqueous solution, followed by treatment with desired organocations. These compounds were easily derived in a one- or two step reaction. The products were included pillaring structure of anilinium (basal repeat ~12 Å), dodecyltrimethylammonium (~27 Å), octadecyltrimethylammonium (~34 Å) and distearydimethylammonium (~41 Å) between oxide layers.

From literatures mentioned above, the stable colloidal suspension of exfoliated sheets and multilayer thin films of several metal oxides, metal disulfides, layers titanate, $H_{0.13}MnO_2.0.7H_2O$, $HNbWO_6$, $KTiNbO_5$, $Na_{0.7}CoO_2$, clay, $H_2K_2Nb_6O_{17}$ were prepared. However, colloidal suspension and thin films of layered $LiCoO_2$ and Mn-doped layered $LiCoO_2$ are not reported.

Thus in this research, $LiCo_{1-x}Mn_xO_2$ (x = 0.0 - 1.0) powders were synthesized by citric acid-assisted sol-gel method (CAS), and their characteristics in terms of the phase purity, crystallinity and particles size are described. The single-phased oxides were used as the precursors in order to prepared colloids and thin films. Multilayer

thin films were fabricated using Mn-doping cobalt oxide sheets and polycation by the layer-by-layer (LBL) technique. Furthermore, this is the first report of a stable colloid and multilayer films of layered cobalt oxides.

1.3   Objectives

1.3.1   To synthesize and characterize $LiCo_{1-x}Mn_xO_2$ (x = 0.0 - 1.0) by citric acid-assisted sol-gel method (CAS).

1.3.2   To prepare and characterize colloidal suspensions and thin film of $LiCo_{1-x}Mn_xO_2$.

CHAPTER II

THEORY

2.1 Structural features of LiCoO$_2$

LiCoO$_2$ possess the layered α-NaFeO$_2$-type structure of the rhombohedral symmetry with space group $\overline{R}3m$. This structure is described as a hexagonal cell setting with the unit cell parameters $a = 2.815$ Å and $c = 14.05$ Å [48]. The structure of this compound is shown in Figure 2.1.
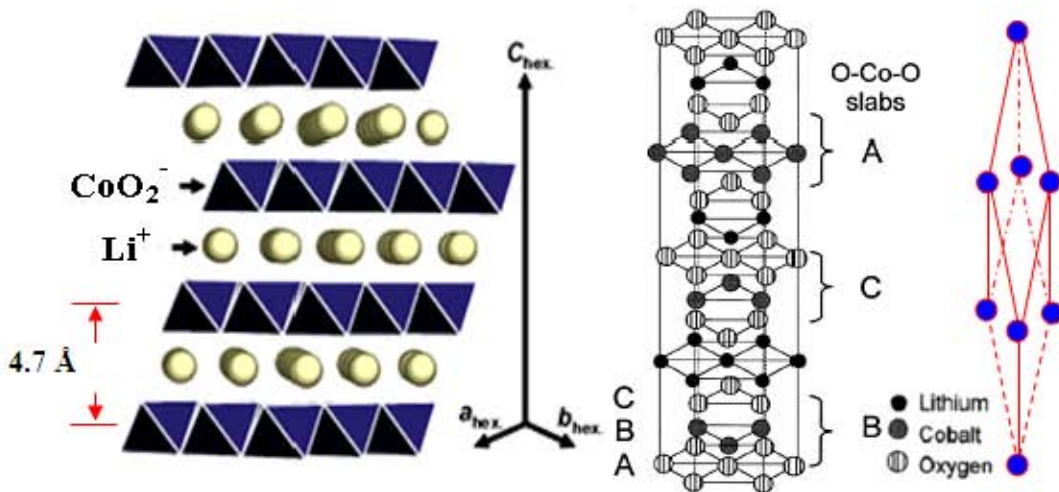
Figure 2.1 The structure of the layered LiCoO$_2$ [49-50].

LiCoO$_2$ consists of edge–shared CoO$_6$ octahedral sheets and interlayer lithium ions. The cubic close-packed oxygen layers stacked in an *ABC* sequence with Co and Li ions living in octahedral sites in alternating layers between the oxygen planes [48, 51]. In addition, the repeating unit of LiCoO$_2$ along the z-direction contains two negative-charged layers of CoO$_2$. The interlayer distance between two CoO$_2$ layers is about 4.7 Å [52]. Li$^+$ ions between interlayer of CoO$_2$ can be reversibly de-intercalated from and intercalated into the interlayer space [48]. Substitution of Li$^+$ ions with large cationic guests by ion-exchange and intercalation reaction, expands a

basal spacing of the layer host. For example, insertion of organocations such as anilinium ($C_6H_5NH_3$), dodecyltrimethylammonium ($C_{12}H_{25}N(CH_3)_3$) increase the d-spacing of $LiCoO_2$ to 12 Å and 27 Å, respectively [47].

2.2 Synthesis of layered $LiCoO_2$

2.2.1 Solid-state reaction

The solid state reaction is a classic method for preparation of oxide powders. The process usually involves mixing metal salts such as acetate, hydroxide, nitrate or carbonate and heating at high temperatures (> 800 °C) for long periods (> 10 h). This process is time-consuming, because of the many hours required for firing and regrinding of the precursors and need an expensive, high temperature furnace. Furthermore, the products may have some undesirable feaures such as irregular morphology, inhomogeneity and large particles size.

2.2.2 Co-precipitation method

Co-precipitation is a one of the wet-chemical techniques for the synthesis of oxide powders. The advantages of this method over conventional solid state reaction are small particle size and large surface area and homogeneity of reactant mixture. Furthermore, the starting materials may be just a simple and rather inexpensive inorganic salts. The process of co-precipitate method also avoids complicated steps [53]. However, in many cases, the single-phased product is hard to achieve because of the rate and possibility to precipitate the desired product may be closed or lower than those of other compounds. Therefore, it is not easy to prepare the single phased materials using this method.

2.2.3 Combustion method

Combustion is a relatively new method for the preparation of oxide powders. This process involves a fast highly exothermic reaction of self-combustion process [54]. Normally the metal nitrates are used as the reactants and dissolved in the fuel-containing solution. The final oxide is calcined at relatively low temperature to

remove all organic species. Furthermore, this method has its advantages over the conventional solid-state method, such as low calcination temperature, short-heating time and the small crystallite size of the products.

2.2.4 Sol-gel method

Sol–gel is widely used to prepare many products such as glasses, ceramics, inorganic fillers and coatings [55]. This method was discovered in the early 1846s by J.J. Ebelenen in studying the formation of SiO_2 gel by hydrolyzing $Si(OEt)_4$. The process involves several steps such as hydrolysis, condensation of a gel precursor and growth of particles. The basic processing steps of this method can be summarized as the followings:

$$Precursor \longrightarrow Hydrolysis \longrightarrow Reactive\ monomer$$

$$Condensation$$

$$Further\ treatment \longleftarrow Gel \longleftarrow Sol\ gelation \longleftarrow$$
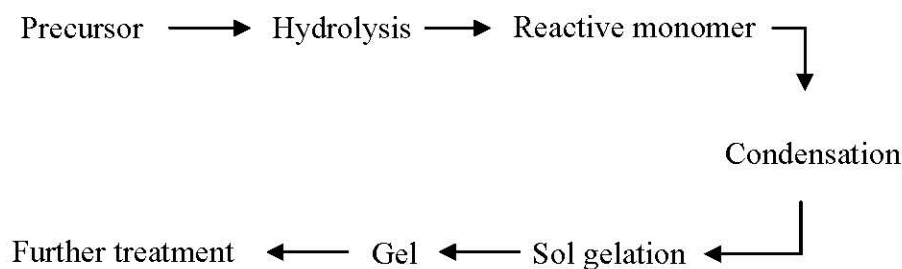
This method has the advantages over the conventional solid-state reaction such as the homogeniety of reactants at the atomic or molecular level, the ease of stoichiometric control, the mild calcinations condition. The method also gives the products with uniform particle size and in nanometer level [6, 10, 12].

2.3 Topological chemistry of layered materials

2.3.1 Intercalation

Intercalation is the insertion of guest species (atoms, ions or molecules) into a crystalline layered lattice with preservation of the layered host structure. Generally, intercalation usually involves reducing the interaction of the host structure and formatting a new interaction between the guest and host, resulting to the expansion of interlayer spaces. The product of this reaction is called an *intercalation compound* [56]. The intercalation reaction can be described by an equation:

$$\textbf{Host} \quad + \quad \textbf{x Guest} \quad \longrightarrow \quad \textbf{Host[x Guest]} \qquad \textbf{(1)}$$

To obtain the intercalation compound, the strong interlayer bonding of layered host causes the difficulty in the intercalation process; therefore, the high activation energy for intercalation needs external energy provides at high temperature or high pressure. For example, the MoO_3-pyridine intercalation compound was achieved by the insertion of pyridine into layered MoO_3 by direct intercalation at 80 $^\circ$C [57]. The high pressure can help in the intercalation process as well. For example, the rate of insertion of small guests such as ethanol and methanol into a layered titanate increases at the pressure of ethanol and methanol medium up to about 10 GPa [58]. The intercalation compound may lead to new materials with novel properties compared to the properties of their components. A new compound can give rise to very interesting several properties, such as electrochemical, electrochromic and conduction properties [59].

2.3.2   Guest exchange

Ion-exchange is a general property of charged layer hosts. In many cases, especially with large guests, the guest exchange reaction may take long time or require evaluated temperatures. For example, the ion-exchange of protons for $Cs_{0.7}Ti_{0.825}\square_{0.175}O_4$ is completed in 3 day, where as the ion-exchange of large TBA^+ cations for $H_{0.7}Ti_{0.825}\square_{0.175}O_4.H_2O$ requires 10 days [42].

2.3.3   Swelling and exfoliation/delamination

After intercalation process, the spacing between layered hosts increases, which depends on the host structure as well as the nature of guest species. The further expansion of the interlayer involving the intercalation of large amounts of solvent is called *swelling*, resulting to the large separation between the layered sheets and reducing the lattice energy of the sheets and interlayered ions, as shown in Figure 2.2.
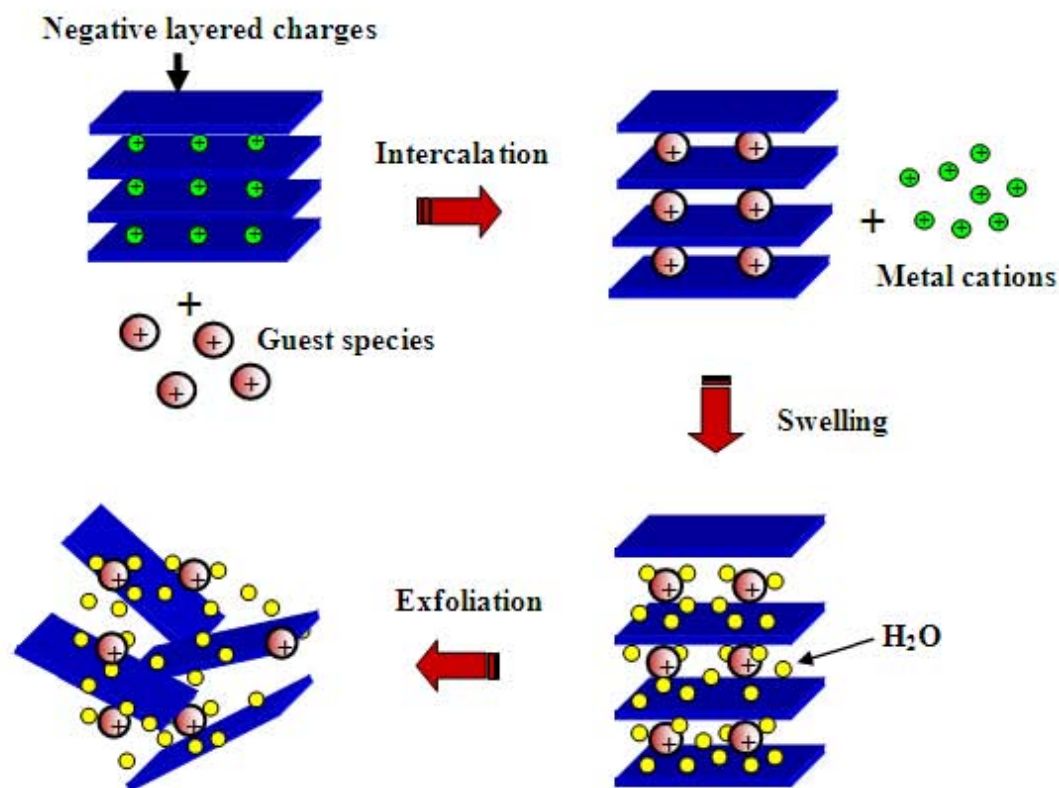
Figure 2.2 Schematic representation of the intercalation, swelling and exfoliation process in layered structure compound.

If the swelling process is taken its extreme, then the host structure can be completely exfoliated or delaminated and leads to the formation of colloidal suspensions (Figure 2.2). The exfoliation of layered materials provides the possibility to reconstruct the two dimensional single sheets to various desired products [60-62]. The single sheet of layered materials may a thickness from one to tens of nanometer. The lateral size is about several hundred nanometers to several micrometers. The size of single sheet materials has a new physicochemical properties compared with their bulk solids [63]. The exfoliated sheets are typically observed for some layered materials such as clay minerals [36], titanate [28, 35, 42, 43], $HNbWO_6$ [44], $H_{0.13}MnO_2 \cdot 0.7H_2O$ [31-33, 64] etc. In many cases, the exfoliated sheets were used for the preparation of the nanocomposite with various organic molecules, high surface area catalysts and thin films. However, some layered hosts are not easily swelled or exfoliated, and some degrade under required reaction conditions.

2.4 Ultrasound processing

Ultrasound processing is the act of applying sound energy to agitate particles in a sample for various purposes; for example, it can be used to speed dissolution by breaking intermolecular interactions. Ultrasound has a frequency in the range of 18 kHz to 100 MHz. High-intensity ultrasound irradiation at 20 kHz enhances the rate of various chemical reactions. This range of ultrasound does not affect chemical bonding directly, but affects reaction indirectly through the phenomenon of cavitation. Cavitation is the production of microbubbles in a liquid caused by a large pressure drop, like the rapid motion of the propeller blade through the liquid, and pulls the liquid molecules apart to crease tiny cavities. These cavities or bubbles are created, expanded, and collapsed with the release of intense local energy as shown in Figure 2.3, providing hot spot regions that can drive high-energy chemical reactions. Hot spots may have a temperature of ~5000 °C, pressure of about 1000 atm, and heating and cooling rates above 10^{10} K/s) [65-66].
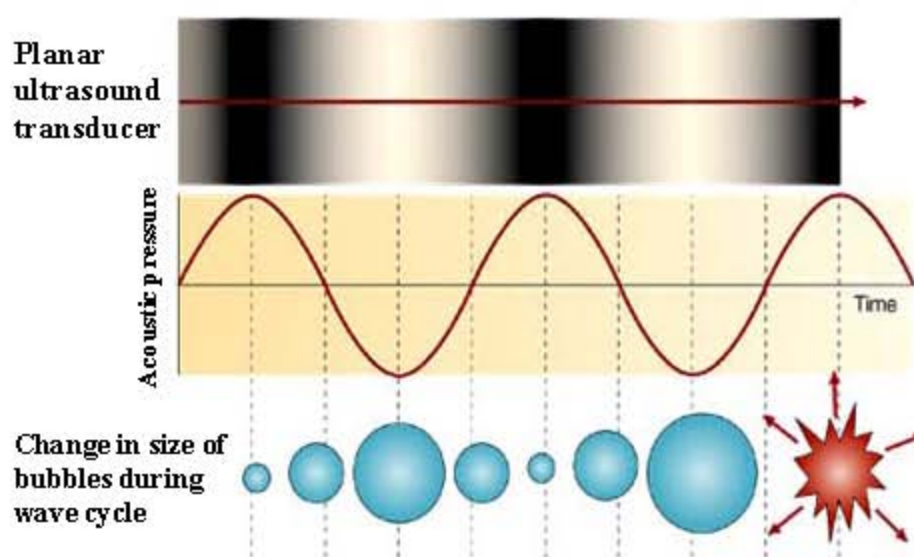
Figure 2.3 The principles of inertial cavitation [67].

In liquid-solid systems, cavitational collapse affects the surface of solids in two ways.

1. The collapse occurs at the surface. Surface defects, entrapped gases, or impurities on the surface cause nucleation and cavitational collapse directry. The localized heating on the surface can lead to fragmentation of solids.

2. The collapse occurs close to the surface, near a solid surface, bubble collapse becomes nonspherical, driving high-speed jets of liquid into the surface as shown in Figure 2.4. This phenomenon can significantly increases mass transport between solution and surface.
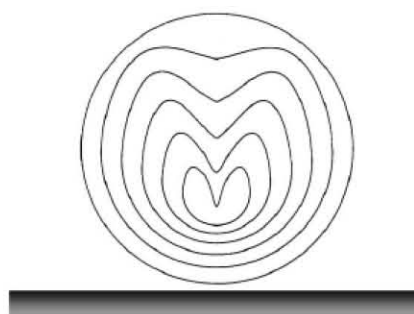
Figure 2.4 Formation of a liquid microjet during bubble collapse near solid surface. [66].

In many cases, Ultrasound enables to synthesize various types of nano-sized material and composites [68]. Recently, ultrasound processing is used for shortening the reaction time for intercalation-exfoliation process. For example, Sukpirom and Lerner reported [41] that ultrasound increases the rate of exfoliation of layered $H_xTi_{2-x/4}O_4 \cdot yH_2O$ (H–Ti) in TBAOH solution. Applied the ultrasound with the power of $60 - 300$ W for $2 - 30$ min effectively reduces the H–Ti particle size to <100 nm.

2.5 Properties of colloids

Colloid is a type of mechanical mixture where one or more of the components have at least one dimension within the range of about 1 nm to 1000 nm. The mixture is also called a *colloidal solution, colloidal system, colloidal suspension* or *colloidal dispersion*. A colloidal system consists of two separate phases: a *dispersed phase* (or internal phase) and a *continuous phase* (or dispersion medium). In the solid-liquid

system, the dominant phase is dispersed phase (for the phase forming the solids) and dispersion medium (for the medium in which the solids are distributed). In this thesis, the colloids of layered $LiCo_{1-x}Mn_xO_2$ phase (dispersed phase) and TBAOH solution phase (dispersion medium) is classified as the colloidal suspension in solid-liquid system.

2.5.1 Brownian motion

Brownian motion is the movement of single colloidal particles. The motion is a random zigzag movement of the particles because of the collision of colloid particles in the dispersion medium. It was discovered under a microscope by the botanist Robert Brown in 1827 [70].

2.5.2 Optical properties

2.5.2.1 Tyndall effect

Light scattering of the particles is a characteristic property of colloid. When the light passes though the colloidal dispersion, some portion may be absorbed, some is scattered and the residue is transmitted. The light scattering of colloid results from the electric field associated with the incident light inducing periodic oscillations of the electron clouds of the atoms of the particles [69]. This effect, called the *Tyndall effect* as shown in Figure 2.5, was first explained by the British physicist John Tyndall.
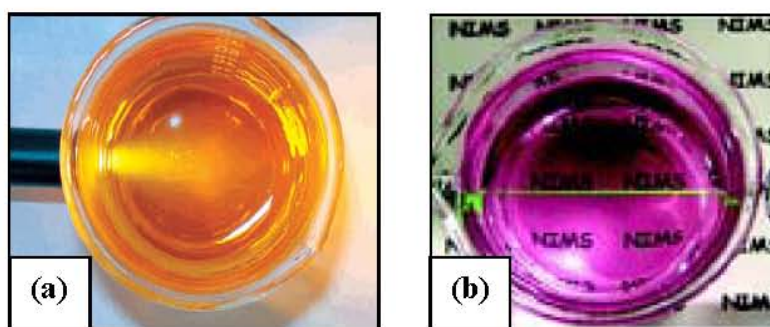
Figure 2.5 Photograph of a colloidal suspension of (a) MnO_2 nanosheets [71] and (b) exfoliated Co-Al LDH nanosheets [72].

2.5.2.2 Turbidity

Turbidity is an optical property of solid-liquid colloid that causes light to be scattered and absorbed rather than transmitted in straight lines through the colloidal dispersions. As a beam of light passes though the colloidal suspension, the intensity of scattered light is a function of solid concentration. The intensity of scattered light from a colloidal system depends on color, size and shape of the scattering particles, the interaction from them, and the difference between the refractive indices of the particles and dispersion medium [69, 73].
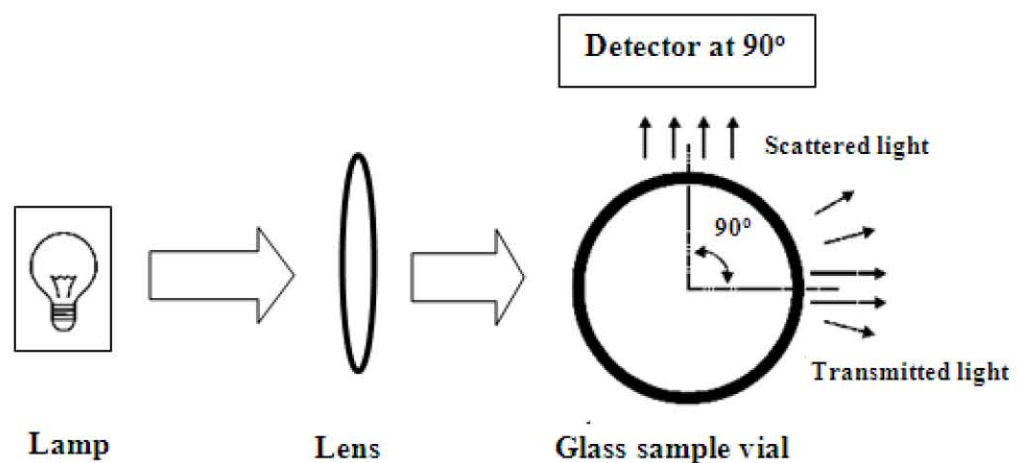
Figure 2.6 Basic nephelometric arrangement of turbidity measurement [74].

Turbidity is normally measured using a nephelometer, which is a meter that measures the intensity of light scattered at 90° as a beam of light passes through a sample. Figure 2.6 shows the basic optical system. The most commonly used turbidity unit is nephelometric turbidity units (NTU). This unit indicates in the intensity of the colloidal light scattered compared with a known concentration of a standard solution.

2.5.3 Interaction between colloid particles

2.5.3.1 Electrostatic interaction: The electrostatic interaction is dominant in the stability of suspensions. In generally, the colloidal particles have an electrical charge, therefore attract or repel each other.

2.5.3.2 Van der Waals forces: This is an interaction force between two dipoles that are either permanent or induced. If the particles do not have a permanent dipole, wavering of the electron density gives rise to a temporary dipole in a particle. This temporary dipole induces a dipole in nearly particles. The temporary dipole and the induced dipoles are then attracted to each other. This is called *Van der Waals force*, and is always present, is short-range, and is attractive.

2.6   Thin film technology

Thin film preparation from layered oxides has been widely studied because of the diverse characteristics when compared with the bulk materials. In addition, the nanoscale films showed a wide range of applications for systems in optics, microelectronics, and magnetic [31, 33]. There are many methods to prepare thin film such as a sol–gel synthesis, sputtering and chemical vapor deposition (CVD). But these processes have to use a high temperature, a high qualitative vacuum system and intricate equipments. The resulting films have a limit of film area or thickness and mechanical instability, respectively [75]. Layer-by-layer (LBL) self-assembly method using a sequential adsorption of oppositely charged materials is used for preparing multilayer thin films with various advantages such as a simple process, low temperature deposition, no limit of thickness and needless of complicated equipments, and it can be used to architect the film layers on a nanometer scale [75-76].

2.6.1 Principles of layer-by-layer (LBL) self-assembly

The LBL adsorption of monolayer is based on electrostatic self-assembly (ESA) between the negative and positive charged layers. Generally, polycation and polyanion such as poly(diallydimethylammonium) chloride; PDDA or PDAD, polyethylenimine; PEI, polydipoly(styrenesulfonate); PSS etc. are normally used as charged polymer layers to construct the LBL films (Figure. 2.7).
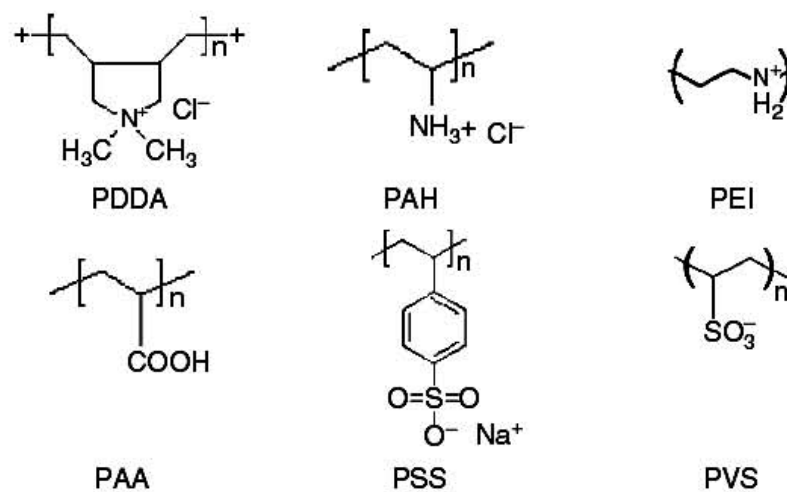
Figure 2.7 Structural schematic of frequently used polycation and polyanions [77].

The solid substrate such as glass slide, quartz slide, silicon wafers are used for prepare thin films by this method. When the substrate dips into polycation solution, polycationic molecules come close to the negatively charged substrate, the local electric field is so strong that it attracts molecules to the surface. Therefore, the surface of substrate is completely covered by the layer of cationic molecules that balances the charge of the negative layer substrate. Then, the substrate become to the positively charged and it used as template to attract negatively charged molecules during subsequent dipping. The process of LBL self-assembly is illustrated in Figure 2.8. A series of these operations are repeated n times to obtain multilayer films of (polycation/polyanion)$_n$. However, this method is used for many application with various a kids of cationic or anionic molecules. Figure 2.8b shows the application of LBL self-assembly for the formation of composite films.
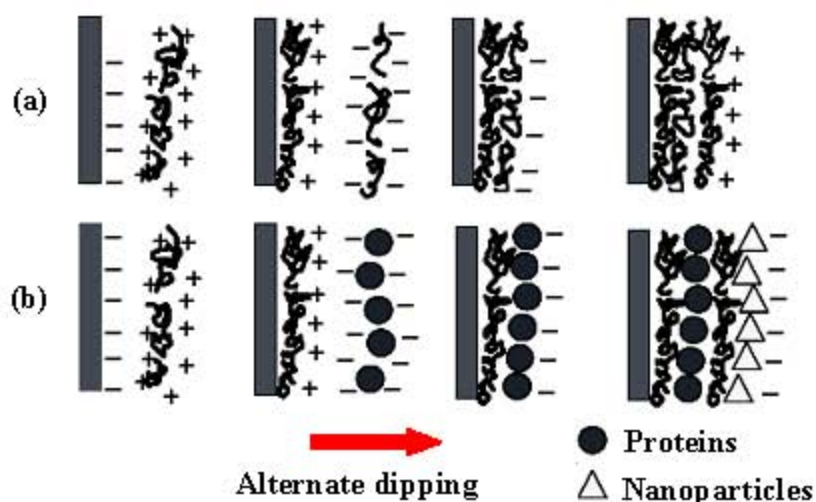
Figure 2.8 Schematic schemes of the LBL self-assembly for (a) alternate adsorption of polycations and polyanions on the solid substrate, and (b) alternate adsorption of polyions, proteins and nanoparticles on the substrate [77].

2.7   Characterization of materials

2.7.1 X-ray diffraction (XRD)

X-ray diffraction (XRD) is one of the most important non-destructive techniques to determine the crystalline structure, phase identification and can provide information on unit cell dimensions of solid. X-rays are generated by a cathode ray tube, filtered to produce monochromatic radiation, collimated to concentrate, and directed toward the finely ground sample. A monochromatic beam of X-ray incident on the surface of sample at an angle θ. The scattered intensity can be measured as a function of scattering angle 2θ. The different phases presenting in the sample are efficiently determined by XRD technique. The XRD pattern is plotted between the peak positions (2θ angle) and intensities of the diffracted beam. The peaks are obtained by varying the incidence angle. The positions and intensities of the peaks act as a distinctive "fingerprint" which provides the information of sample. The Joint Committee on Powder Diffraction Standards (JCPDS) database used to identify of the crystalline compounds. To calculate the crystallite size form XRD pattern, in 1918 Scherrer developed the equation:

$$L = \lambda K / \beta \cos\theta \qquad\qquad (2)$$

Where **L** is the crystallite size (Å). **K** is the shape factor, which typically has a value about 0.9 and **β** is the full widths at maximum half-height (FWMH) of the peak in radians of 2θ. The width of a diffraction peak is influenced by the crystallite size: a large crystallite size causes sharp reflections, whereas a small size leads to broad reflections.

2.7.2 Transmission Electron Microscope (TEM)

TEM is a microscopy technique used for studying the size, size distribution and morphology of particles. TEM involves a beam of accelerated electron, 50-200 keV, emitted by a tungsten filament cathode in vacuum. These electrons are deflected in small angles by atoms in sample and transmitted through a thin sample. Then, these electrons are magnified by magnetic lenses and hitting a fluorescent screen coated with a phosphor to generate the bright field image. A schematic diagram of transmission electron microscope is shown in Figure 2.9. The images from electron microscopes indicate the shape of a sample crystallite which can be used to determine size and morphology of solid nanoparticles. In this study, TEM can be used to examine the dispersion of layer host.
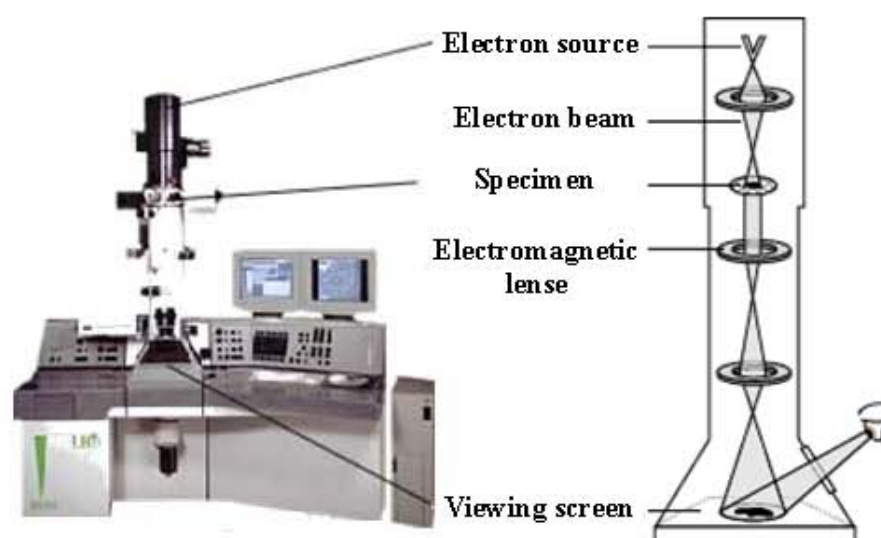
Figure 2.9 Schematic diagram of transmission electron microscope [78].

2.7.3 Fourier transform infrared spectroscopy (FT-IR)

The FT-IR spectroscopy is most widely used for the identification of the chemical bonds of organic molecules, inorganic materials and organometallic compounds. In addition, it can be used for investigated the purification of materials [73]. The chemical bond vibrations usually have energies in the infrared region. KBr pellet is commonly used to study the solid samples. The solid samples can be milled with potassium bromide (KBr) to form a very fine powder. Then this powder is compressed into a thin film pellet. For organic-inorganic composite thin films, the IR absorption spectra can confirm the existence of the polymer component and layered host materials.

2.7.4 Ultraviolet-visible spectroscopy (UV-Vis)

UV-Vis spectroscopy is widely used to measure of the absorption of ultraviolet and visible light by a sample. The absorption of light is caused by electronic transitions of the valence electrons with specific wavelengths. The absorption and the intensity of the absorption show the information of electronic structure of sample. The light source is usually a hydrogen or deuterium lamp for UV measurements and a tungsten lamp for visible measurements. These light sources emit light over a broad range of wavelengths. Spectra are obtained by recording the intensity of absorption at each wavelength over a given range. Schematic diagram of this equipment is shown in Figure 2.10.
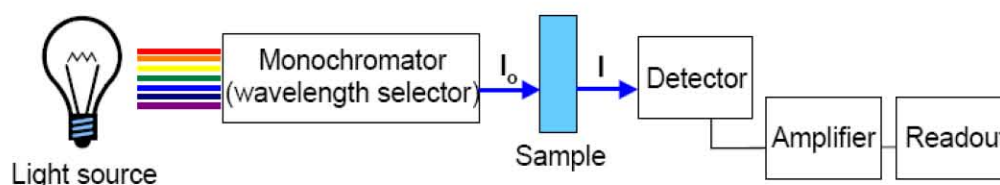
Figure 2.10 Schematic diagram of a spectrophotometer [79].

Experimental measurements are usually made in terms of absorbance, the relationship between absorbance (A) and concentration (c) is defined by Beer-Lambert Law:

$$A = \varepsilon bc = -\log T = -\log (I / I_o) \qquad (3)$$

Where **A** is the measured absorbance, **ε** is known as the molar extinction coefficient, **b** is the path length of the absorbing solution on centimeters, **c** is the concentration in moles/liter. **T** is the transmittance, **I** is the light intensity after it passes through the sample and **I_o** is the initial light intensity.

Nanometer-sized semiconductor particles or layers are an intermediate form between molecules and bulk solids. For semiconductor materials, the electronic band structures are due to the confinement of the electron-hole pair in the restricted space of the semiconductor particles. As the particles get smaller, the band gap is larger, resulting from shifts of the conduction band edge to the higher energy and the valence band edge to lower energy. The smaller the thickness of the particles with the larger exciton energy (ΔE_g) has been observed for several layered semiconductor materials in colloidal or exfoliated state such as GaS, PbI_2, TiO_2, $H_xTi_{2-x/4} \square_{1/4}O_4.H_2O$ etc. [80]. In many cases, UV-Vis spectra of the suspensions are comprised of larger particles that show very broad spectra indicating to the light scattering by larger particles. If the particles get small, the broad spectrum is gradually changed to a shape absorption peak. For example, the suspension with large particles of layered $H_xTi_{2-x/4} \square_{1/4}O_4 \cdot yH_2O$ showed very broad peak. When the particles got smaller leading to the sharp absorption peak at a higher energy of 270 nm [41]. In other research, Omomo *et al.* [81] reported the optical property of layered $H_{0.13}MnO_2 \cdot 0.7H_2O$. A diffuse scattering spectrum revealed an almost constant and featureless absorption in the range 200 – 800 nm, resulting from reflection of the larger particles size. While the exfoliated absorption spectra of MnO_2 nanosheets with broad peak centered at 374 nm. Furthermore, a blue shift of spectra in UV-Vis absorption with decreasing in particle size, can be observed in several compounds such as layered $H_2K_2Nb_6O_{17}$ [30] and CdS [82].

2.7.5 Atomic force microscopy (AFM)

Atomic force microscopy (AFM) has become the most widely used technique to examine the thin surface. The AFM consists of a microscale cantilever with a sharp tip at its end. It is used to scan the sample surface. Schematic diagram of atomic force microscope is shown in Figure 2.11. AFM measures the interaction force (e.g. attractive, repulsive, magnetic, electrostatic, Van der Waals) between a sharp tip and the sample surface. The tip may be dragged across the surface, or may vibrate as it moves. The interaction forces depend on the nature of the sample, the probe tip and the distance between them [83].
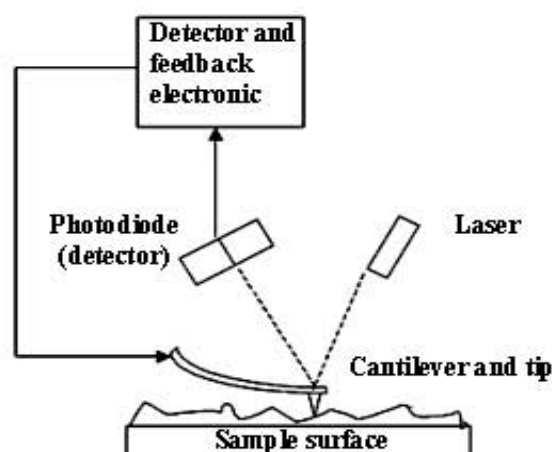
Figure 2.11 Schematic diagram of atomic force microscope [84].

When the tip is brought close to a sample surface, the forces between the tip and sample cause the cantilever to bend. This movement can be detected by the deflection of a laser beam which is reflected off the back of the cantilever. When the tip is scanned over the sample surface, the deflection of the cantilever can be recorded as three-dimensional image of the sample surface [83, 85]. The AFM can be operated in many modes depending upon the applications which tapping mode is the most commonly used. This mode are better than the contact and non-contact mode such as eliminating lateral forces that can damage soft samples and reduce image resolution [86]. For the surface topography of the thin films, the images of sample were recorded by tapping mode. In this project this technique used for study the roughness and layer thickness of films with various numbers of bilayer.

CHAPTER III

EXPERIMENTAL

3.1 Chemicals:

1. Lithium nitrate, $LiNO_3$ (PRS Panreac, 98%)

2. Cobalt nitrate, $Co(NO_3)_2.6H_2O$, (Fisher, reagent grade)

3. Manganese nitrate, $(Mn(NO_3)_2.4H_2O$ (PRS Panreac, 97%)

4. Citric acid anhydrous, $C_6H_8O_7$ (Scharlau, 95.5%)

5. Ethanol absolute, C_2H_5OH (Merck, $\geq$99.9%)

6. Sulfuric acid, H_2SO_4 (Merck, 95-97%)

7. Hydrochloric acid, HCl (Merck, 37%)

8. Tetrabutylammonium hydroxide 40% in water, TBAOH (Acros organics, reagent grade)

9. Poly(diallydimethylammonium) chloride 20% in water, PDADMAC/PDAD (Aldrich, reagent grade)

10. Hydrogen peroxide 30%, H_2O_2 (Merck, reagent grade)

11. Ammonia solution 25%, NH_4OH (Merck, reagent grade)

12. Sodium chloride, NaCl (CARLO ERBA, 99.5-100.5%)

13. Potassium bromide, KBr (Fluka, $\geq$99.5%)

14. Milli-Q water ~18.2 M Ω

15. Deionized water (DI)

16. Reverse osmosis water (RO)

3.2 Synthesis of $LiCo_{1-x}Mn_xO_2$ (x = 0.0 - 1.0)

The $LiCo_{1-x}Mn_xO_2$ (x = 0.0 - 1.0) powders were synthesized by modifying the method of Hanh et $al.$ [6] as presented in Scheme 3.1. The $LiCo_{0.8}Mn_{0.2}O_2$ of approximately 1 g was obtained by dissolving a stoichiometric amount of lithium, cobalt and manganese nitrate salts (0.7102 g of $LiNO_3$, 2.3985 g of $Co(NO_3)_2 \cdot 6H_2O$, 0.5172 g of $Mn(NO_3)_2 \cdot 4H_2O$) and 5.9379 g of citric acid in a total acid to nitrate molar ratio of 1 in 50 mL of ethanol. Other samples with various amounts of the reactants are summarized in Table 3.1. The solution mixtures were heated at 100 –

120 °C to obtain the as-synthesized powders, and then calcined at 300 – 700 °C for 6 - 12 h. The structural phase compositions were investigated using the X-ray diffraction (XRD). The LCMx code is referred to the calcined $LiCo_{1-x}Mn_xO_2$ where x is the molar ratio of Mn to Mn+Co (Table 3.2).

$LiNO_3$	$Co(NO_3)_2 \cdot 6H_2O$	$Mn(NO_3)_2 \cdot 4H_2O$	Citric acid

1) Dissolve in ethanol.
2) Stir for 24 h.
3) Dry at 100 - 120 °C.

As-synthesized $LiCo_{1-x}Mn_xO_2$

Calcine at 300 – 700 °C for 6 - 12 h.

(Heating rate 2 °C/min)

Calcined $LiCo_{1-x}Mn_xO_2$
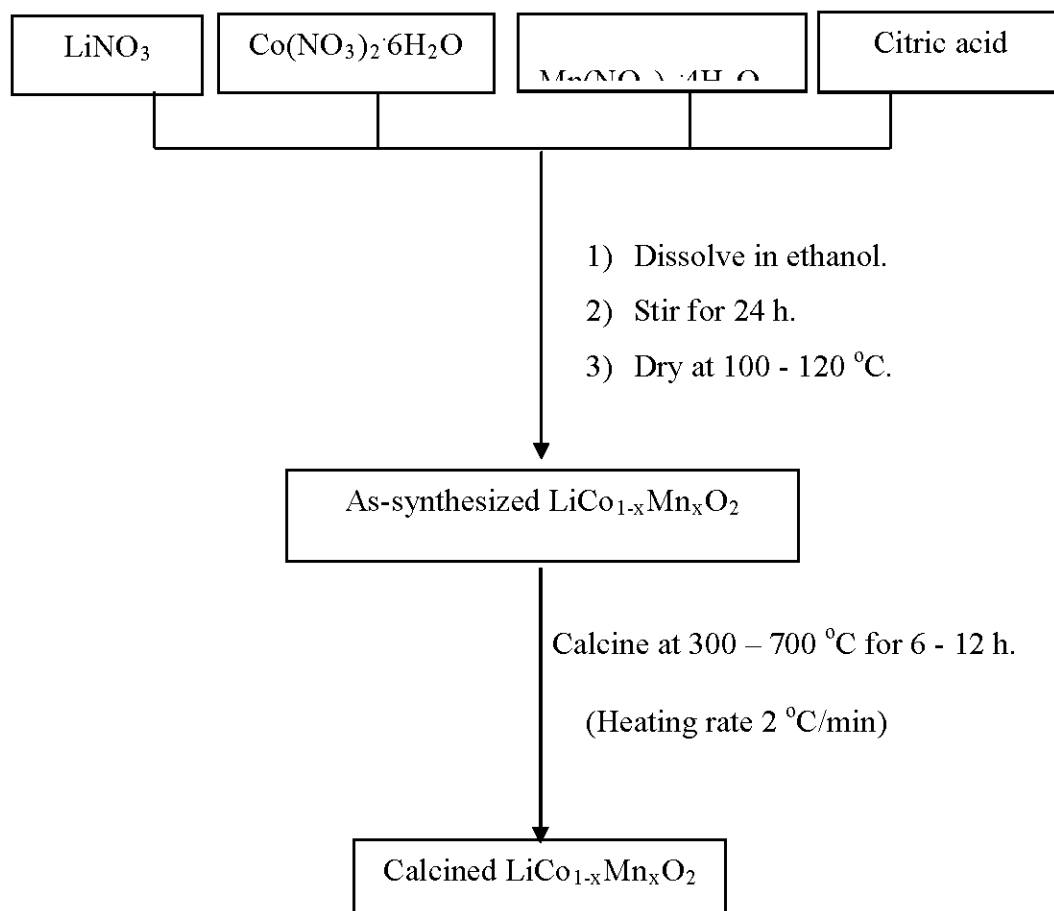
Scheme 3.1 Experimental scheme for the synthesis of $LiCo_{1-x}Mn_xO_2$ (x = 0.0 - 1.0).

Table 3.1 Stoichiometric amounts of starting materials for $LiCo_{1-x}Mn_xO_2$ synthesis

x	LiNO$_3$ (g)	Co(NO$_3$)$_2$·6H$_2$O (g)	Mn(NO$_3$)$_2$·4H$_2$O (g)	Citric acid (g)
0.0	0.7047	2.9736	0.0000	5.8893
0.1	0.7073	2.6873	0.2575	5.9135
0.2	0.7102	2.3985	0.5172	5.9379
0.3	0.7131	2.1074	0.7790	5.9624
0.4	0.7161	1.8138	1.0429	5.9872
0.5	0.7191	1.5178	1.3091	6.0122
0.6	0.7220	1.2192	1.5774	6.0368
0.7	0.7251	0.9183	1.8480	6.0622
0.8	0.7281	0.6148	2.1209	6.0878
0.9	0.7312	0.3087	2.3962	6.1136
1.0	0.7343	0.0000	2.6737	6.1396

3.3 Proton-exchanged form of $LiCo_{1-x}Mn_xO_2$

$LiCo_{1-x}Mn_xO_2$ was converted into its proton-exchanged form by modifying the method of Gupta *et al.* [87]. $LiCo_{1-x}Mn_xO_2$ (2g) was dispersed in 100 mL 0.35 M H_2SO_4 aqueous solution and stirred at room temperature for 24 h. The product was centrifuged, washed with DI water, and dried at 50 °C in vacuum oven overnight. The proton-exchanged form of $LiCo_{1-x}Mn_xO_2$ is referred as $HCo_{1-x}Mn_xO_2$ (HCMx). For example, $HCo_{0.8}Mn_{0.2}O_2$ abbreviated as HCM0.2.

Table 3.2 The sample codes for $LiCo_{1-x}Mn_xO_2$ samples and their proton-exchanged form

x	Compounds (Theoretical formula)	Sample codes
0.0	$LiCoO_2$	LCM0.0
	$HCoO_2$	HCM0.0
0.1	$LiCo_{0.9}Mn_{0.1}O_2$	LCM0.1
	$HCo_{0.9}Mn_{0.1}O_2$	HCM0.1
0.2	$LiCo_{0.8}Mn_{0.2}O_2$	LCM0.2
	$HCo_{0.8}Mn_{0.2}O_2$	HCM0.2
0.3	$LiCo_{0.7}Mn_{0.3}O_2$	LCM0.3
	$HCo_{0.7}Mn_{0.3}O_2$	HCM0.3
0.4	$LiCo_{0.6}Mn_{0.4}O_2$	LCM0.4
	$HCo_{0.6}Mn_{0.4}O_2$	HCM0.4
0.5	$LiCo_{0.5}Mn_{0.5}O_2$	LCM0.5
	$HCo_{0.5}Mn_{0.5}O_2$	HCM0.5
0.6	$LiCo_{0.4}Mn_{0.6}O_2$	LCM0.6
	$HCo_{0.4}Mn_{0.6}O_2$	HCM0.6
0.7	$LiCo_{0.3}Mn_{0.7}O_2$	LCM0.7
	$HCo_{0.3}Mn_{0.7}O_2$	HCM0.7
0.8	$LiCo_{0.2}Mn_{0.8}O_2$	LCM0.8
	$HCo_{0.2}Mn_{0.8}O_2$	HCM0.8
0.9	$LiCo_{0.1}Mn_{0.9}O_2$	LCM0.9
	$HCo_{0.1}Mn_{0.9}O_2$	HCM0.9
1.0	$LiMnO_2$	LCM1.0
	$HMnO_2$	HCM1.0

3.4 Dispersion of HCMx

The colloidal suspensions of HCMx were prepared by modifying the methods of Sasaki *et al.* [31] and Sukpirom and Lerner [29]. 0.2 g of HCMx was added to an aqueous solution of 50 mL 0.04 M TBAOH in 100 mL glass bottle. The mixture was shaken with the speed of 300 rpm for 24 h at room temperature, and then sonicated for 30 minutes using ultrasonic processor with Ti alloy probe (13 mm diameter) at

125 watts. After sonication, the suspension was centrifuged at 3000 rpm for 10 min. The samples were divided in 2 parts: (i.) the supernatant colloidal suspension of HCMx, so called *upper phase* (abbreviated as Up-HCMx), and (ii.) the precipitates, so called *deposited phase* (abbreviated as Dep-HCMx). Both parts were cast on glass substrates and dried in air for 24 h prior to the characterization by XRD.

3.4.1 Effect of TBAOH concentration

The effect of TBAOH concentration was studied by dispersing a fixed amount of the 0.2 g HCM0.2 in 50 mL TBAOH aqueous solution. The mixture were shaken at 300 rpm for 24 h and then sonicated for 30 min. The molar ratio of TBA cation to exchangeable protons in HCM0.2 (referred as TBA/HCM0.2) was adjusted to 0.0, 0.1, 0.5, 1.0, 2.0, 3.5 and 5.0 folds. After sonication, the colloidal suspensions were centrifuged at 3000 rpm for 10 min in order to separate the deposited phases. All samples of the Up-HCM0.2 and Dep-HCM0.2 were cast on glass substrates and dried in air for 24 h prior to the characterization by XRD. The Up-HCM0.2 samples were diluted 50-fold in Milli-Q water and analyzed by UV-Vis spectroscopy.

3.4.2 Effect of sonication time

The effect of sonication time towards the dispersion process was studied by dispersing a fixed amount of 0.2 g HCM0.2 in 50 mL TBAOH aqueous solution with TBA/HCM0.2 = 1.0. The mixtures were shaken at 300 rpm for 24 h, and sonicated for 0, 30, 60 and 90 min. After sonication, the colloidal suspensions were centrifuged at 3000 rpm for 10 min in order to separate the deposited phases. All samples of the Up-HCM0.2 and Dep-HCM0.2 were cast on glass substrates and dried in air for 24 h prior to the characterization by XRD. The Up-HCM0.2 samples were diluted 50-fold in Milli-Q water and analyzed by UV-Vis spectroscopy.

3.5 Fabrication of multilayer thin film by LBL technique

3.5.1 Priming of substrates

Substrates, glass slides and quartz slides, were treated in a piranhas solution (3:1 volume ratio of concentrated H_2SO_4 and 30% H_2O_2) for 30 min, followed by thorough rinsing with DI water for several times. The substrates were further treated with the mixture of concentrated NH_3, 30% H_2O_2 and H_2O (1:1:5 in volume) at $40 - 50\,°C$ for 30 min. After that, the cleaned substrates were dried at room temperature.

3.5.2 Preparation of multilayer thin films

Multilayer thin films were prepared by modifying the layer-by-layer (LBL) assembly procedure of Sasaki *et al.* [31]. The clean substrates were immersed in 50 mL 10 mM Poly(diallyldimethylammonium chloride) (PDAD) aqueous solution containing 0.5 M NaCl. The experiment was under shaking with 50 rpm for 10 min to get a positively charged substrate, and followed by thorough washing with Milli-Q water for 3 times (10s each time). Then the positively charged substrate was immersed in a 50 mL colloidal suspension of Up-HCM0.2 for 10 min, and washed with Milli-Q water for 3 times again. After that, it was dried at room temperature. The apparatus set-up of this process is shown in Figure 3.1.
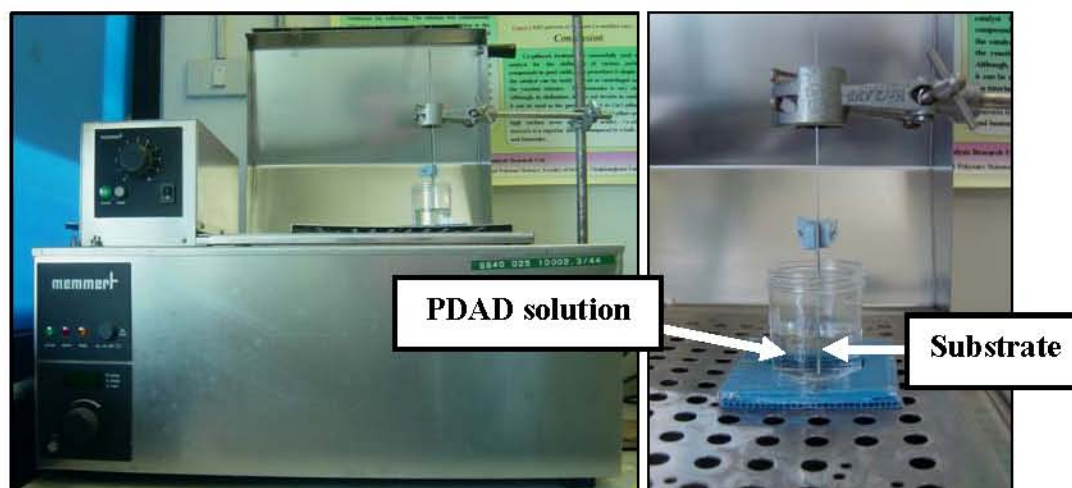
Figure 3.1 Apparatus set-up for multilayer thin film preparation.

A series of these operations were repeated *n* times to obtain multilayer films of (PDAD/HCM0.2)$_n$; n = 0 - 20, as shown in scheme 3.2. The multilayer films fabricated on quartz substrates were analyzed by UV-Vis spectroscopy. The samples for AFM prepared on glass slide were examined by AFM in a tapping mode. Infrared spectra were recorded on samples pressed into KBr disks using FT-IR spectrometer.
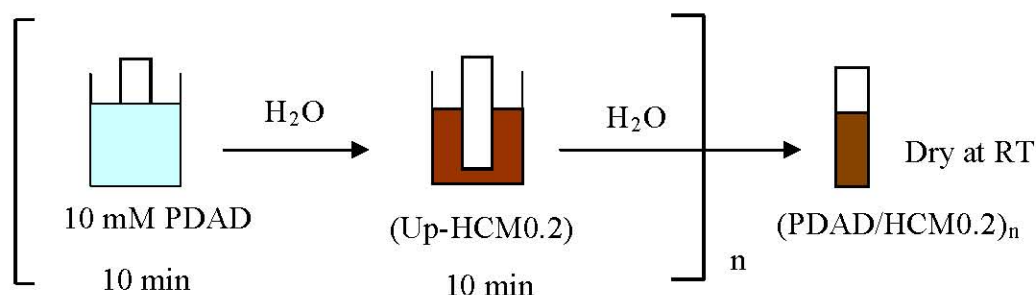
Scheme 3.2 Experimental steps of thin film preparation.

3.5.3 Effect of NaCl concentration

The effect of NaCl concentration to the thin film preparation was studied in the substrate with one bilayer ((PDAD/HCM0.2)$_n$; n = 1). The procedure was similar to section 3.5.2 with the addition of 0.00 - 1.00 M NaCl in the PDAD solutions.

3.5.4 Effect of dipping times

The effect of dipping times to the thin film preparation was studied in the substrate with one bilayer ((PDAD/HCM0.2)$_n$; n = 1). The dipping time in the PDAD solution containing 0.50 M NaCl was fixed at 10 min. The dipping times in the colloidal suspension of HCM0.2 were varied at 1, 2, 5, 10, 20, 40 and 60 min.

3.6 Characterization techniques

3.6.1 Powder X-ray diffraction (XRD)

The XRD patterns of all samples were determined by a Rigaku, Dmax 2200/Ultima$^+$ diffractometer equipped with a monochromator and Cu Kα radiation. The tube voltage and current were set at 40 kV and 30 mA, respectively. The diffraction pattern was recorded in the 2-theta ranged from 2 - 30 degree and 15 - 60 degree with a scan speed of 3 degree/min and a scan step of 0.02 degree. The scattering slit, divergent slit and receiving slit were fixed at 0.5 degree, 0.5 degree and 0.15 mm, respectively.

3.6.2 Inductively coupled plasma-atomic emission spectroscopy (ICP-AES)

Lithium, cobalt and manganese contents in the LCMx and HCMx samples were analyzed using the Perkin Elmer Plasma-1000 inductively coupled plasma-atomic emission spectrometer (ICP-AES). The samples were digested with acid as the followings: 0.0200 g of samples in a 100 mL beaker was soaked with 5 mL of 6 M HCl and heated on a hotplate to a clear solution. The step was repeated for 3 times. The clear solution was transferred to a 500 mL volumetric flask and made to the volume with reverse osmosis water. The sample concentration was approximately 40 mg/L (ppm).

3.6.3 UV-Visible spectroscopy (UV-Vis)

The absorption spectra of colloidal suspensions and thin films were recorded by a Shimadzu UV-2550 UV-Visible spectrophotometer in the absorbance mode. The measurement was in the range of 190 to 900 nm, the sampling interval and slit width were 0.1 nm and 1.0 nm, respectively.

3.6.4 Fourier transform infrared spectroscopy (FT-IR)

Fourier transform infrared (FT-IR) spectra were recorded on a Nicolet Impact 410 FTIR spectrometer. Sample powders were prepared as a KBr pellet, by grinding a small amount of sample with dried KBr and pressing to 6000 psi in a pellet press. IR data were collected from 4000 to 400 cm^{-1}.

3.6.5 Transmission electron microscopy (TEM)

The morphology and particle size of layered $LiCo_{1-x}Mn_xO_2$ before and after exfoliation process were investigated by a JEOL; JEM-2100 transmission electron microscopy.

3.6.6 Turbidity meter

The turbidity of colloidal suspensions was determined by a TN-100 turbid meter with an infrared-emitting diode (850 nm wavelength) light source and silicon photovoltaic detector.

3.6.7 Atomic force microscopy (AFM)

Atomic force microscopy (AFM) with the NanoScope IV A controller was used to examine the surface topology and the thickness of thin films prepared on glass substrates. AFM images were acquired in a tapping mode.

3.7 Instruments and apparatus

3.7.1 Muffle furnace

The calcination was performed on a Carbolite RHF 1600 muffle furnace in air. The furnace was used for $LiCo_{1-x}Mn_xO_2$ synthesis. The process was able to remove the moisture and decompose organic impurities from the samples. The temperature program for the calcination of $LiCo_{1-x}Mn_xO_2$ is shown in Scheme 3.3.

300 – 700 °C, 6 -12 h

2 °C/min

2 °C/min

100 °C
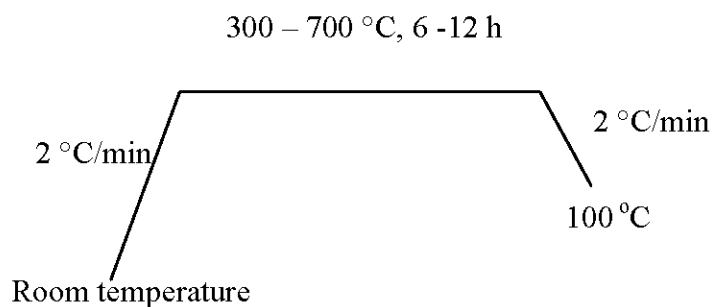
Room temperature

Scheme 3.3 The temperature program for the calcination of $LiCo_{1-x}Mn_xO_2$.

3.7.2 Centrifuge

The separation and collection of the HCMx samples were processed by a Sanyo centrifuge at speed of 3,000 rpm for a few minutes. In addition, this equipment was used to separate the precipitates (Dep-HCMx) from colloidal suspension (Up-HCMx) at speed of 3000 rpm for 10 min.

3.7.3 Oven

The HCMx and Dep-HCMx samples were dried in an EYELA VOS-301SD vacuum oven at 50 °C overnight.

3.7.4 Shaker

The suspensions of HCMx were obtained by Heidolph VIBRAM100 shaker with setting at 300 rpm for 24h, In addition, the multilayer thin films were prepared using Memmert shaker with setting at 50 rpm (speed no. 4).

3.7.5 Ultrasound

The dispersions of HCMx were obtained using VC 505 ultrasonic processor with Ti alloy probe (13 mm diameter) at 125 watts.

CHAPTER IV

RESULT AND DISCUSSION

4.1   Synthesis and characterization of LiCoO$_2$ powders

4.1.1   X-ray diffraction (XRD)

LiCoO$_2$ was synthesized by modifying the method of Hanh *et al.* [6]. The temperature and time of calcination to obtain a single-phased LiCoO$_2$ were studied. The XRD patterns of as-synthesized and calcined LiCoO$_2$ samples are shown in Figure 4.1.
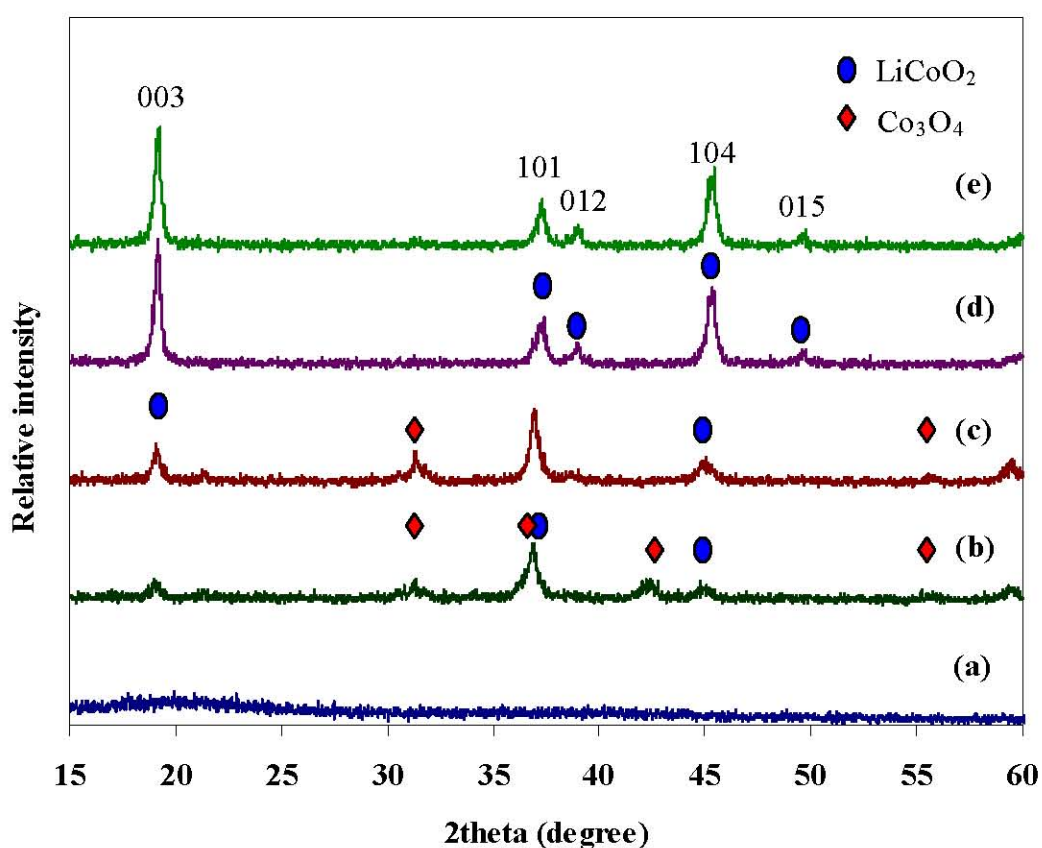
Figure 4.1 XRD patterns of (a) as-synthesized LiCoO$_2$ and (b) calcined LiCoO$_2$ at 300 $^{\circ}$C for 6 h, (c) 300 $^{\circ}$C for 12 h, (d) 400 $^{\circ}$C for 6 h and (e) 400 $^{\circ}$C for 12 h.

The pattern of the as-synthesized $LiCoO_2$ presents an amorphous phase. Using the calcination temperature of 300 °C for 6 and 12 h, XRD reveals that the sample is composed of $LiCoO_2$ phase (JCPDS 44-0145) and Co_3O_4 phase (JCPDS 42-1467). As the calcination temperature increased to 400 °C for 6 h, the XRD pattern shows a single-phase of $LiCoO_2$. The sharp diffraction lines of $LiCoO_2$ at 2θ = 19.06, 37.56, and 45.38 correspond to (003), (101), and (104) reflections, respectively. These patterns are indexed as a rhombohedral structure (JCPDS 44-0145). The crystallite size of $LiCoO_2$ is estimated from the widths of the diffraction line of 003, 101, and 104 planes using the Scherer equation in Table 4.1. It can be observed that the prepared $LiCoO_2$ crystallites are in the nanosize range.

Table 4.1 Crystallite sizes of calcined $LiCoO_2$ samples at 400 °C

Calcined condition	Crystallite size (nm)*			
	L_{003}	L_{101}	L_{104}	$L_{average}$
400 °C, 6 h	21.5	21.1	22.3	21.6±0.6
400 °C, 12 h	23.4	22.5	23.2	23.0±0.5

* The data were calculated, based on the Scherer method by the MDI Jade software.

4.1.2 Transmission electron microscope (TEM)

Figure 4.2 shows the TEM images of the calcined $LiCoO_2$ at 400 °C for 6 h. It can be observed that the average particles size have diameters about 25 nm, which agrees well with the data obtained from XRD studies (Table 4.1). The individual crystallite of $LiCoO_2$ is shown in the high-resolution lattice image (Figure 4.2-d). This image presents a well-defined layered structure of cobalt oxide. Furthermore, TEM images do not show other morphologies except sheet-like particles; therefore, layered $LiCoO_2$ is the dominant phase.
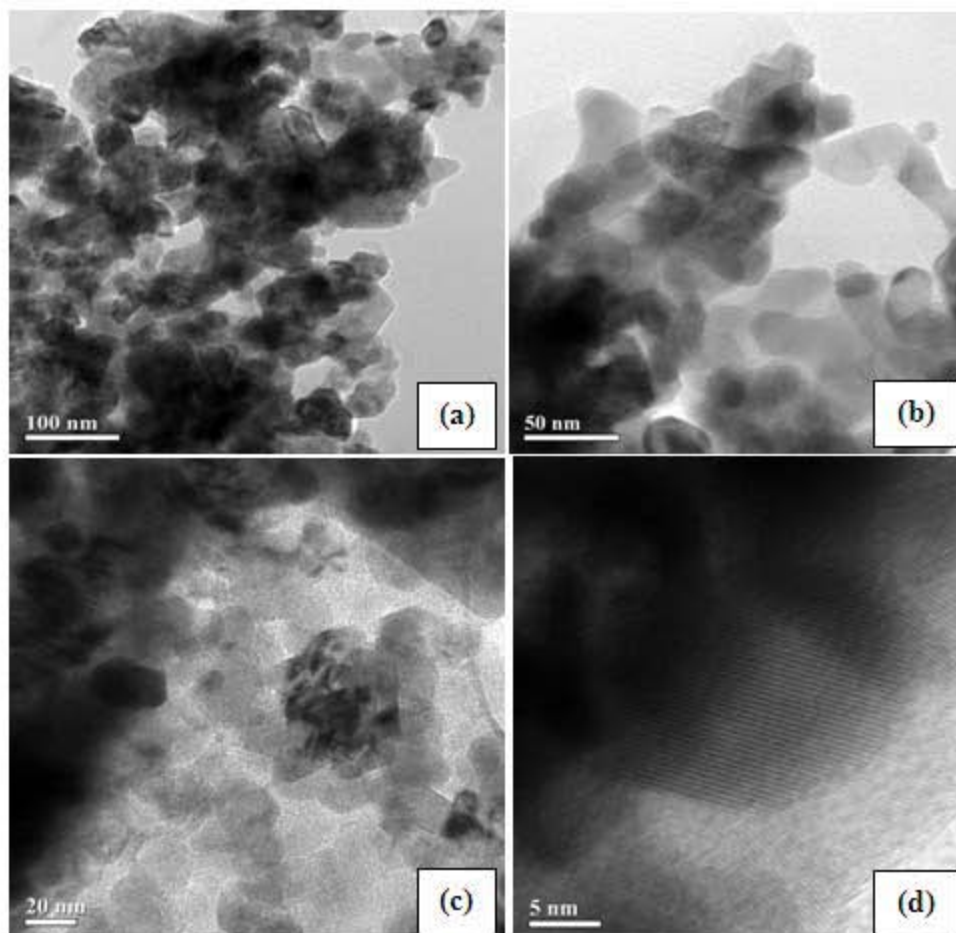
Figure 4.2   TEM images of the calcined $LiCoO_2$ at 400 °C for 6 h.

4.2   Synthesis and characterization of $LiCo_{1-x}Mn_xO_2$ powders

The $LiCo_{1-x}Mn_xO_2$ (x = 0.0 - 1.0) powders were synthesized by the same method. The as-synthesized $LiCo_{1-x}Mn_xO_2$ was calcined in the range of 400 - 700 °C for 6 h to obtain the single-phased $LiCo_{1-x}Mn_xO_2$.

4.2.1 Crystal structure and crystal size of calcined $LiCo_{1-x}Mn_xO_2$

The XRD patterns of the $LiCo_{1-x}Mn_xO_2$ (x = 0.0 - 1.0) calcined at 400 and 500 °C for 6 h are shown in Figure 4.3 and 4.4, respectively.
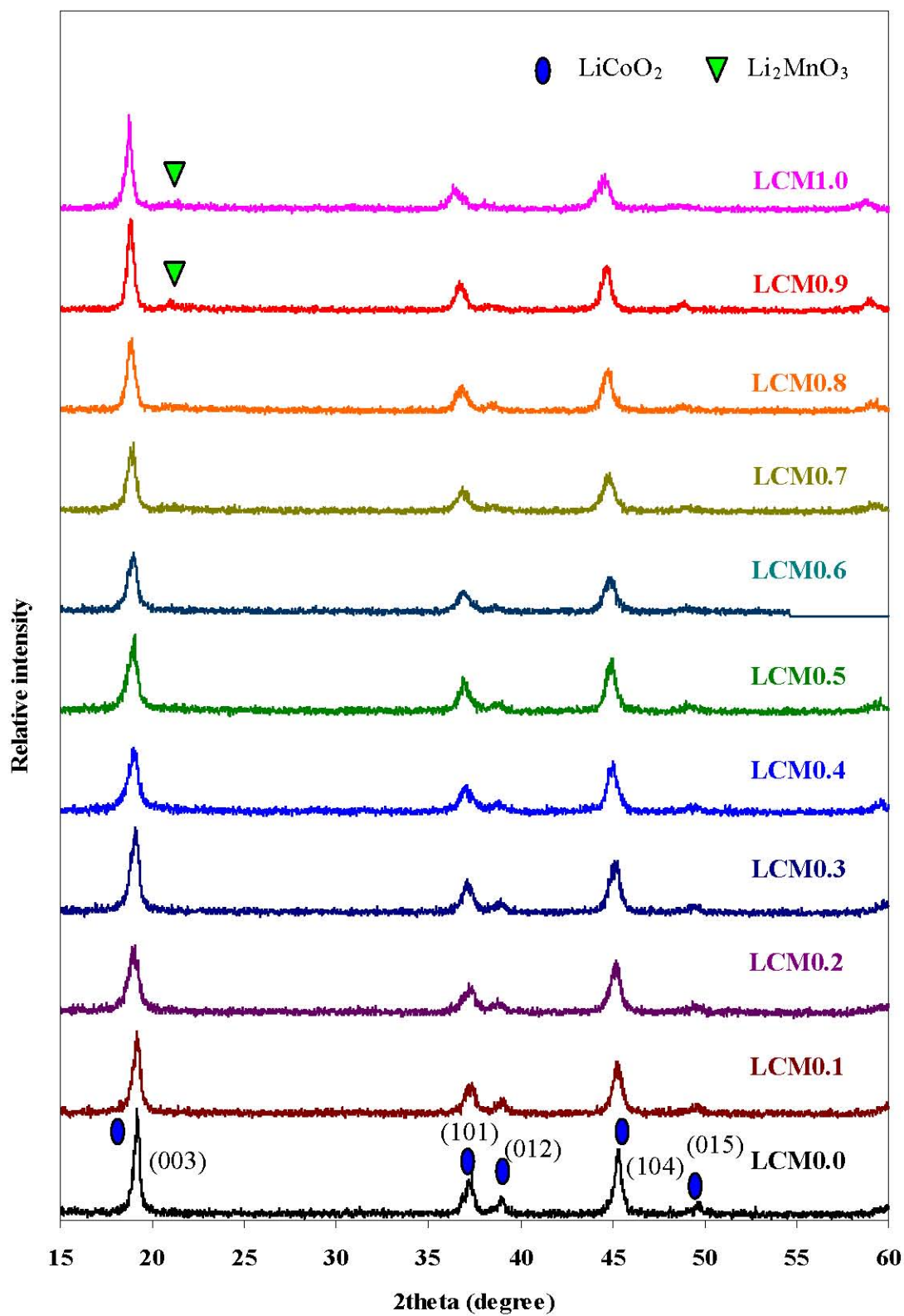
Figure 4.3 XRD patterns of $LiCo_{1-x}Mn_xO_2$ (x = 0.0 - 1.0) calcined at 400 $^{\circ}$C for 6 h.
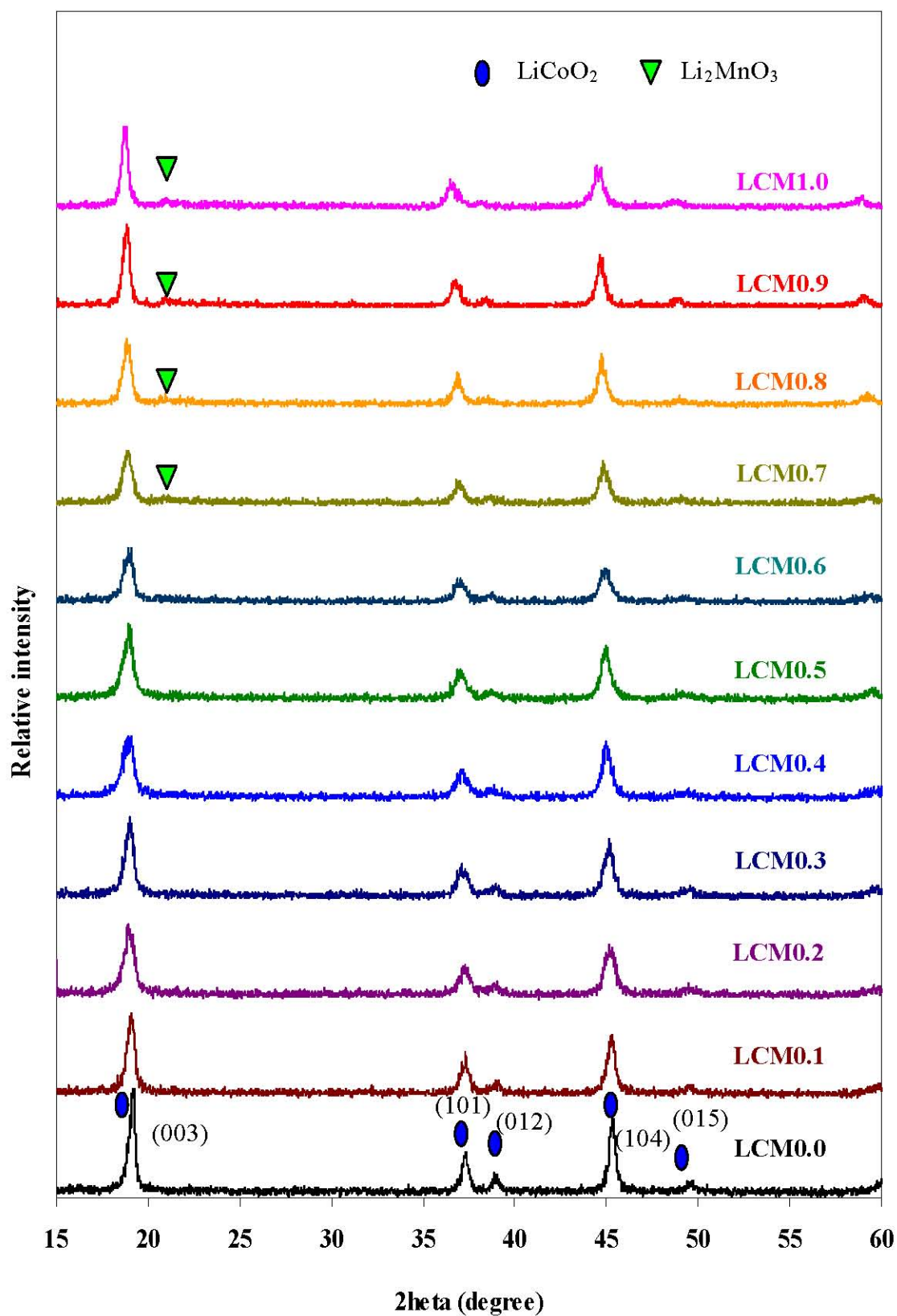
Figure 4.4 XRD patterns of $LiCo_{1-x}Mn_xO_2$ (x = 0.0 - 1.0) calcined at 500 ^{o}C for 6 h.

Figure 4.3 shows XRD patterns of $LiCo_{1-x}Mn_xO_2$ (x = 0.0 - 1.0) calcined at 400 °C for 6 h. As x = 0.0 - 0.8, the samples appear to be a single-phased $LiCoO_2$. As x = 0.9 and 1.0, the small peak of an impurity phase (Li_2MnO_3; JCPDS 27-1252) at 22 ° was observed. When the samples were calcined at 500 °C for 6 h (Figure 4.4), the patterns of compounds with x = 0.7 - 1.0 contains the Li_2MnO_3 phase (JCPDS 27-1252). It can be concluded that the single-phased $LiCoO_2$ were observed for Mn-doping up to x = 0.6. However the board peaks of the patterns refer to the small crystallite size of samples which may cause the difficulty to maintain the layered structure of the samples during the exfoliation process. In the colloid preparation, using ultrasound radiation causes cavitation phenomenon. This phenomenon creates high impact energy to the solid surface and high temperature of the solution that may causes the degradation of the unstable layered structure. To obtain the stability of single-phased $LiCo_{1-x}Mn_xO_2$ with optimized ratio of Mn/Co, the samples were calcined at 700 °C for 6 h. Furthermore, the patterns of all samples calcined at 400 °C and 500 °C have too low intensity of characteristic peaks to calculate the lattice parameters. Thus, the lattice parameters of LCMx calcined at 700 °C are calculated.

Figure 4.5 illustrates XRD patterns of $LiCo_{1-x}Mn_xO_2$ (x = 0.0 - 1.0) calcined at 700 °C for 6 h. The intense diffraction lines of LCM0.0 at 2θ = 19.02, 37.48, 38.48, 39.16, 45.30, 49.50 and 59.70 correspond to (003), (101), (006), (012), (104), (015) and (107) reflections, respectively. These diffraction patterns are indexed as a rhombohedral structure, similar to that of $LiCoO_2$ (JCPDS 50-0653, simulated in Figure 4.6).
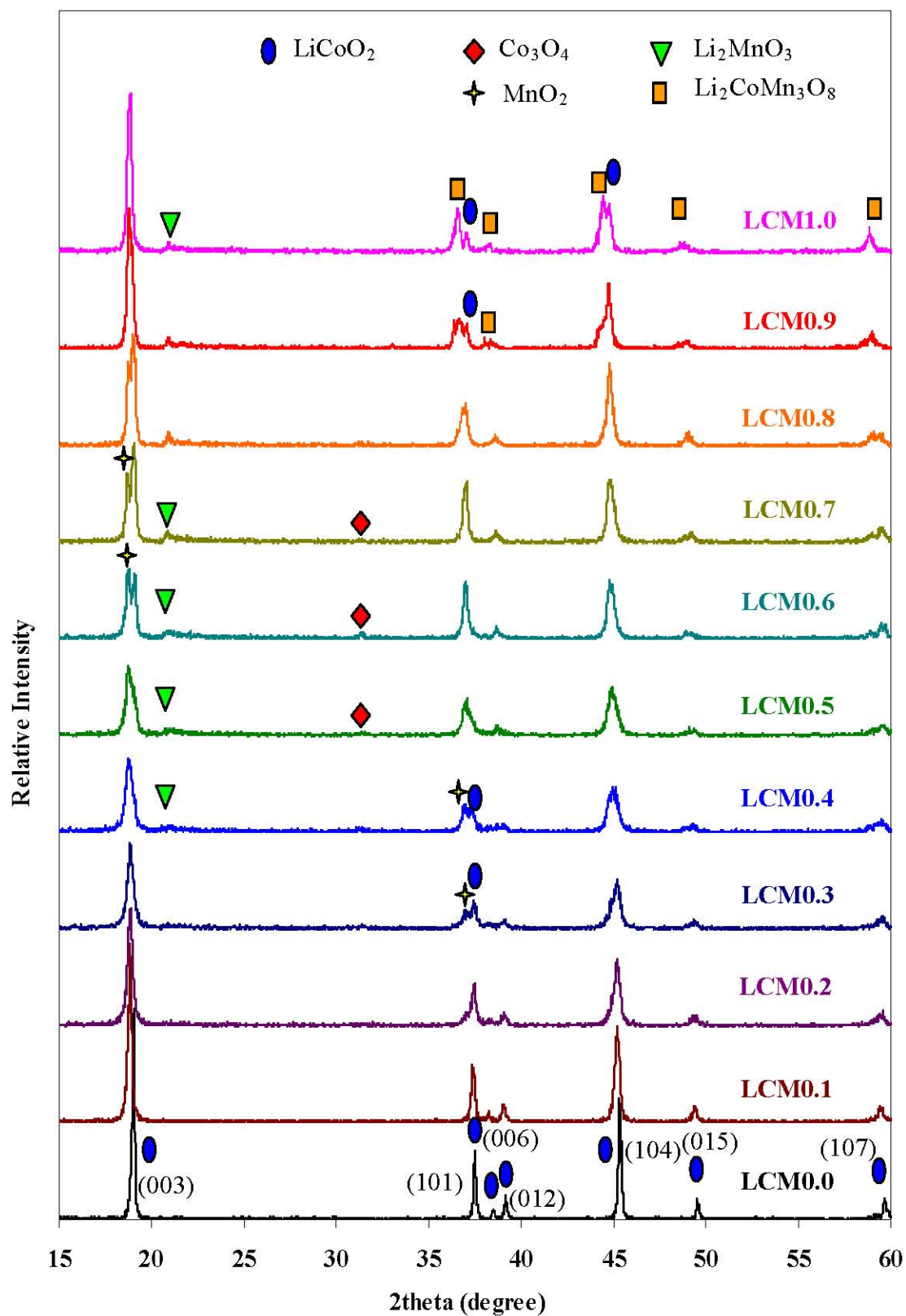
Figure 4.5 XRD patterns of $LiCo_{1-x}Mn_xO_2$ (x = 0.0 - 1.0) calcined at 700 ^oC for 6 h.
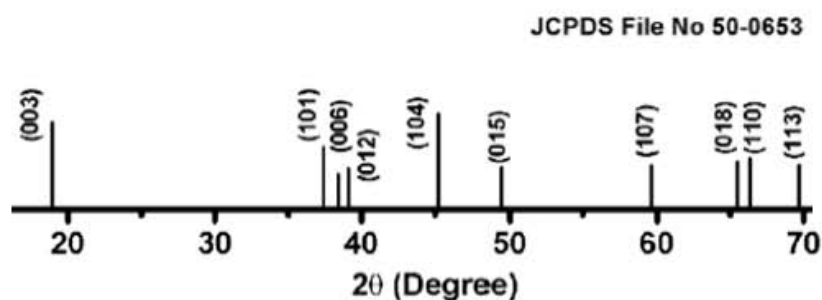
Figure 4.6 Simulated XRD pattern of $LiCoO_2$ from JCPDS: 50-0653.

The single-phased oxides were found for Mn doping up to x = 0.2. The secondary phases were found in the samples with the x = 0.3 − 1.0. These impurity phases were identified as MnO_2 phase (JCPDS 42-1169), Li_2MnO_3 (JCPDS 27-1252) and Co_3O_4 (JCPDS 42-1467). Furthermore, the samples with x is 0.9 and 1.0 are the mixed phase of Li_2MnO_3, $LiCoO_2$ and $Li_2CoMn_3O_8$ (JCPDS 48-0261). With increasing Mn content in the single phased LCMx (x = 0.1 and 0.2), the XRD intensities of all peaks decrease. Moreover, the (003) peak, slightly shifted to a lower angle with an increase in Mn content. To obtain the lattice parameters for each composition in Table 4.2, the (003), (101) and (104) reflections were chosen because of their high intensities. Substitution of Co by Mn results to the expansion of the unit cell parameters consistent with the differences in size between Co^{3+} and Mn^{3+} (Co^{3+} = 0.56 Å and Mn^{3+} = 0.63 Å). The result agrees well with Caballero *et al.* [24] and Suresh *et al.* [26].

Table 4.2 Lattice parameters and d-spacings of single-phased $LiCo_{1-x}Mn_xO_2$ calcined at 700 °C for 6 h

Samples	d_{003} (Å)	Lattice parameter (Å)		
		a	*c*	*c/a*
LCM0.0	4.6655±0.0152	2.8116±0.0031	13.9966±0.0457	4.9781±0.0117
LCM0.1	4.7046±0.0031	2.8132±0.0024	14.1139±0.0091	5.0151±0.0026
LCM0.2	4.7095±0.0097	2.8143±0.0018	14.1285±0.0292	5.0202±0.0082

The crystallite sizes of single-phased oxides are calculated from the XRD patterns using the Scherer method, using a full width at half maximum of shaper and clearer peaks of (003), (101) and (104) reflections as shown in Table 4.3. The data indicates that the crystallite sizes of synthesized $LiCo_{1-x}Mn_xO_2$ are in the nanosized range. Furthermore, the crystallite size decreases with an increase of x from 0.0 to 0.2.

Table 4.3 The crystallite sizes of single-phased $LiCo_{1-x}Mn_xO_2$ (x = 0.0 - 0.2) calcined at 700 °C for 6 h

Samples	Crystallite size (nm)*			
	L_{003}	L_{101}	L_{104}	$L_{average}$
LCM0.0	66.9	89.8	58.2	71.6±16.3
LCM0.1	39.6	39.8	32.3	37.2±4.3
LCM0.2	26.4	29.4	23.6	26.5±2.9

* The data were calculated, based on the Scherer method by the MDI Jade software.

The effect of the calcination temperature at 400 – 700 °C towards the crystallinity is shown in Figure 4.7. As the temperatures increase (400, 500 and 700 °C), the crystallite size of all samples is risen indicating the gradual growth in the particle size [88]. The growth of the particle size results from the rearrangement of the atoms in the samples through diffusion at high temperature.
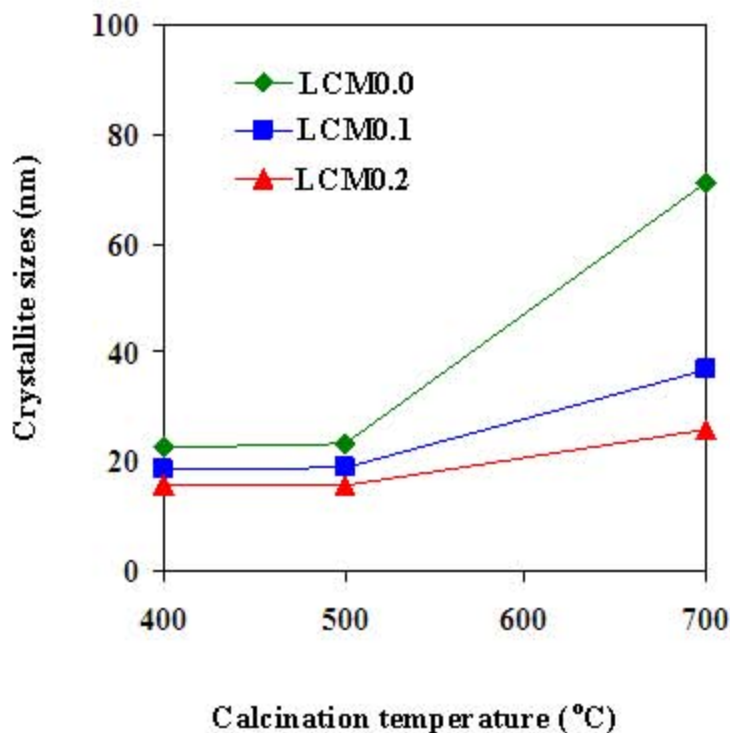
Figure 4.7 Crystallite sizes of single-phased $LiCo_{1-x}Mn_xO_2$ (x = 0.0 - 0.2) using various calcined temperatures of 400 – 700 $^{\circ}$C.

4.2.2 Transmission electron microscope (TEM)

Figure 4.8 shows TEM images of LCM0.0, LCM0.1 and LCM0.2. It can be observed that the LCM0.0, LCM0.1 and LCM0.2 have diameters in the range of 50 - 100 nm, 40 - 60 nm and 25 - 50 nm, respectively. The Mn doping apparently leads to the reduction of particle size. This result agrees well with the data obtained from XRD studies (Table 4.3).

LCM0.0
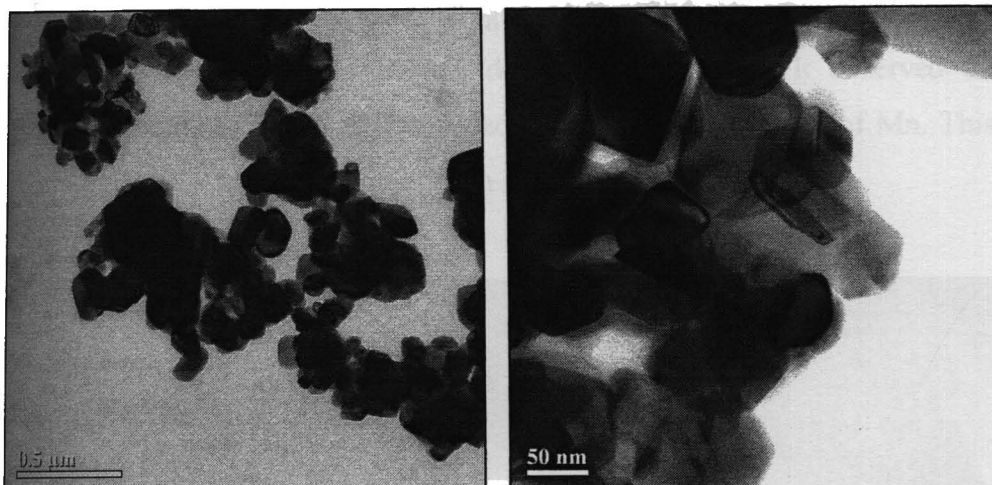
LCM0.1
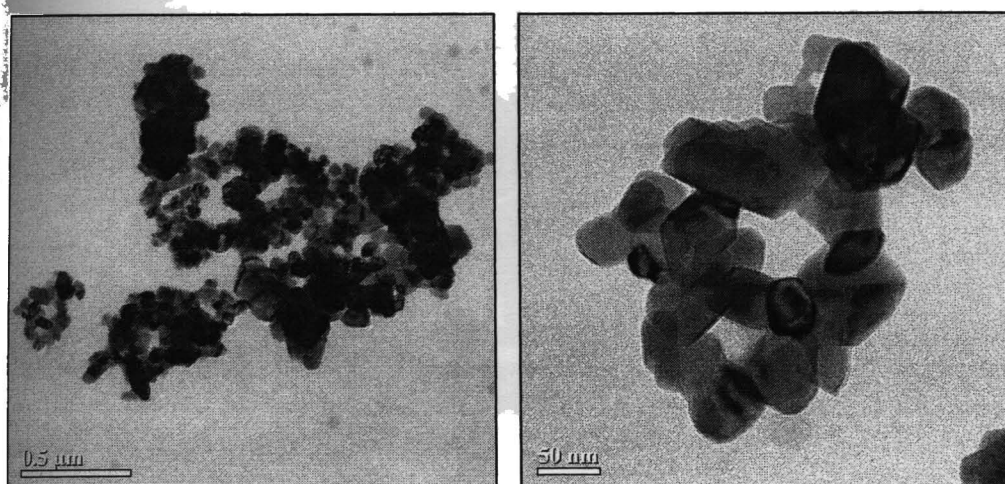
LCM0.2
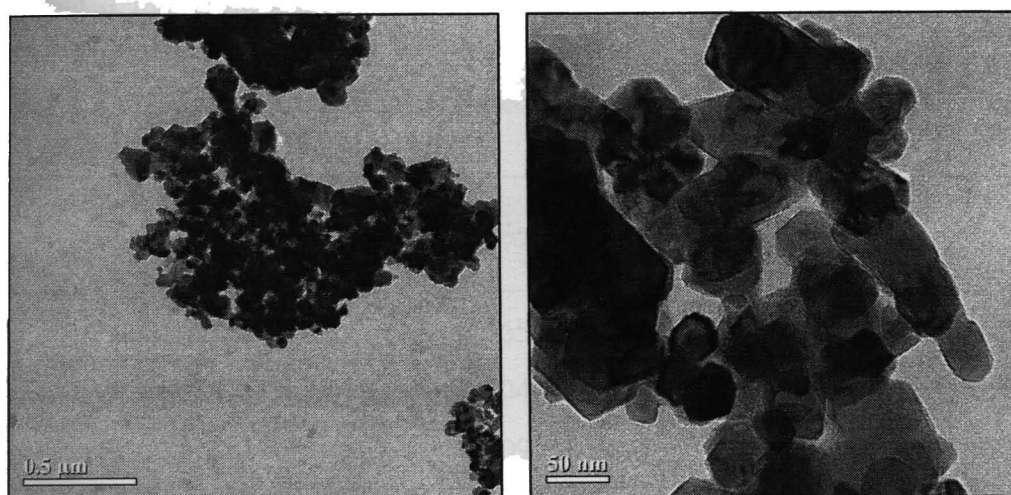
Figure 4.8 TEM images of single-phased $LiCo_{1-x}Mn_xO_2$ calcined at 700 ^{o}C for 6 h.

The individual crystallites of $LiCo_{1-x}Mn_xO_2$ (x = 0.0 - 0.2) is shown in the high-resolution lattice images (Figure 4.9). These images present a layered structure and the d-spacings of Mn doping-cobalt oxides. It observed that, the distances of between layers are expanded with increasing amount of Mn. This result concurs well with the data obtained from XRD studies (Table 4.4).
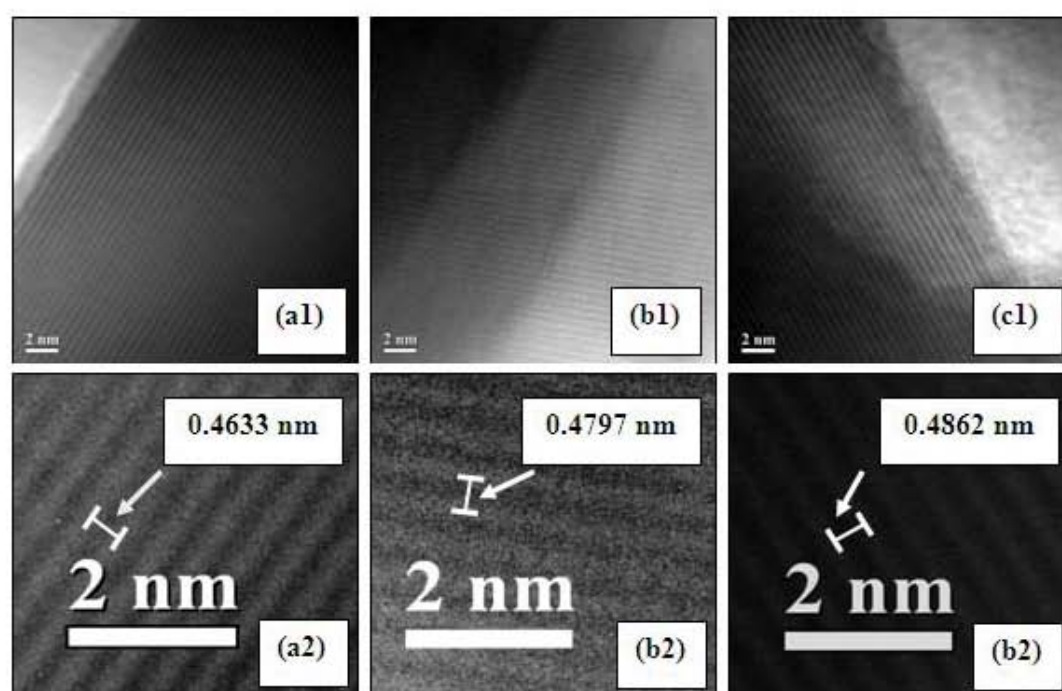
Figure 4.9 High resolution TEM images of (a) LCM0.0, (b) LCM0.1 and (c) LCM0.2 calcined at 700 °C for 6 h.

Table 4.4 The d-spacings of single-phased $LiCo_{1-x}Mn_xO_2$ calcined at 700 °C for 6 h

Samples	d_{003} (nm)	
	XRD	TEM
LCM0.0	4.6655±0.0152	0.4633±0.0063
LCM0.1	4.7046±0.0031	0.4797±0.0054
LCM0.2	4.7095±0.0097	0.4862±0.0082

4.2.3 Fourier transform infra-red spectroscopy (FT-IR)

Figure 4.10 shows the FT-IR spectra of single-phased $LiCo_{1-x}Mn_xO_2$ calcined at 700 °C for 6 h. All samples show the four characteristic peaks in the range 500-700 cm^{-1}, which are attributed to the asymmetric stretching CoO_6 and MnO_6 groups. This observation is similar to that Rao *et al.* [89], Tao *et al.* [90], Kalyani *et al.* [14] and Li *et al.* [90]. While the stretching mode of LiO_6 octahedron is observed in the far-infrared region around 240 - 270 cm^{-1} [91] but that region is not covered here. A summary of peak position assignments is provided in Table 4. 5.
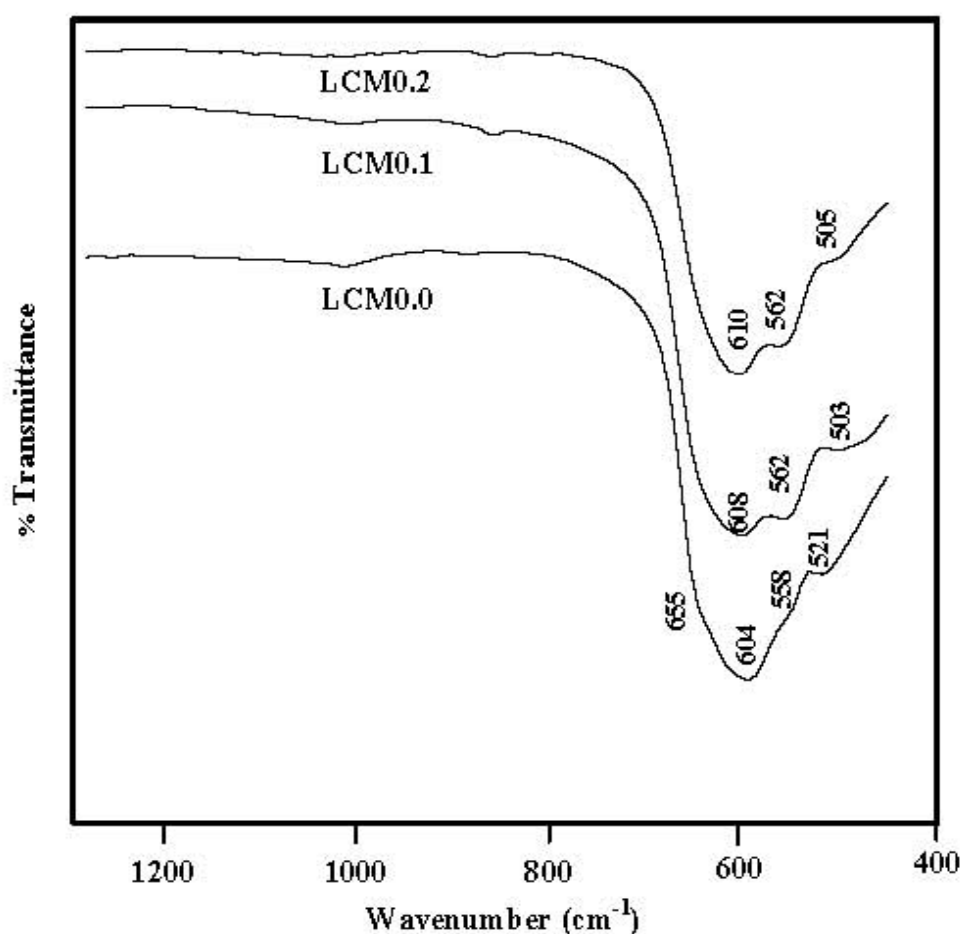
Figure 4.10 FT-IR spectra of single-phased $LiCo_{1-x}Mn_xO_2$ calcined at 700 °C for 6 h.

Furthermore, the peak at 521 cm^{-1} of LCM0.0 shifts towards lower wavenumbers (~503 - 505 cm^{-1}) as the Mn content increases (x = 0.1 and 0.2). The shifting of this vibration peak results from a decrease in the strength of Co-O

interaction due to the expansion of the lattice parameter from the substitution of Co (III) ions in LCM0.0 by the larger Mn (III and IV) ions [92-93].

Table 4.5 FT-IR peak positions and assignments of single-phased $LiCo_{1-x}Mn_xO_2$ calcined at 700 ^oC for 6 h

Literature values (ν, Cm^{-1})				Observed values (ν, Cm^{-1})			Assignment
$LiCoO_2$ [89]	$LiCoO_2$ [88]	$LiMn_2O_4$ [90]	$LiMn_2O_4$ [14]	LCM 0.0	LCM 0.1	LCM 0.2	
		507	510		503	505	ν_{as}-MnO$_6$[a]
525	520			521	-	-	ν_{as}-CoO$_6$[b]
556	575			558	562	562	ν_{as}-CoO$_6$[b]
597	605			604	608	610	ν_{as}-CoO$_6$[b]
		613	620				ν_{as}-MnO$_6$[a]
651	660			655			ν_{as}-CoO$_6$[b]

ν_{as} = asymmetric stretching

[a] Ref. [14, 91]

[b] Ref. [89]

4.2.4 Chemical composition of the single-phased of $LiCo_{1-x}Mn_xO_2$

The chemical composition of the single-phased oxides was analyzed by ICP-AES as shown in Table 4.6. In all cases, the analyzed compositions are close to the targeted chemical composition. Substitution of Co (III) ions in $LiCoO_2$ by Mn (III and IV) ions results to a decrease in the lithium content. From the calculation (shown in appendices 4), the oxidation number of Mn in LCM0.1 and LCM0.2 is about 3.20 and 3.15, respectively. Furthermore, the less amount of lithium cations by Mn-doping suggests the reduced charges of cobalt manganese oxide layered sheets.

Table 4.6 Chemical compositions of single-phased $LiCo_{1-x}Mn_xO_2$ calcined at 700 $^{\circ}$C for 6 h

Samples	Stoichiometry			Composition
	Li/(Co+Mn)	Co/(Co+Mn)	Mn/(Co+Mn)	
LCM0.0	1.00	1.00	-	$Li_{1.00}Co_{1.00}O_2$
LCM0.1	0.98	0.90	0.10	$Li_{0.98}Co_{0.90}Mn_{0.10}O_2$
LCM0.2	0.97	0.80	0.20	$Li_{0.97}Co_{0.80}Mn_{0.20}O_2$

4.3. Characterization of HCMx

Some layered transition metal oxides are not active for intercalation process because of the difficulty associated with the intercalation of guest molecules. This resistance to intercalation is attributed to the higher charge density of the sheets [95]. Generally, layered oxides can be converted into the proton-exchanged forms and preserved their layer structure [30, 32, 46]. Proton-exchanged layered compounds with low negative charge densities [95]. Allow high degree of intercalation that means the easy incorporation of a wide variety of guests such as cations and organic molecules into the interlayer [96]. In many cases, proton-exchanged forms were used as starting materials to prepare colloids and thin films [31, 42-43]. In this thesis, the proton-exchanged form of $LiCo_{1-x}Mn_xO_2$ was obtained by stirring the powder in an acid solution.

4.3.1 X-ray diffraction (XRD)

The XRD patterns of the single-phased $LiCo_{1-x}Mn_xO_2$ calcined at 700 $^{\circ}$C for 6 h and their proton-exchanged form are shown in Figure 4.11.
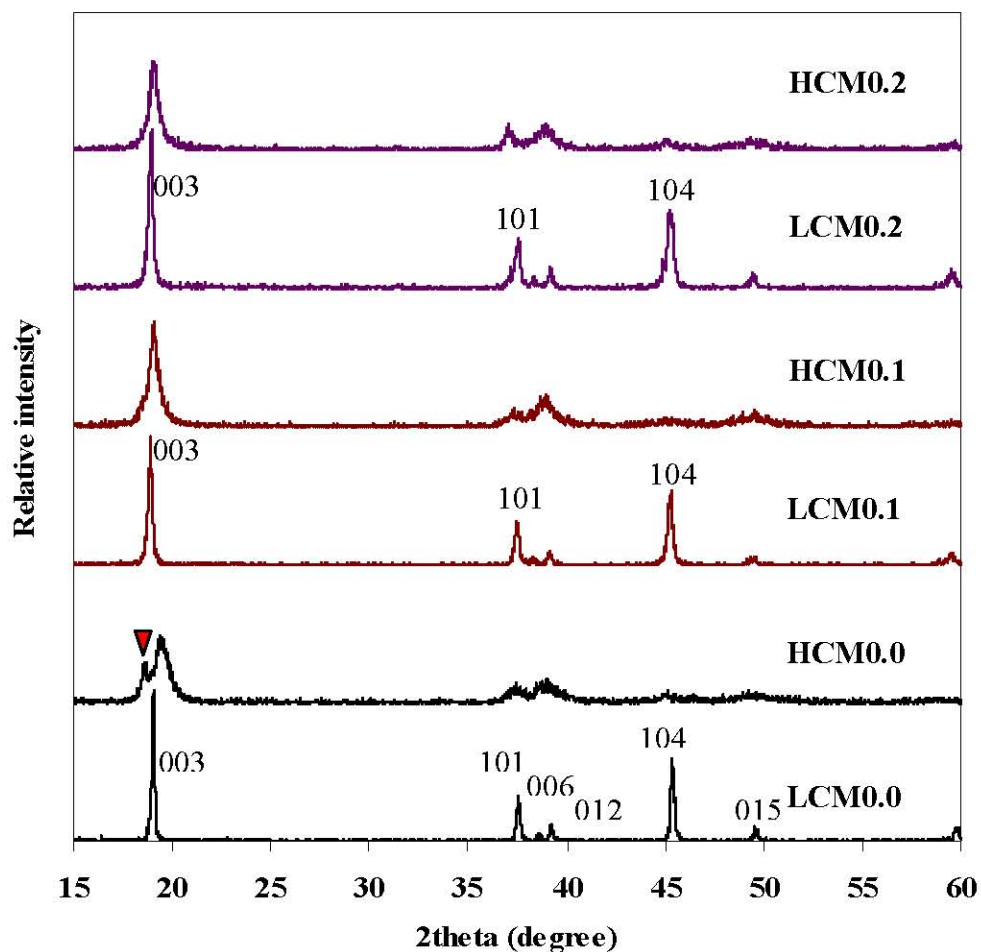
Figure 4.11 XRD patterns of single-phased $LiCo_{1-x}Mn_xO_2$ calcined at 700 ^oC for 6 h and their proton-exchanged form. (▼ Indicates that the proton exchanged reaction is not complete).

From the patterns, the (003), (101) and (104) peaks of HCM0.0, HCM0.1 and HCM0.2 are broaden after the proton-exchanged process. The peaks broadening results from the structural deformation by acid treatment, leading to the smaller particle size [96]. The pattern of HCM0.0 presents the mixture phase between LCM0.0 and HCM0.0, indicating that the proton-exchanged reaction was incomplete. The incomplete ion-exchange was found in LCM0.0 because it has larger crystallite size compared to LCM0.1 and LCM0.2 have. The large crystallites have less external surface area to contact with the acid solution; therefore, the diffusion of proton into the layered structure requires longer time. The crystallite sizes of HCMx are estimated from (003) reflection, reported in Table 4.7. The data indicates that the crystallite sizes of LCMx and HCMx are in the nanosized range. The crystallite sizes of

HCM0.1 and HCM0.2 are smaller than LCM0.1 and LCM0.2, respectively, while that of HCM0.0 is not reported because of the broaden and overlap peaks of the mixture phase.

Table 4.7 Crystallite sizes of single-phased $LiCo_{1-x}Mn_xO_2$ calcined at 700 $^{\circ}$C for 6 h and their proton-exchanged form

Samples	Crystallite size (nm)[a]
LCM0.0	71.6
LCM0.1	37.2
LCM0.2	26.5
HCM0.0	-[b]
HCM0.1	16.8
HCM0.2	18.6

[a] The data were calculated, based on the Scherer method by the MDI Jade software.

-[b] Proton-exchanged reaction is not complete.

4.3.2 Transmission electron microscope (TEM)

Figure 4.12 shows TEM images of the HCM0.0, HCM0.1 and HCM0.2. It can be observed that the particles sizes of all samples decrease after proton-exchange. The trend of the particle size of HCMx is as the followings;

HCM0.0 > HCM0.1 > HCM0.2

HCM0.0
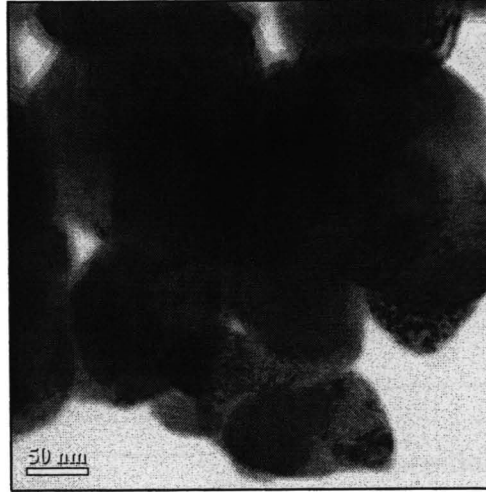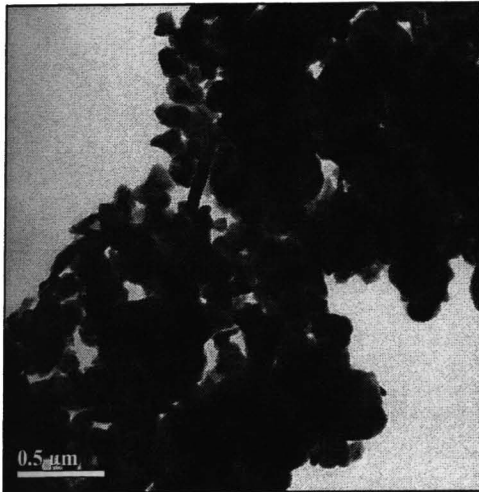
HCM0.1
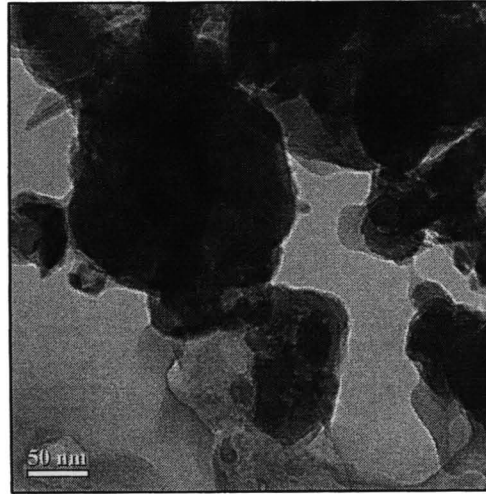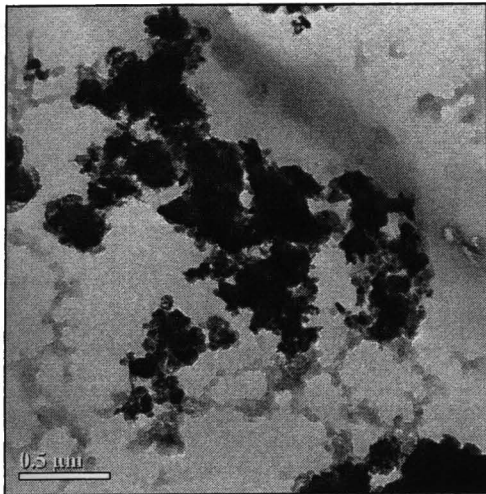
HCM0.2
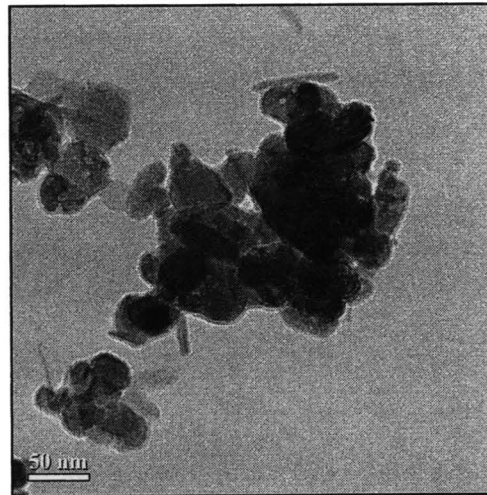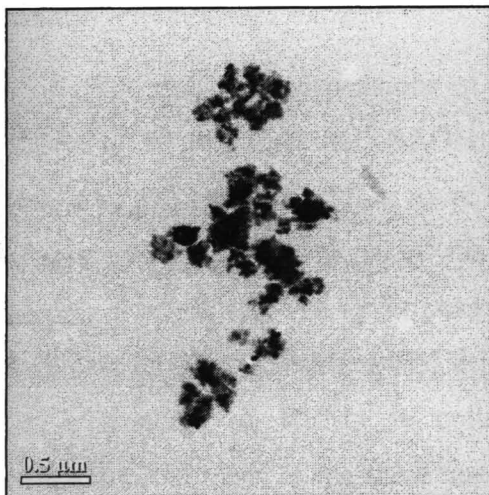
Figure 4.12 TEM images of HCMx.

4.3.3 Chemical composition of HCMx

The element compositions of LCMx samples before and after proton-exchange were analyzed by ICP-AES as shown in Table 4.8. It is noted that all lithium ions can not be replaced by protons.

Table 4.8 Chemical compositions of single-phased $LiCo_{1-x}Mn_xO_2$ samples before and after proton-exchange process

| Samples | Stoichiometry | | | | Composition |
| | H | Li | Co | Mn | |
	H/(Co+Mn)	Li/(Co+Mn)	Co/(Co+Mn)	Mn/(Co+Mn)	
LCM0.0	-	1.00	1.00	-	$Li_{1.00}Co_{1.00}O_2$
LCM0.1	-	0.98	0.90	0.10	$Li_{0.98}Co_{0.90}Mn_{0.10}O_2$
LCM0.2	-	0.97	0.80	0.20	$Li_{0.97}Co_{0.80}Mn_{0.20}O_2$
HCM0.0	0.88	0.12	1.00	-	$H_{0.88}Li_{0.12}CoO_2$
HCM0.1	0.83	0.15	0.89	0.11	$H_{0.83}Li_{0.15}Co_{0.89}Mn_{0.11}O_2$
HCM0.2	0.81	0.16	0.82	0.18	$H_{0.81}Li_{0.16}Co_{0.82}Mn_{0.18}O_2$

4.4 Characterization of colloid suspension

The colloidal suspensions of HCMx were obtained by dispersing 0.20 g of HCMx in 50 mL 0.04 M TBAOH solution (TBA/HCMx = 1). The mixture was shaken at 300 rpm for 24 h at room temperature, and then sonicated for 30 minutes. After sonication, the suspension was centrifuged at 3000 rpm for 10 min to remove the deposited phases. The upper phase (Up-HCMx) and deposited phase (Dep-HCMx) were cast on glass substrates and dried in air for 24h prior to characterize by XRD. The percentage of HCMx in colloidal suspension phase can be estimated by subtracting the mass of the solid that remained at the bottom of the glass bottle from the initial mass (0.20 g). Thus, the calculated amounts of the solid oxides in

dispersion phase of HCM0.0, HCM0.1 and HCM0.2 are about 6, 11 and 29 wt%, respectively.

4.4.1 X-ray diffraction (XRD)

The deposited solid and the colloidal suspension of HCMx (HCM0.1 and HCM0.2) after exfoliation process were cast on glass slides and dried at room temperature. Their XRD patterns are shown in Figure 4.13. For all cases, the patterns of the deposited solid are similar to the HCMx, referred that the TBA^+ cannot intercalate into layered structure. On the other hand, the patterns of colloidal suspension appeared two noticeable basal spacing of 4.67 Å and 11.50 Å. The former is due to HCMx phase, and the latter is assigned to a TBA^+ intercalated phase. The free TBA^+ ion is a spherical-liked shape with the size in the range of 9.50 - 10.50 Å [97]. During an exfoliation process, the free TBA^+ ion can be intercalated into the confined space between layered structure, then its spherical-like shape could change because of the electrostatic interaction. The size of TBA^+ ion in the space between layered host (11.50 - 4.67 = 6.83 Å) is smaller than the free ion because of the attractive interaction between TBA^+ cation and negative-charged layer of host. In order to increase the attractive force, the distance between opposite charges should be shorten; therefore, the alkyl chains of TBA^+ ion rearrange themselves and the spherical-liked shape becomes flatter [28-29].

Not only the TBA^+ intercalated phase, the XRD patterns of Up-HCM0.1 and Up-HCM0.2 also show a starting HCMx phase with d-spacing about 4.67 Å, indicating the incomplete intercalation of TBA^+ ion, leading to the imperfect exfoliation of HCMx in solution. In addition, the colloidal suspension of HCM0.0 is not stable in this condition. Thus, the XRD of Up-HCM0.0 is not available.
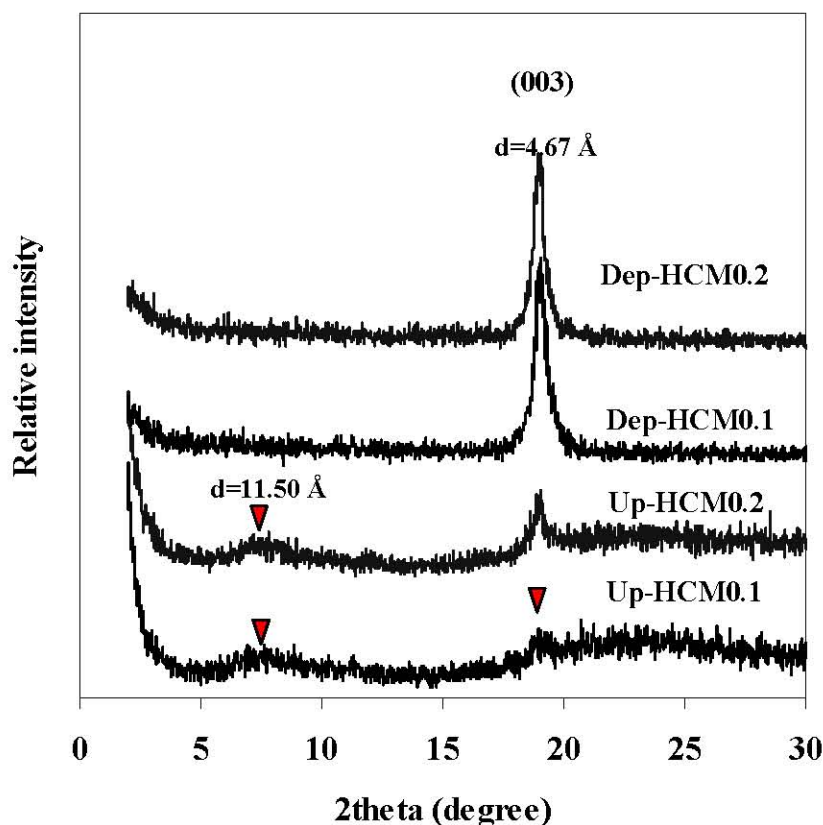
Figure 4.13 XRD patterns of colloidal suspension (Up-HCMx) and deposited solid (Dep-HCMx) of HCMx.

4.4.2 Tyndall effect

The colloidal suspensions of HCMx samples were obtained using the procedure above. Figure 4.14 (a) shows photographs of the colloidal suspensions of HCM0.0, HCM0.1 and HCM0.2. The color of the colloids was varied from colorless to dark-brown, depending on the Mn content. However, the colloidal suspension of HCM0.0 was not stable, this result may cause from the larger particles and higher charged layers of HCM0.0 compared with the other samples. Figure 4.14 (b) shows the light scattering of the HCMx suspension. It observed that the suspension of HCM0.1 and HCM0.2 exhibits the Tyndall effect but the suspension of HCM0.0 is not present. This effect shows the characteristic property of a colloid.

HCM0.0　　HCM0.1　　HCM0.2　　　HCM0.0　　HCM0.1　　HCM0.2
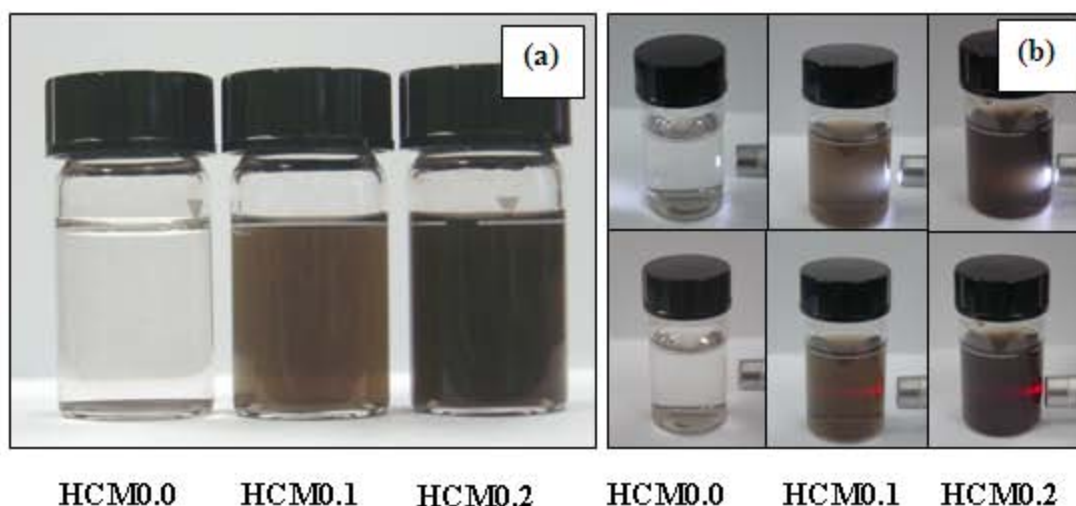
Figure 4.14 (a) Photographs of the colloidal suspensions of HCMx (diluted by 10-fold with Milli-Q water) and (b) the demonstration of Tyndall effect.

4.4.3 UV-Vis spectroscopy

Figure 4.15 shows UV-Vis spectra of the prepared colloidal suspensions of HCM0.1 and HCM0.2. The spectra exhibits optical absorption with a broad peak centered on 254 nm and 244 nm, respectively. In the case of HCM0.0, the spectrum does not appear because of the unstable colloid. The broad peaks of colloidal suspension HCM0.1 and HCM0.2 are ascribed to the combination of a characteristic absorption peak of the exfoliated HCM0.2 and the scattering from its larger particles in suspension. The peak of HCM0.2 suspension with the highest absorbance could be explained as HCM0.2 was dispersed in higher amount than the other two oxides, because the HCM0.2 has smaller particles size and lower charged layers than HCM0.1 and HCM0.0, as discussed in sections 4.2.4 and 4.3.2. Furthermore, the substitution of Co by Mn results in the expansion of the space between CoO_2 sheets. Then, the interaction between CoO_2 sheets of HCM0.2 layers decreases, so that it can be more dispersed in TBAOH solution.
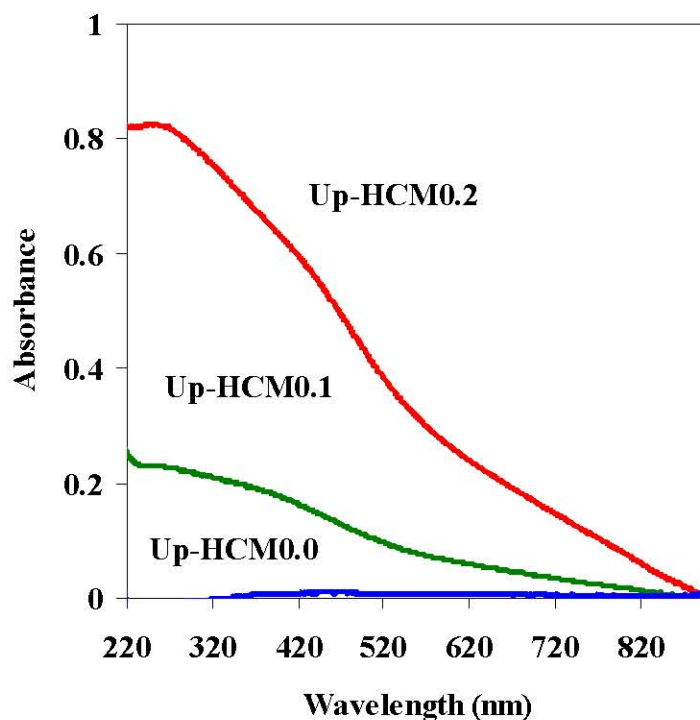
Figure 4.15 UV-Vis spectra of colloidal suspensions of HCMx in TBAOH solution (diluted by 50-fold with Milli-Q water).

4.4.4 The stability of colloidal suspension (Up-HCM0.1 and Up-HCM0.2)

Figure 4.16 shows the relationship between the turbidity of colloid and a suspension time. The turbidity of the colloid is decreased when the suspension time increases. This result may cause from the precipitation of the larger particles of HCMx over a standing period. On the other hand, the UV-Vis spectroscopy ensures the stability of colloids. Figure 4.17 shows the relationship between the maximum absorbance and a suspension time. The peak absorbance is slightly decreased even after standing for 10 day. Thus, the colloidal suspension of HCM0.1 and HCM0.2 is suitable for used as precursor for thin film preparation. This UV-Vis result contrasts with the turbidity because the UV-Vis absorption at the characteristic peak results from the nanosheets of HCMx, while the turbidity corresponds with the larger particles.
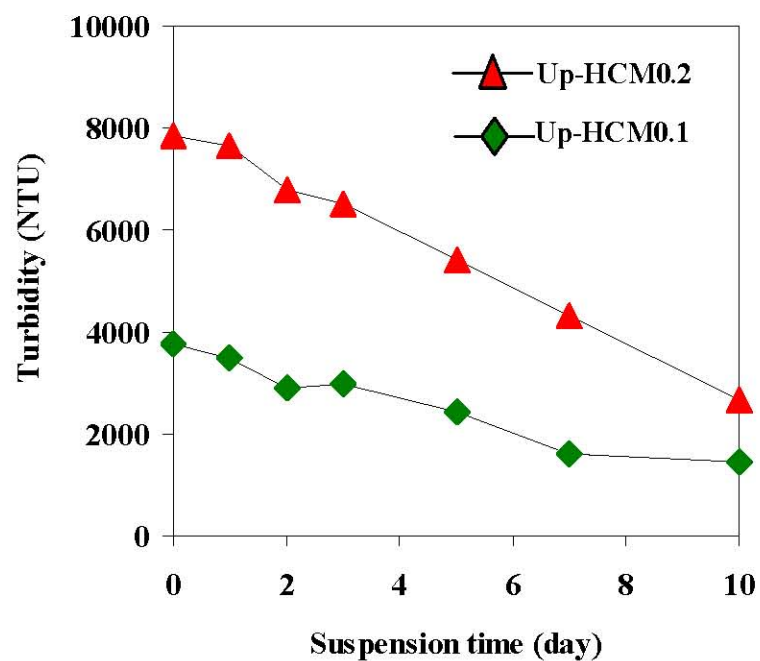
Figure 4.16 Relationship between a suspension time and a turbidity of colloid (diluted by 50-fold with Milli-Q water).
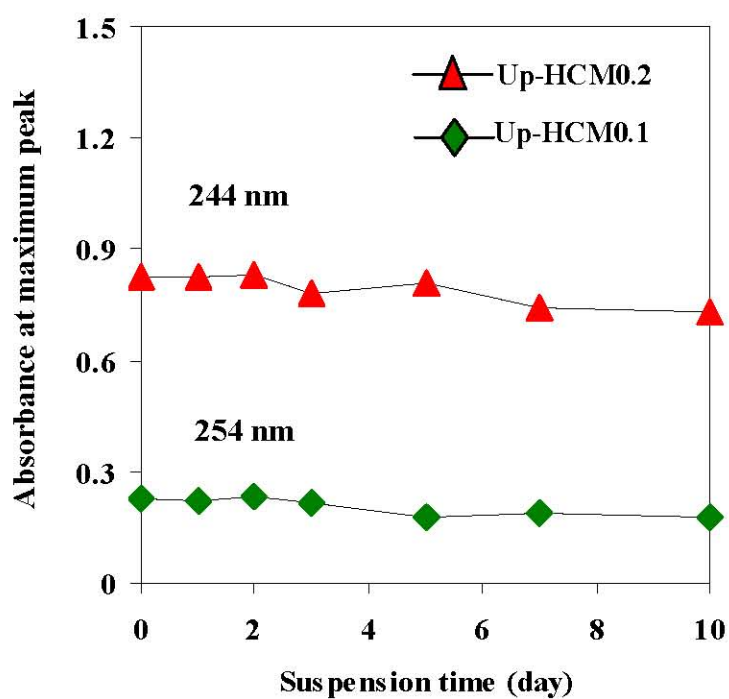
Figure 4.17 Relationship between a suspension time and a peak absorbance of colloid suspensions (diluted by 50-fold with Milli-Q water).

4.4.5 Transmission electron microscopy (TEM)

The morphology of HCMx powders and HCMx suspensions was examined by TEM as shown in Figure 4.18. The TEM images reveal that the HCMx sheets in colloids were not fully exfoliated but much more dispersed after shaking with TBAOH solution. The result also indicates that the sizes of Mn-doping cobalt oxides are about 5 - 10 nm (Figure 4.18 (c-d)).
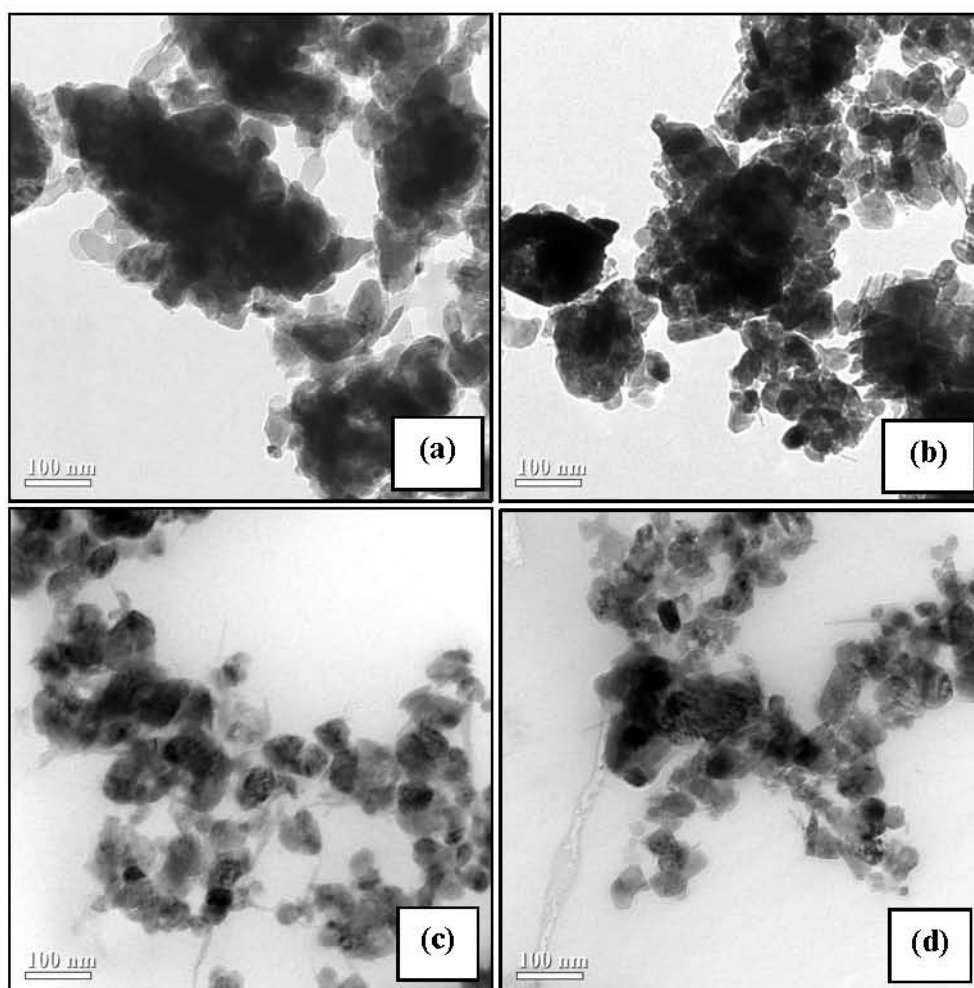
Figure 4.18 TEM images of (a) HCM0.1, (b) HCM0.2, (c) Up-HCM0.1 and (d) Up-HCM0.2.

Therefore it can be concluded that the HCMx colloidal suspensions are comprised of the HCMx nanoparticles and exfoliated Mn-doping cobalt oxides nanosheets. In the next experiment, HCM0.2 was chosen as the starting material for

study of the effect of TBAOH concentration and a sonicate time in exfoliation process.

4.4.6 Effect of TBAOH concentration

The effect of TBAOH concentration was studied with a fixed amount of 0.20 g HCM0.2 by varying the mole ratio of TBA/HCM0.2 in the range of 0.0 - 5.0. The dispersion condition was shaking at 300 rpm for 24 h and sonicating for 30 min. Figure 4.19 shows the photographs of Up-HCM0.2. After sonication, all sample showed the dark-brown suspension (Figure 4.20 (a)). Then, centrifuge at 3000 rpm for 10 min, the samples with TBA/HCM0.2 mole ratio in the range of 0.0 - 3.5 still contained the large amount of HCM0.2 in solution. As TBA/HCM0.2 = 5.0, the suspension presented the light-brown solution and the precipitate presented HCM0.2 in the bottom because of the ionic strength in the suspensions. Figure 4.19 (c) and (d) shows the photographs of Up-HCM0.2 diluted for 10-fold and 20-fold, respectively. It can be observed that, the TBA/HCM0.2 mole ratio of 0.5 - 1.0 had the highest dark-brown suspension, indicating to the largest amount of HCM0.2 in a solution.
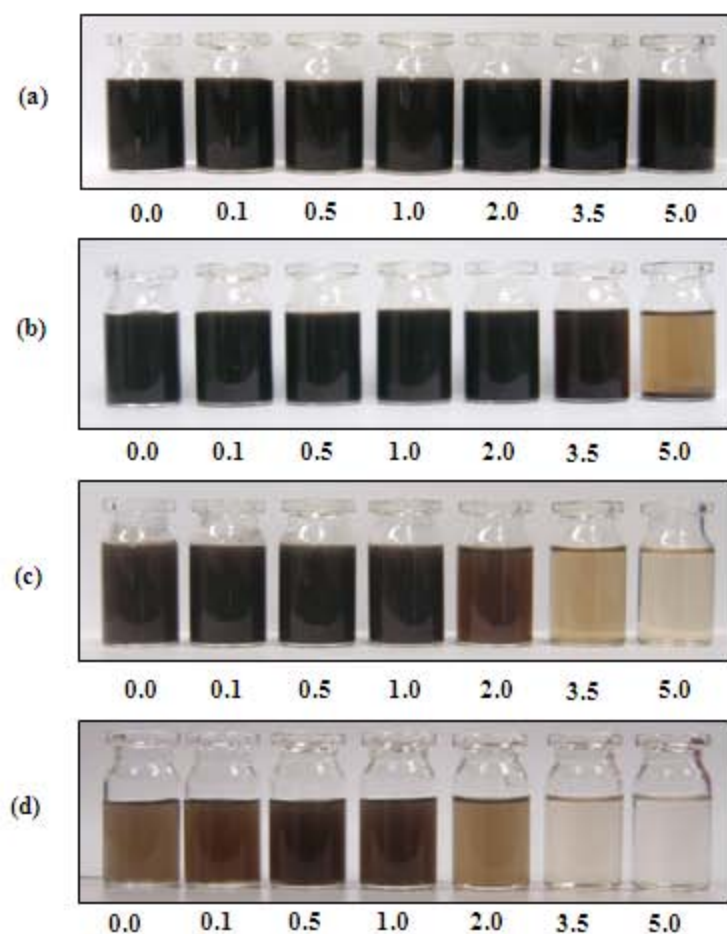
Figure 4.19 Photographs of Up-HCM0.2 with various mole ratio of TBA/HCM0.2 in the range of 0.0-5.0 (a) after sonication at 125 W for 30 min, and (b) after centrifugation at 3000 rpm for 10 min, (c) diluted by 10-fold, (d) diluted by 20-fold.

4.4.6.1 UV-Vis spectroscopy

Figure 4.20 (a) shows the absorption spectra of HCM0.2 suspensions with various molar ratios of TBA/ HCM0.2, and Figure 4.20 (b) shows the relationship between an absorbance (λ_{max}) at 244 nm and the mole ratio of TBA/HCM0.2. It can be observed that the spectrum with TBA/HCM0.2 = 0.5 have the highest absorption spectrum. However, with increasing the mole ratio of TBA/HCM0.2 higher than 0.5, the absorbance of the spectrum decreases as some solid precipitates. The result causes from the increase of the ionic strength in the suspensions. In the suspension, the region near a charged surface forms a double layer, consisted of a firmly bound layer (stern layer) and a diffuse layer. When

HCM0.2 particles approach each others, their surface induces electric potential fields and associates with a diffuse layer interaction, creating a repulsive force that can overcome the attractive van der Waals force, and keep the HCM0.2 particles separate. Increasing ionic strength reduces an electrostatic repulsion and thereby increases HCM0.2 particle aggregation and precipitation [99]. Bizeto *et al.* [100] reported the effect of mole ratio *n*-bultylamine/H$^+$-niobate on exfoliation process. With increasing the amine ratio, the amount of exfoliated niobate particles decreases.
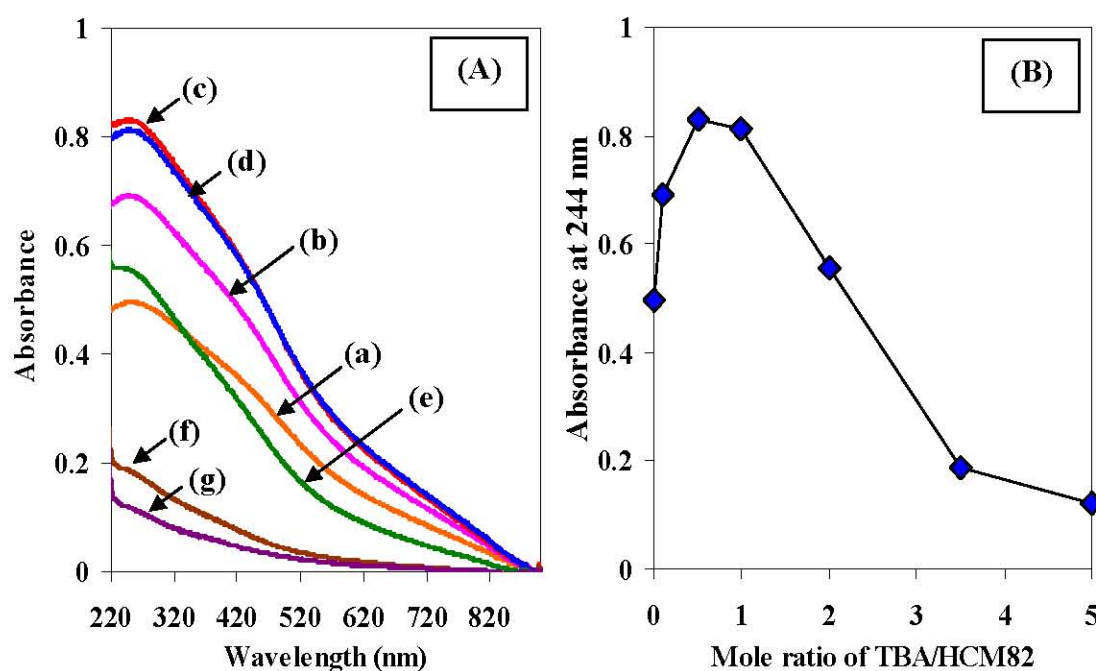
Figure 4.20 (A) The absorption spectra of Up-HCM0.2 (diluted by 50-fold with Milli-Q water) with various TBA/HCM0.2 of (a) 0.0, (b) 0.1, (c) 0.5, (d) 1.0, (e) 2.0, (f) 3.5 and (g) 5.0, and (B) the relationship between an absorbance at 244 nm (λ_{max}) and the mole ratio of TBA/HCM0.2.

4.4.6.2 X-ray diffraction (XRD)

XRD patterns, shown in Figure 4.21, of colloidal suspensions were recorded by cast the colloid on a glass slide and dried it at room temperature. At the mole ratio of TBA/HCM0.2 in the range of 1.0 - 3.5, the patterns are presented the TBA$^+$ intercalated phase with d-spacing about 11.5 Å. However, the pattern of all samples showed a small peak of HCM0.2 at 2theta about 19 degree indicated that the

exfoliation process is not fully complete. Figure 4.22 shows XRD patterns of deposited solids of the samples prepared with various TBA/HCM0.2. The patterns are similar to the pattern of a starting material HCM0.2; therefore, TBA$^+$ is can not intercalated into layered structure.
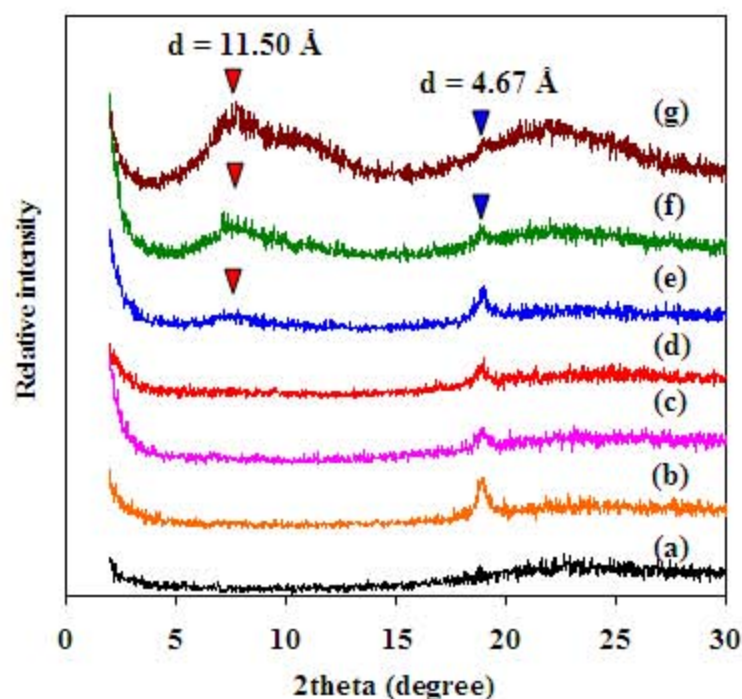
Figure 4.21 XRD patterns of (a) glass substrate and Up-HCM0.2 prepared with various mole ratio of TBA/HCM0.2 of (b) 0.0, (c) 0.1, (d) 0.5, (e) 1.0, (f) 2.0 and (g) 3.5.
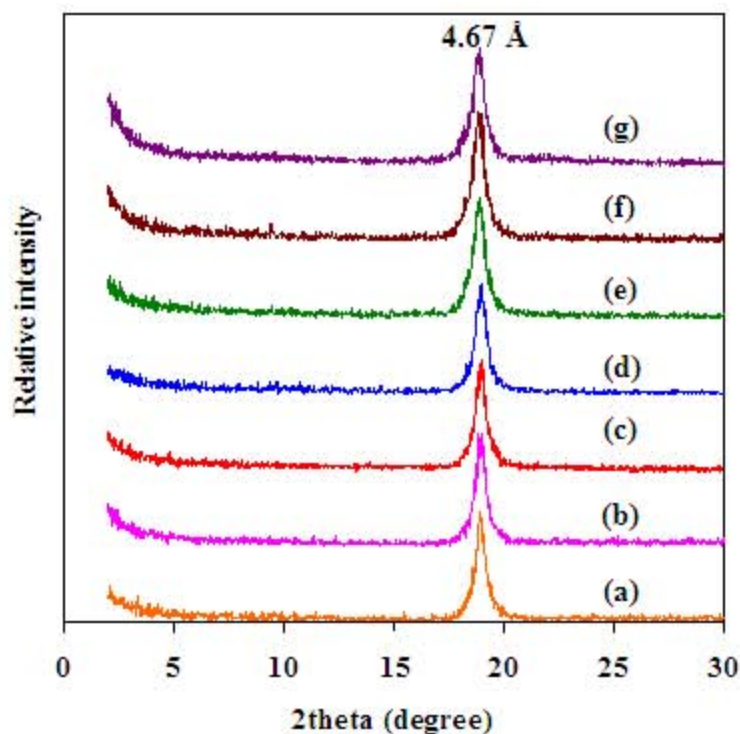
Figure 4.22 XRD patterns of Dep-HCM0.2 prepared with various mole ratio of TBA/HCM0.2 of (a) 0, (b) 0.1, (c) 0.5, (d) 1, (e) 2, (f) 3.5 and (g) 5.

4.4.7 Effect of sonication time

The effect of sonication time in exfoliation process was studied in the range of 1 - 90 min. The suspensions were prepared by shaking the HCM0.2 (0.20 g) in 50 mL TBAOH solution with TBA/HCM0.2 = 1.0 for 24 h and then sonicated with 125 w.

4.4.7.1 UV-Vis spectroscopy

Figure 4.23 (a) shows the spectra of HCM0.2 suspensions with various sonication times. The absorbance in the spectra increases when the sonication time increases. The plot of an absorbance at 244 nm versus sonication time is shown in Figure 4.23 (b). The absorbance increases dramatically upon sonication, and almost reaches the saturation at sonication time of 30 minutes of the colloids using sonication.
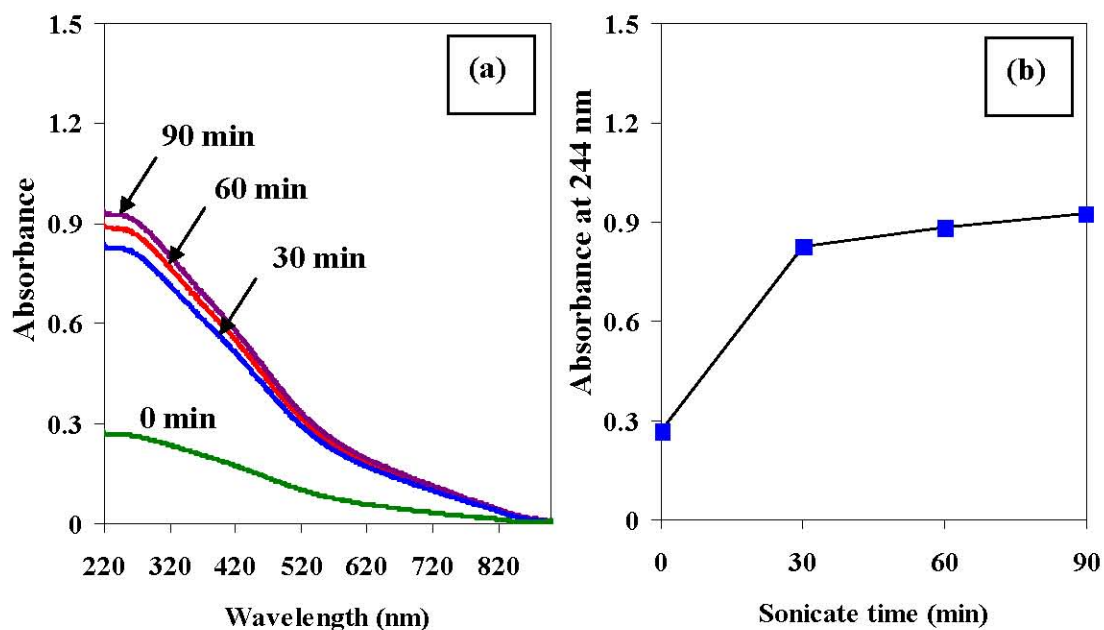
Figure 4.23 (a) The UV-Vis spectra of Up-HCM0.2 (diluted by 50-fold with Milli-Q water) with a mole ratio of TBA/HCM0.2 = 1 with various sonication times in the range 0 - 90 min and (b) the relationship between an absorbance at 244 nm and sonication time.

4.4.7.2 X-ray diffraction (XRD)

The XRD patterns of Up-HCM0.2 and Dep-HCM0.2 using various sonication times were recorded by casting the samples on a glass slide and drying at room temperature as shown in Figure 4.24 and Figure 4.25, respectively. Figures 4.24, the XRD patterns of all sample presents the small peak of HCM0.2 with a d-spacing about 4.67 Å. Furthermore, the broad peak with a d-spacing about 11.50 Å assigned to a TBA$^+$ intercalated phase is observed. Considering the patterns of Dep-HCM0.2 (Figure 4.26), all patterns are similar to the pattern of HCM0.2, as discussed in section 4.4.6.2. The crystallite sizes of deposited solid are indicated in Table 4.9. All the sonicated samples show a small crystallite size about 17 nm. This result is similar to the crystallite size of HCM0.2 precursor. Therefore, ultrasound in these conditions does not affect on the crystallite size but it assists the dispersion of solid in colloidal suspension.
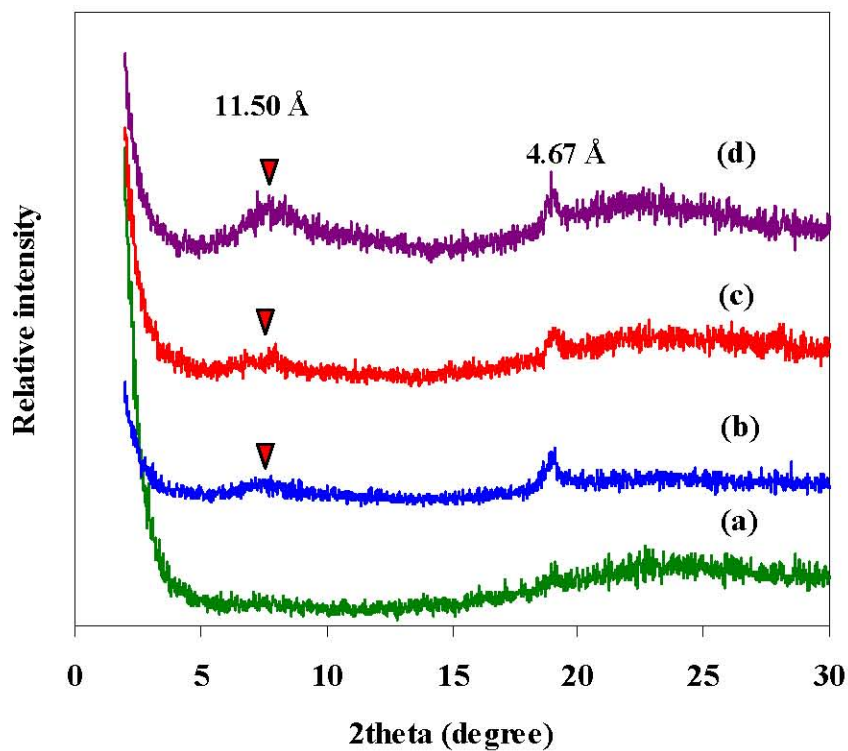
Figure 4.24 XRD patterns of Up-HCM0.2 with various sonication times at (a) 0 min, (b) 30 min, (c) 60 min and (d) 90 min.
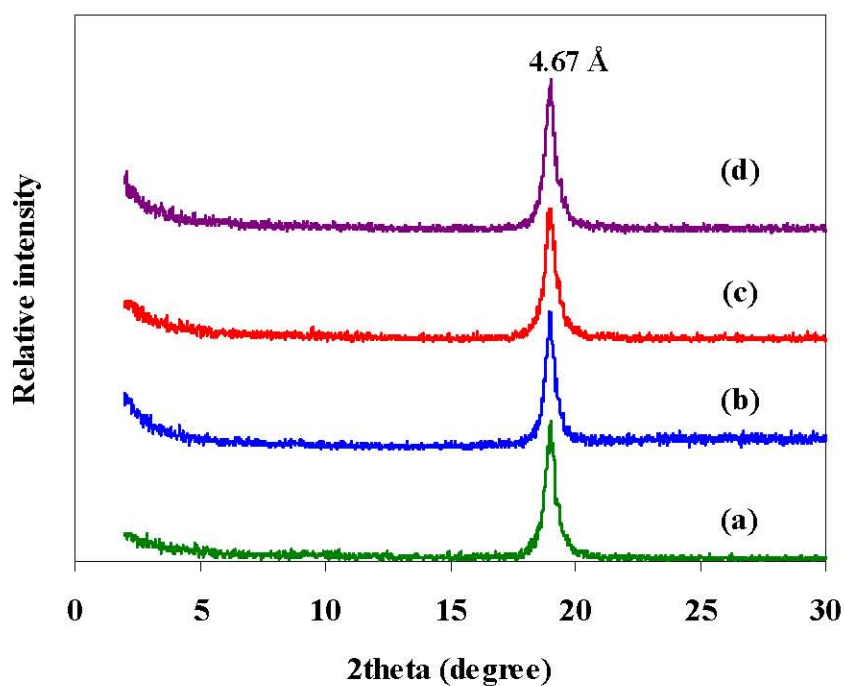
Figure 4.25 XRD patterns Dep-HCM0.2 using various sonication times at (a) 0 min, (b) 30 min, (c) 60 min and (d) 90 min.

Table 4.9 Crystallite sizes of HCM0.2 and Dep-HCM0.2 with various sonication times.

Sample	Crystallite size (nm)*
HCM0.2 starting material	18.6
Dep-HCM0.2, Sonicate for 0 min	17.8
Dep-HCM0.2, Sonicate for 30 min	19.2
Dep-HCM0.2, Sonicate for 60 min	16.3
Dep-HCM0.2, Sonicate for 90 min	18.3

* The data were calculated, based on the Scherer method by the MDI Jade software.

4.4.8 Preparation of colloidal suspensions of single-phased $LiCo_{1-x}Mn_xO_2$ calcined at 400 °C for 6 h

From the results above, the HCMx sheets in colloids were not fully exfoliated but much more dispersed after shaking with TBAOH solution. This result may cause from the large crystallite sizes, the high charged layers, the nature of the samples *etc*. In the next experiment, the single-phased $LiCo_{1-x}Mn_xO_2$ (x = 0.0 - 0.2) calcined at 400 °C for 6 h (LCMx-400) was chosen as the starting materials for study of the effect of reduced crystallite size in exfoliation process. The proton-exchanged materials (HCMx-400) were prepared by stirring LCMx-400 powders in 0.35 M H_2SO_4 for 24 h. The colloidal suspensions of HCMx-400 were obtained by disperse 0.20 g of HCMx-400 in 50 mL 0.04 M TBAOH solution (TBA/HCMx-400 = 1). The dispersion condition was shaking at 300 rpm for 24 h and sonicating for 30 min. After sonication, the suspension was centrifuged at 3000 rpm for 10 min to remove the deposited phases. The percentage of HCMx-400 in colloidal suspension phase can be estimated by subtracting the mass of the solid that remained at the bottom of the glass bottle from the initial mass (0.20 g). Thus, the calculated amounts of the solid oxides in dispersion phase of HCM0.0-400, HCM0.1-400 and HCM0.2-400 are about 19, 33 and 42 wt%, respectively.

4.4.8.1 UV-Vis spectroscopy

Figure 4.26 shows UV-Vis spectra of the prepared colloidal suspension of HCMx-400 (Up-HCMx-400). The spectra of Up-HCM0.0-400 exhibit optical absorption with a broad peak centered on 295 nm. The broad peak is ascribed to the combination of a characteristic absorption peak of the exfoliated HCM0.0-400 and the scattering from its larger particles in suspension Up-HCM0.0-400. In contrast, the Up-HCM0.1-400 and Up-HCM0.2-400 show narrower absorbance features with peak centered on 256 nm. These absorbance peaks may be attributed to the characteristic absorption of Mn-doping cobalt oxide nanosheets. The peak of Up-HCM0.2-400 with the highest absorbance could be explained as HCM0.2-400 was dispersed in higher amount than the other two oxides, as discussed in section 4.4.3.
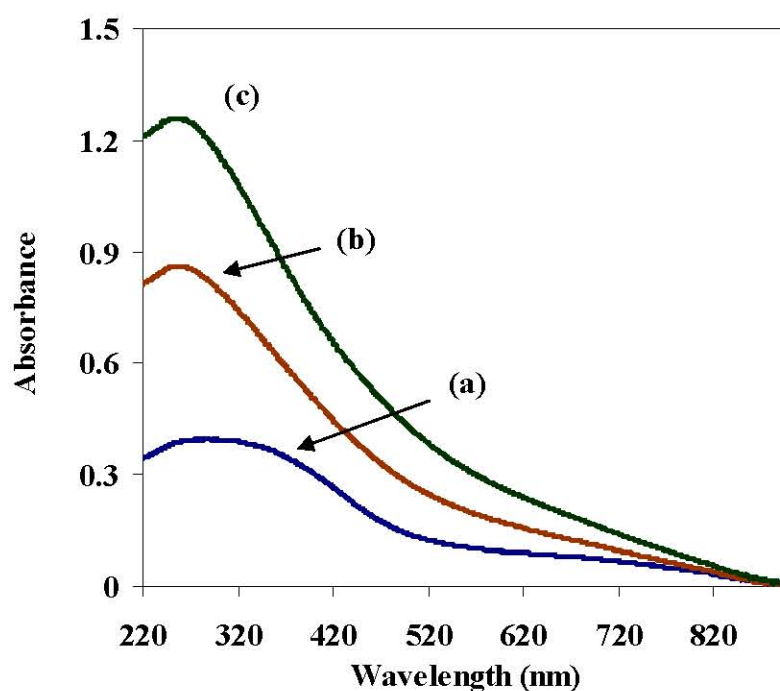
Figure 4.26 UV-Vis spectra of (a) Up-HCM0.0-400, (b) Up-HCM0.1-400 and (c) Up-HCM0.2-400 (diluted by 50-fold with Milli-Q water).

4.4.8.2 X-ray diffraction (XRD)

The upper phase (Up-HCMx-400) and deposited phase (Dep-HCMx-400) were cast on glass substrates and dried in air for 24 h as shown in Figures 4.27 and Figures 4.28, respectively. Figures 4.27, the XRD patterns of all sample

presents the peak of HCMx-400 with a d-spacing about 4.65 Å indicated that the exfoliation process is not fully complete. Furthermore, the broad peak with a d-spacing about 11.55 Å assigned to a TBA^+ intercalated phase is observed. Considering the patterns of Dep-HCMx-400 (Figure 4.28), all patterns are similar to the pattern of HCM0.2, as discussed in section 4.4.1.
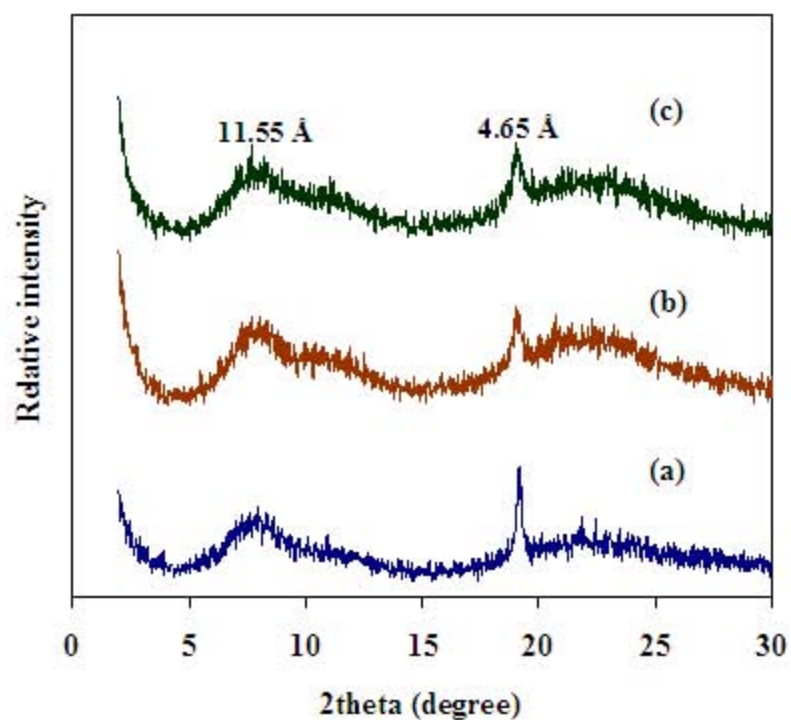
Figure 4.27 XRD patterns (a) Up-HCM0.0-400, (b) Up-HCM0.1-400 and (c) Up-HCM0.2-400.
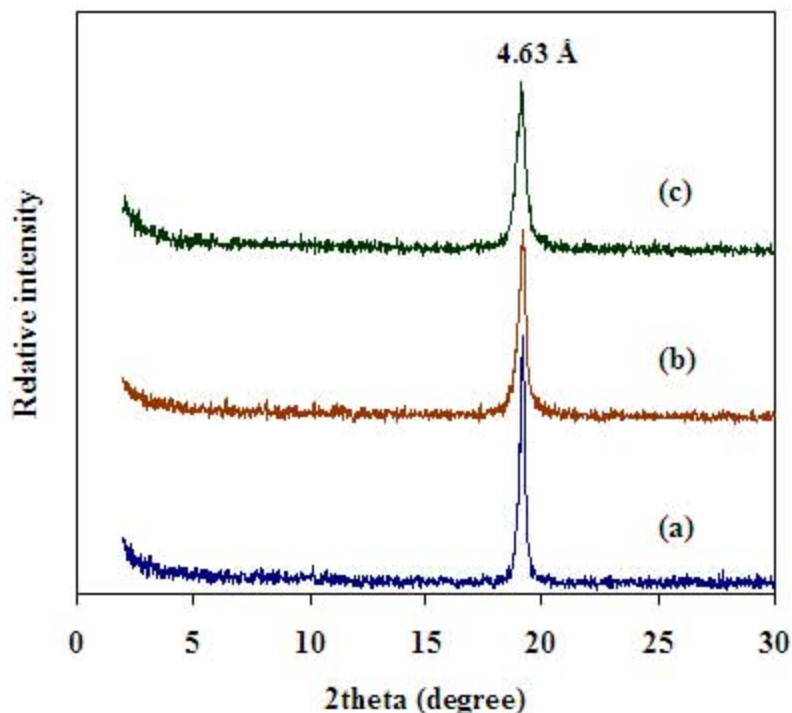
Figure 4.28 XRD patterns (a) Dep-HCM0.0-400, (b) Dep-HCM0.1-400 and (c) Dep-HCM0.2-400.

4.5 Fabrication of multilayer thin films

4.5.1 Effect of NaCl concentration

The thin films were prepared by dipping the substrates in PDAD solution containing various NaCl concentrations in the range of 0.00 - 1.00 M and then immersed in Up-HCM0.2. By naked-eyes observation before UV-Vis analyzing, the surface of NaCl-dipped film was smoother and more covered by HCM0.2 than NaCl-free film. This effect indicates to the increase of the ionic strength in the PDAD solution (polyelectrolyte), when the amount of NaCl increased. The effect could be explained in the same way as Claesson et al. [100] whom reviewed the interaction between polyelectrolytes and substrate surfaces. As the salt concentration was increased, the ionic strength of the solution has the effect of screening electrostatic interactions in the system resulting in: i) more coiled polyelectrolyte solution conformations due to screening of intrachain repulsion; ii) reduction in the number of directly surface bound segments and increased length and fraction of loops and tails

of the adsorbed polyelectrolyte. To explain the result above, the higher amount and better distribution of adsorbed layer polyelectrolyte PDAD cations, as the NaCl content increases, allows the negatively charged layers of HCM0.2 deposited in higher content and more homogeneously. Previous work on the investigation of the construction of poly(vinyl sulfate)/poly(allylamine hydrochloride) (PVS/PAH) film using NaCl solutions of different ionic strengths was reported by Lvov *et al.* [101]. As the NaCl concentration increases, thickness and surface roughness of PVS/PAH layers are increased.

Figure 4.29 (a) shows the UV-Vis spectra of PDAD/HCM0.2 films, prepared with various NaCl concentrations. The plot of absorbance at 211 nm versus concentration of NaCl is shown in Figure 4.29 (b). The absorbance in the spectra increases when the NaCl concentration increases up until NaCl concentration is 0.5. At NaCl concentration are 0.75 and 1.0, the absorbance does not increase due to the saturation of HCM0.2 adsorption on the surface.
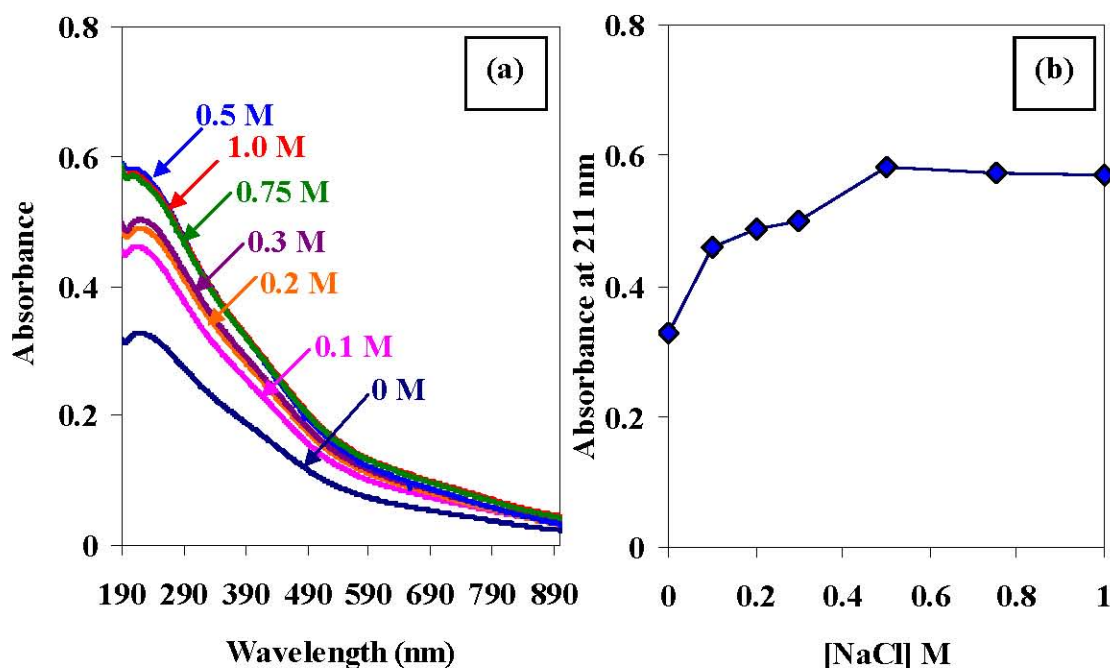
Figure 4.29 (a) UV-Vis spectra of PDAD/HCM0.2 thin films, prepared with various NaCl concentrations in polymer solution, and (b) the relationship between an absorbance at 211 nm (λ_{max}) and the concentration of NaCl.

4.5.2 Effect of dipping time

Figure 4.30 (a) shows the UV-Vis spectra of the PDAD/HCM0.2 films. Thin films were prepared by fixing the dipping time of the PDAD solution containing 0.50 M NaCl at 10 min and varying the dipping times of Up-HCM0.2 in the range of 1- 60 min. The plot of absorbance at 211 nm versus dipping time of Up-HCM0.2 is shown in Figure 4.31 (b). With increasing the dipping time, the absorbance is increased until the dipping time reaches 10 min, resulting from the saturation of HCM0.2 adsorption on the substrate surface.
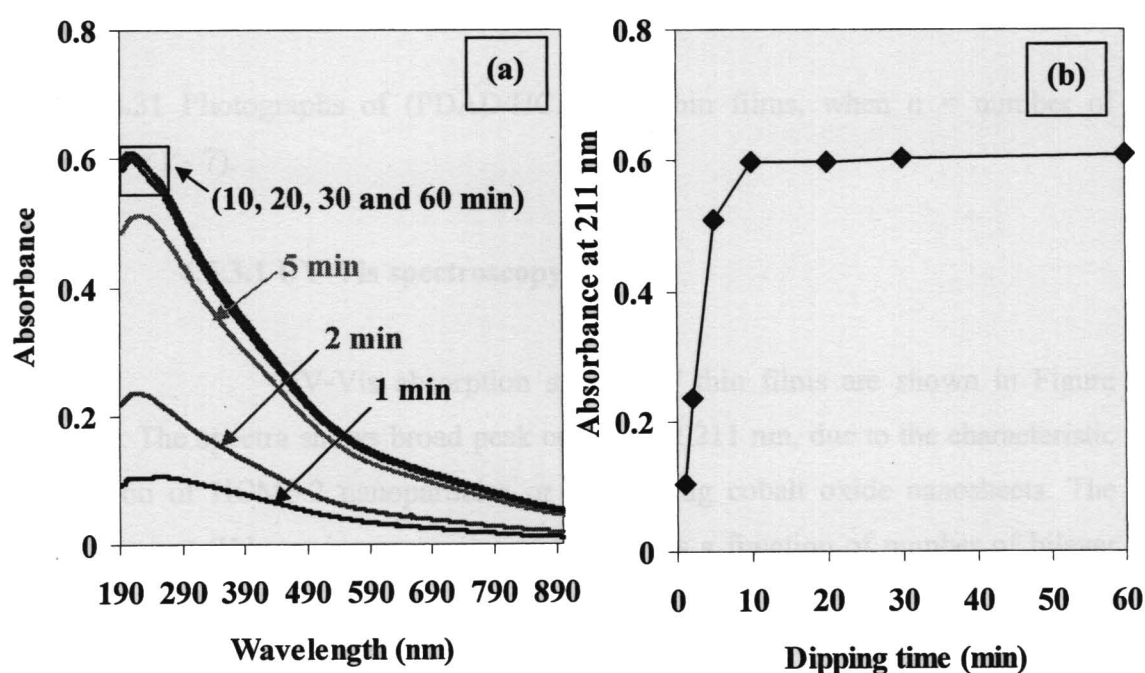
Figure 4.30 UV-Vis spectra of PDAD/HCM0.2 thin films with various dipping times of Up-HCM0.2 between 1 - 60 min, and (b) the relationship between an absorbance at 211 nm (λ_{max}) and the dipping times.

4.5.3 Preparation and characterization of the films

From the results above, the suitable condition for thin film preparation is by dipping the clean substrate in 10 mM PDAD containing 0.5 M NaCl for 10 min, followed by thorough washing with pure water, and then dipping in Up-HCM0.2 for 10 min, and washed again. After that, the resulting films were dried at room temperature. As shown in Figure 4.31, the thin films shows light-brown to deep-

brown color with the increase of number of bilayer, therefore the preparation method supports the consecutive growth of the films.

Figure 4.31 Photographs of (PDAD/HCM0.2)$_n$ thin films, when n = number of bilayer (n = 1 - 7).

4.5.3.1 UV-Vis spectroscopy

UV-Vis absorption spectra of thin films are shown in Figure 4.32 (a). The spectra shows broad peak centered at 211 nm, due to the characteristic absorption of HCM0.2 nanoparticles or Mn-doping cobalt oxide nanosheets. The absorbance at 211 nm increases almost linearly as a function of number of bilayer (Figure 4.32 (b)), indicating the successful layer-by-layer growth.
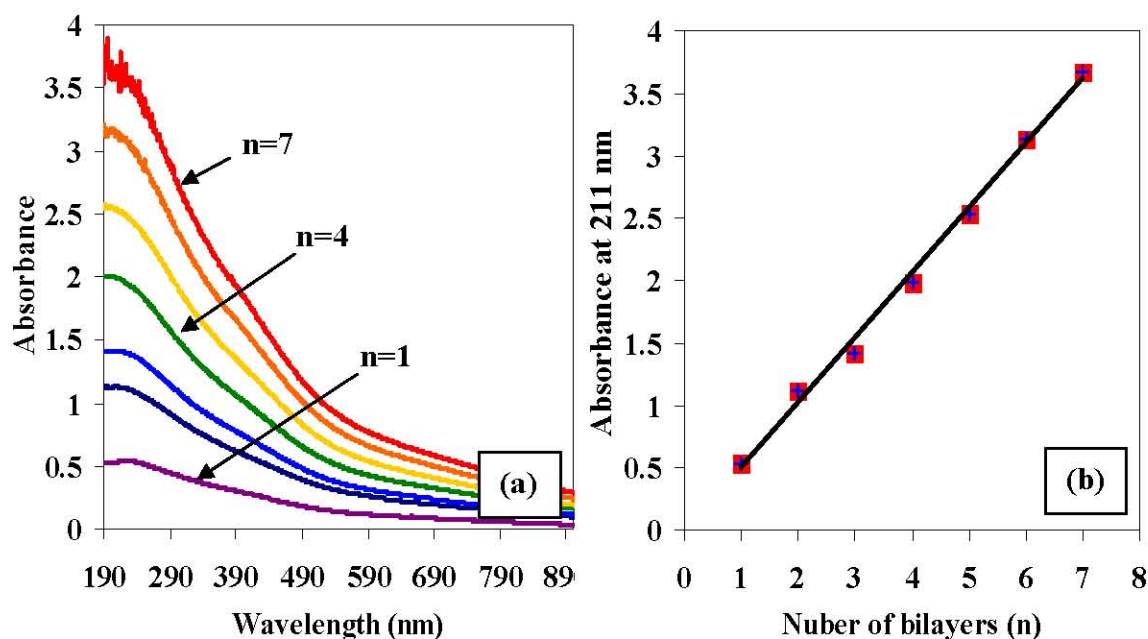
Figure 4.32 (a) UV-Vis spectra of multilayer thin films $(PDAD/HCM0.2)_n$: n = 1 - 7, and (b) the relationship between the absorbance at 211 nm and a number of bilayers.

4.5.3.2 X-ray diffraction (XRD)

Figure 4.33 (a) shows the XRD patterns of multilayer thin films $(PDAD/HCM0.2)_n$. The weak and board XRD peaks at a d-spacing of 4.67 Å indicates the nature of nanocrstallline $MCoO_2$, where M = interlayered cation. For thin films of 1 and 3 bilayer, the peak is not observed because the very thin metal oxide layer on the substrate is lower than the detection limit of XRD. However, the intensity of (003) peak increases and gets sharper as more layers are deposited onto the substrate, since the repeating pair of PDAD/HCM0.2. Figure 4.33 (b) shows the linear relationship between the area of (003) peak and (1/n); n = number of bilayers. As the number of bilayers increases, the area of these peaks increases exponentially, suggesting that XRD could be used to study the growth of nanostructure films.
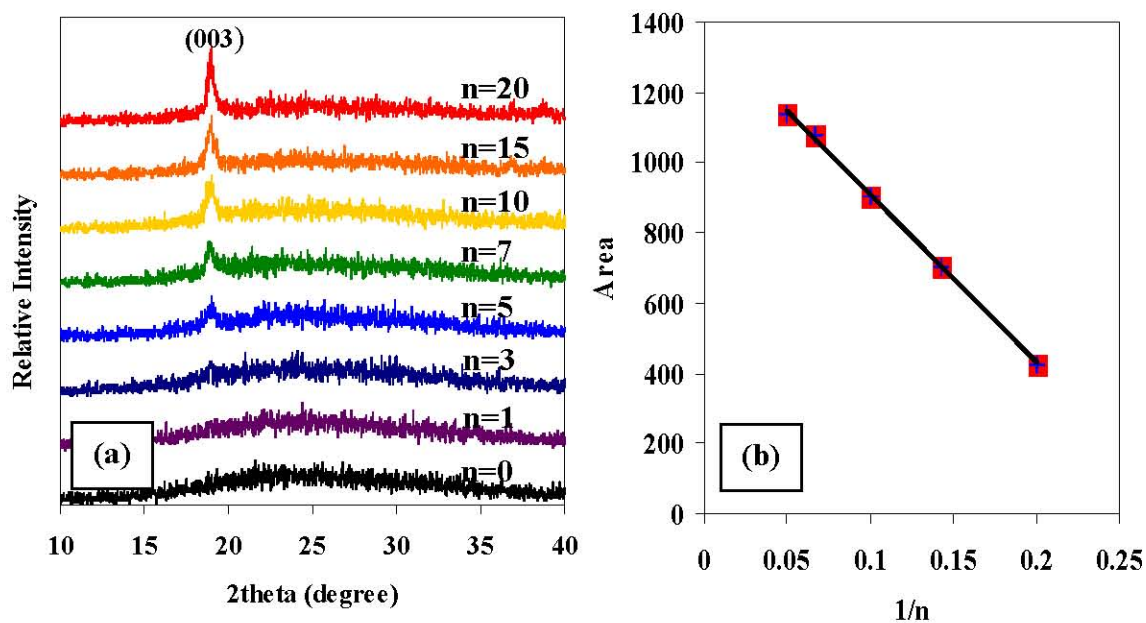
Figure 4.33 (a) XRD patterns of thin film $(PDAD/HCM0.2)_n$ with various n number of bilayer and (b) the relationship between the area and $1/n$.

4.5.3.3 Atomic force microscopy (AFM)

Figure 4.34 shows the tapping-mode two and three-dimensional (2-D and 3-D) AFM images of the multilayer thin films $(PDAD/HCM0.2)_n$ (n=1-15) on a glass substrate. AFM images shows that the HCM0.2 nanoparticles have diameters in the range of 30 - 60 nm. The surface of glass substrate was densely covered and the large aggregated HCM0.2 nanoparticles are found on some parts. The aggregation of the nanoparticles may cause from the incompleted exfoliation of HCM0.2 in the colloidal suspension. This effect may cause the higher roughness of thin film surface as the number of bilayer increases.
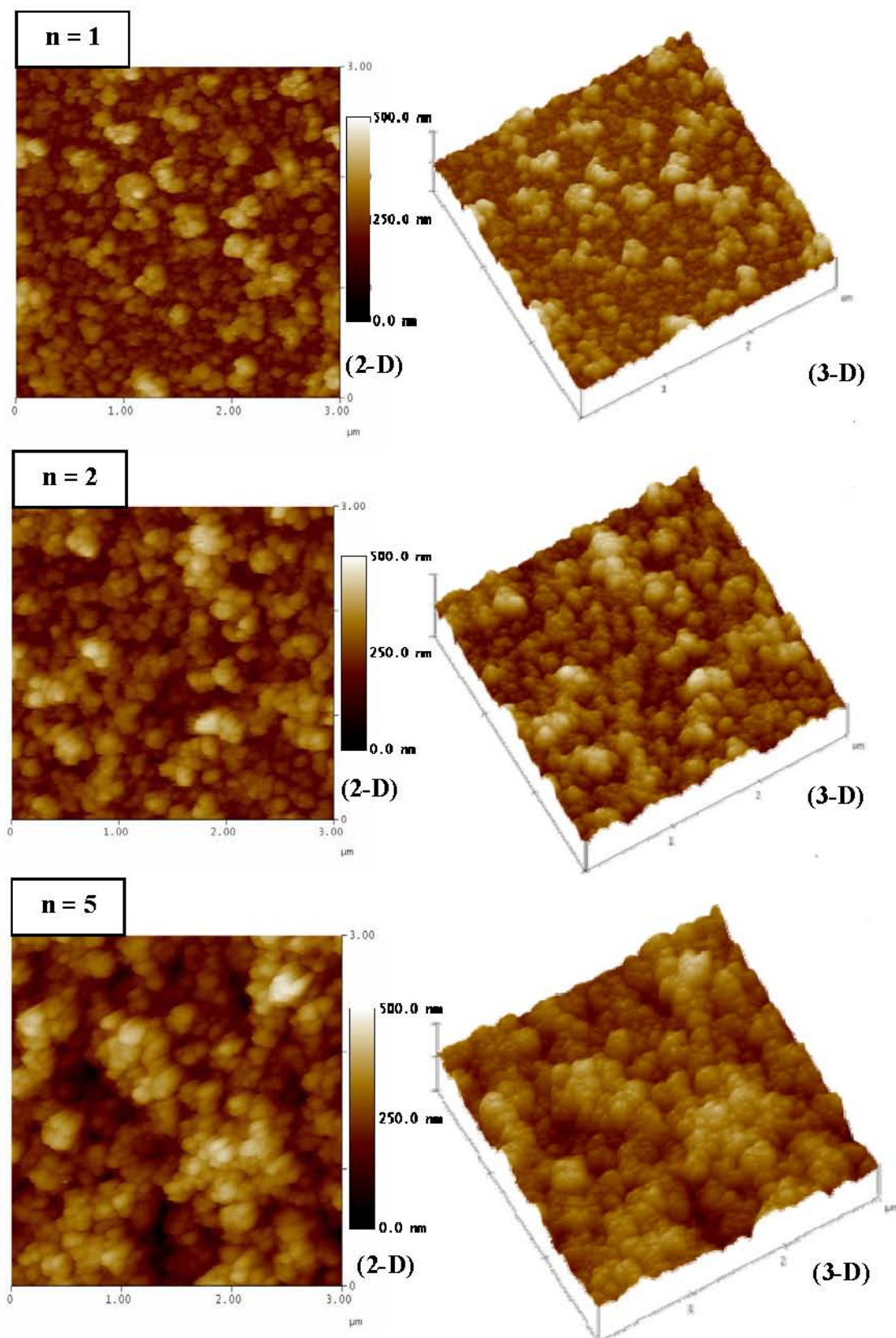
Figure 4.34 Tapping-mode 2-D and 3-D AFM images of (PDAD/HCM0.2)$_n$ films on a glass substrate.
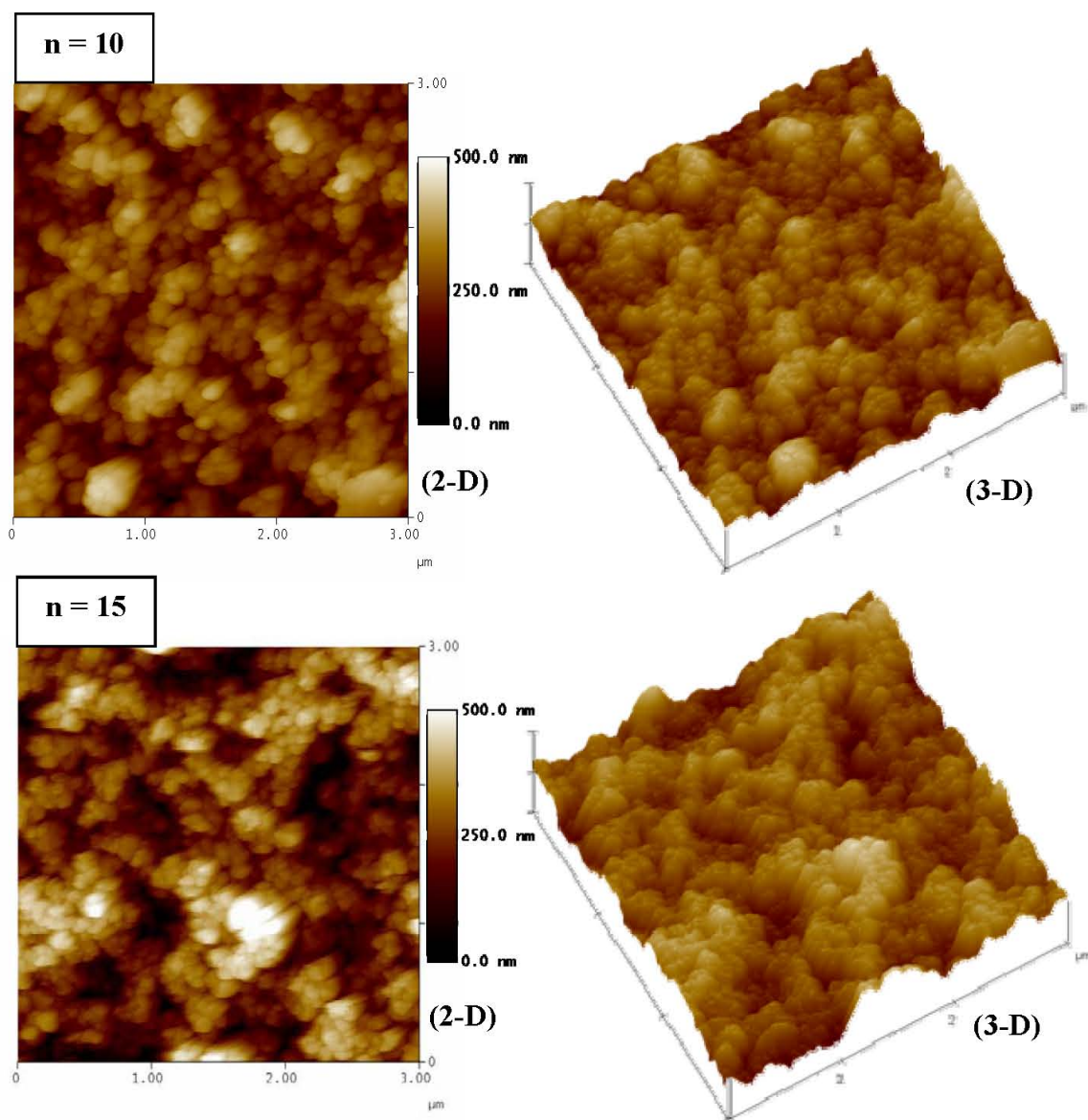
Figure 4.34 (Continue) Tapping-mode 2-D and 3-D AFM images of (PDAD/HCM0.2)$_n$ films on a glass substrate.

Figure 4.35 (a) shows the cross-sectional analysis of the thin films. For the PDAD/HCM0.2 film (n=1), a section analysis revealed the film have an average thickness about 98 nm. These average thicknesses increased linearly as a function of a number of bilayer (Figure 4.36(b)), indicating the success of the layer-by-layer growth.
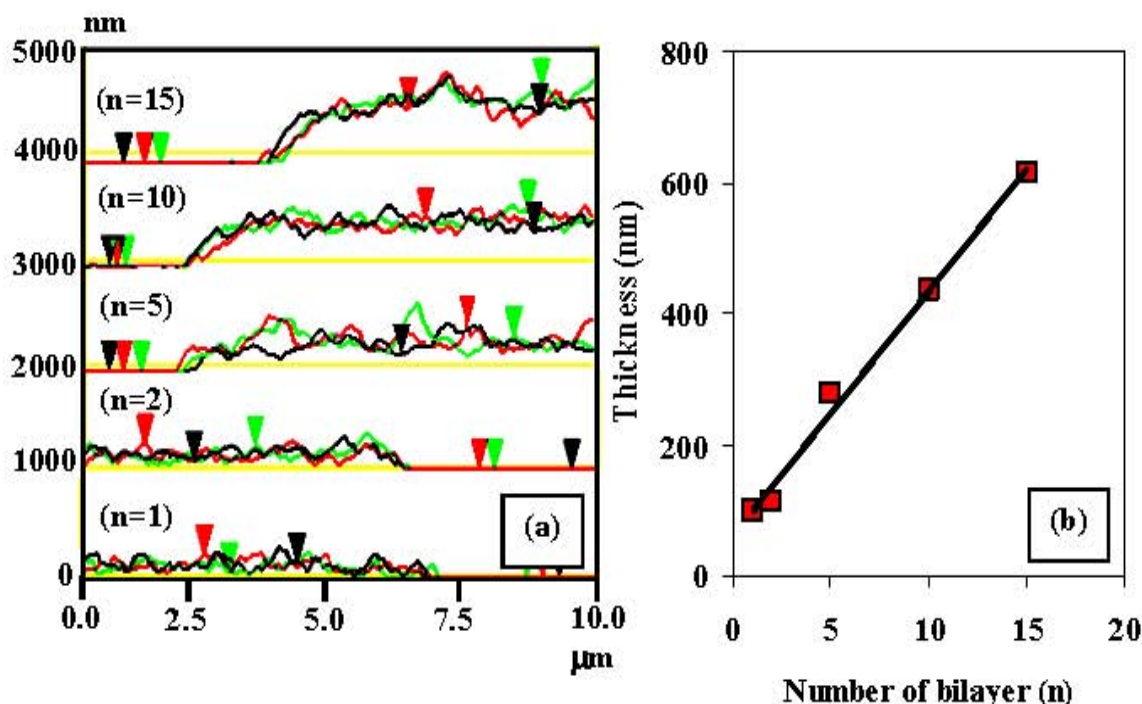
Figure 4.35 (a) A cross-sectional analysis revealed the roughness in the films. (b) Relationship between average thickness of multilayer films $(PDAD/HCM0.2)_n$ and number of bilayers (n).

4.5.3.4 Fourier transform infrared spectrometer (FT-IR)

The presence of PDAD in the multilayer thin films was confirmed by FT-IR. The FT-IR spectra of HCM0.2 and multilayer films $(PDAD/HCM0.2)_{10}$ are shown in Figure 4.36. The spectra of the films present characteristic absorption peaks due to existing organic and inorganic components. The HCM0.2 has a strong peak at 571 cm^{-1}, with a shoulder at 665 cm^{-1}. These absorption bands are attributed to the asymmetry stretching mode of CoO_6 and MnO_6 [90-91]. The bands at $2957, 2923,$ and 2855 cm^{-1} are assigned to the stretching vibrations of CH_3- and $-CH_2-$ groups of PDAD. The bands at 1459 and 1384 cm^{-1} are assigned to the bending and deformation modes $-CH_2-$ groups. Furthermore, the spectra presents a broad band around 3432 cm^{-1} (stretching) and 1630 cm^{-1} (bending) of the H_2O [31, 103].
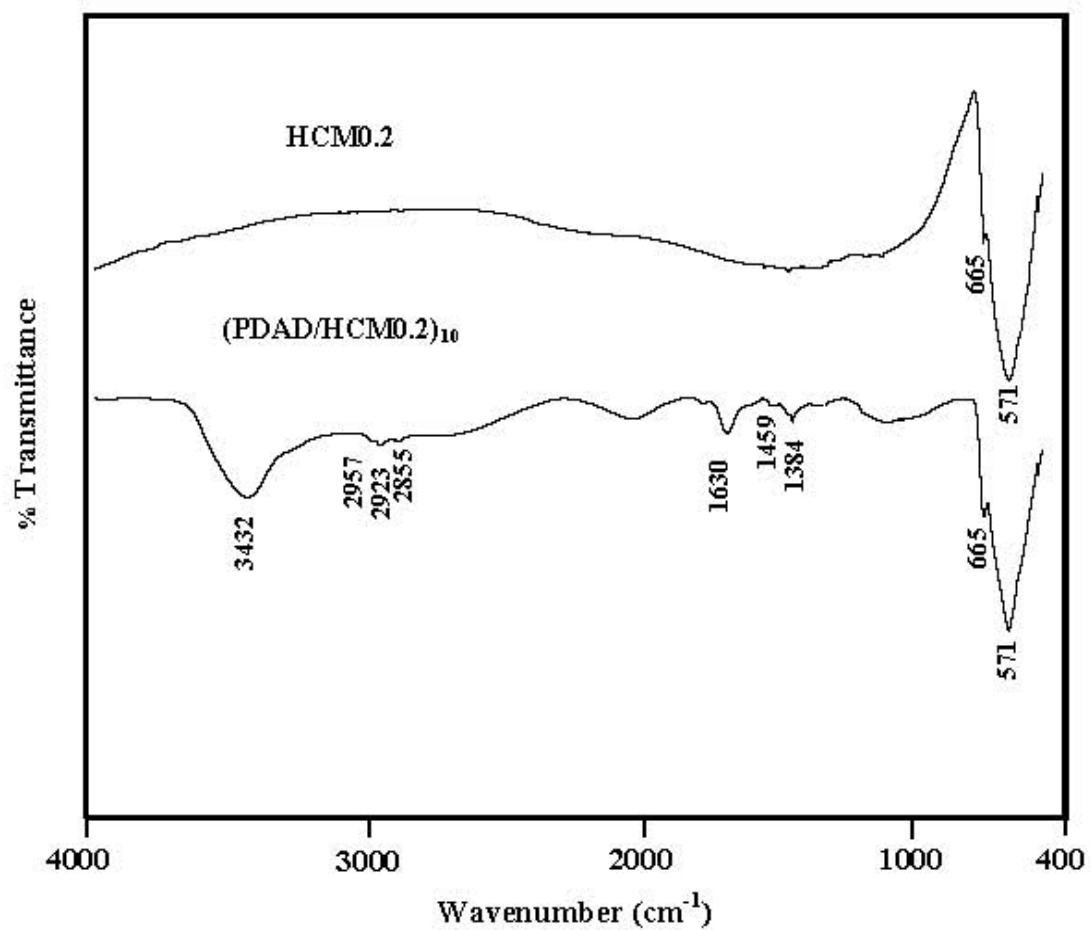
Figure 4.36 FT-IR spectra of (a) HCM0.2 and (b) (PDAD/HCM0.2)$_{10}$ films.

CHAPTER V

CONCLUSION AND SUGGESTION

5.1 Conclusion

$LiCo_{1-x}Mn_xO_2$ (x = 0.0 - 1.0), abbreviated as LCMx (x = the molar ratio of Mn-doping), were synthesized by sol-gel method with a citric acid as a chelating agent. The as-synthesized oxides were calcined at 300 – 700 ^{o}C for 6 h to obtain the fine powders needed to prepare the colloids.

The single-phased LCMx, with the rhombohedral structure, was observed for Mn-doping up to x = 0.2, calcined at 700 ^{o}C for 6 h, (LCM0.0, LCM0.1 and LCM0.2). Substitution of Co by Mn was found to result in the expansion of unit cell parameters, consistent with the larger size of Mn^{3+} than that of Co^{3+}. The particles sizes of LCM0.0, LCM0.1 and LCM0.2, observed by TEM, have diameters in the range of 50 -100 nm, 40 - 60 nm and 25 - 50 nm, respectively. The Mn-doping apparently leads to the reduction of particle size. XRD studies revealed the decreasing of crystallite size with Mn-doping as well.

The single-phased LCMx was used as a starting material for the preparation of colloids and multilayer thin films. The proton-exchanged materials, $HCo_{1-x}Mn_xO_2$ (HCMx) were prepared by stirring LCMx powders in 0.35 M H_2SO_4 for 24 h. The colloidal suspensions of HCMx were obtained by dispersion in tetrabutylammonium hydroxide (TBAOH) at various mole ratio of TBA/HCMx of 0.0 – 5.0 with the help of ultrasound at various sonication time of 0 – 90 minutes.

The optimum condition was observed at the mole ratio of TBA/HCMx = 1.0 and the setting of ultrasonic processor at 125 W for 30 minutes. The stable colloids were observed for HCM0.1 and HCM0.2. The degrees of stable colloid are 11 wt.% and 29 wt.% for HCM0.1 and HCM0.2, respectively. However, TEM images and XRD studies indicated that the colloidal suspensions of HCM0.1 and HCM0.2 were not fully exfoliated. The colloids were comprised of HCMx nanoparticles and

exfoliated Mn-doping cobalt oxide nanosheets. TEM images were observed that the Mn-doping cobalt oxides nanosheets have thickness about 5-10 nm. Colloidal suspension of HCM0.2 was further used as the starting precursor for the thin film preparation because its colloidal dispersion has higher solid content than of HCM0.1 has.

Multilayer thin films, poly(diallyldimethylammonium) (PDAD) ions and HCM0.2 nanoparticles has been successfully deposited layer-by-layer (LBL) onto the glass substrates by dipping coat technique. The optimum condition for thin film preparation was using 10 mM PDAD solution containing 0.5 M NaCl, dipping time at 10 min.

The photographs of thin films (PDAD/HCM0.2)$_n$; n = number of bilayers were exhibited light-brown to deep-brown color with increasing number of bilayers. FT-IR spectrum was indicated the LBL formation of organic-inorganic nanocomposite films. UV-Vis, XRD and AFM analyses were supported the consecutive growth of the films. The average thickness of a bilayer is 98 nm.

5.2 Suggestion for further work

From the obtained results, further work shall be focused on the following:

1. To study the conductivity of the (PDAD/HCM0.2)$_n$ films in order to prepare electrode materials.

2. To apply the thin films as a solid electrode and test their electrochemical properties.

REFERENCES

[1]   Kweon, H.J.; Kim, G.B.; Lim, H.S.; Nam, S.S.; Park, D.G. Synthesis of $Li_xNi_{0.85}Co_{0.15}O_2$ by the PVA-precursor method and charge-discharge characteristics of a lithium ion battery using this materials cathode. J. Power Sources. 83 (1999): 84-92.

[2]   The high-power lithium-ion (online). Avaliable from:

        http://www.superbpower.net/Battery/en8.html[2009, February 23]

[3]   Liu, Y.J.; Hu, Q.Y.;Li X.H.; Wang Z.X.; Guo H.J. Recycle and synthesis of $LiCoO_2$ from incisors bound of Li-ion batteries. Trans. Nonferrous Met. SOC. China. 16 (2006): 956-959.

[4]   Battery statistics (online). Avaliable from: http//warehouse-operation-manage ment.blogspot.com/2008/01/battery-statistics.html[2009, March 3]

[5]   Periasamy, P.; Kim, H.S.; Na, S.H.; Moon, S.I.; Lee, J.C. Synthesis and characterization of $LiNi_{0.8}Co_{0.2}O_2$ prepared by a combustion solution method for lithium batteries. J. Power Sources. 132 (2004): 213-218.

[6]   Hanh, M.D.; Thang, V.X B.; Hang, T.; Tai, L.T.; Hein, T.D.; Minh, N.D. (2005). Magnetic and electrochemical properties of nano-size $LiCoO_2$ powder prepared by sol-gel method. Proceedings of the Eighth German-Vietnamese Seminar on Physics and Engineering 4: 03-08.

[7]   Whittingham, M.S. Lithium batteries and cathode materials. Chem. Rev. 104 (2004): 4271-4301.

[8]   Gopukumar, S.; Jeong, Y.; Kim, K.B. Synthesis and electrochemical performance of tetravalent doped $LiCoO_2$ in lithium rechargeable cells. Solid State Ionics. 159 (2003): 223-232.

[9]   Ganesan, M.; Sundararajan, S.; Dhananjeyan, M.V.T. Sarangapani, K.B. Renganathan N.G. Synthesis and characterization of tetravalent titanium (Ti^{4+}) substituted $LiCoO_2$ for lithium-ion batteries. Mater. Sci. Eng. B 131 (2006): 203–209.

[10]   Sun, Y.K. Synthesis of ultrafine $LiCoO_2$ powders by sol-gel method. J. Mat. Sci. 31 (1996): 3617-3621.

[11] Ding, N.; Ge, X.W.; Chen, C.H. A new gel route to synthesize $LiCoO_2$ for lithium-ion batteries. <u>Mater. Res. Bull.</u> 40 (2005): 1451–1459.

[12] Santiago E.I.; Andrade A.V.C.; Paiva-Santos C.O.; Bulhoes L.O.S., Structure and electrochemical properties of $LiCoO_2$ prepared by combustion synthesis. <u>Solid State Ionics</u> 158 (2003): 91-102.

[13] Rodrigues S.; Munichandraiah N.; Shukla A.K., Novel solution-combustion synthesis of $LiCoO_2$ and its characterization as cathode material for lithium-ion cells, <u>J. Power Sources</u> 102 (2001): 322–325.

[14] Kalyani, P.; Kalaiselvi, N. Muniyandi, N. A new solution combustion route to synthesize $LiCoO_2$ and $LiMn_2O_4$. <u>J. Power Sources</u> 111(2002): 232-238.

[15] Chang S.K.; Kweon, H.J.; Kim, B.K.; Jung D.Y.; Kwon, Y.U. Syntheses of $LiCoO_2$ for cathode materials of secondary batteries from reflux reactions at 130-200°C. <u>J. Power Sources</u> 104 (2002): 125-131.

[16] Peng Z.S.; Wan C.R.; Jiang C.Y. Synthsis by sol-gel process and characterization of $LiCoO_2$ cathode materials. <u>J. Power Sources</u> 72 (1998): 215-220.

[17] Julien, C.; El-Farh, L.; Rangan, S.; Massot, M. Studies of $LiNi_{0.6}Co_{0.4}O_2$ cathode material prepared by the citric acid-assisted sol-gel method for lithium batteries. <u>J. Sol-Gel. Sci.Tech.</u> 15 (1999: 63–72.

[18] Jin, Y.; Lin, P.; Chen, C.H. Aninvestiaton of silicon-doped $LiCoO_2$ as cathode in lithium-ion secondary batteries. <u>Solid State Ionics</u> 177 (2006): 317-323.

[19] Khan, M.N.; Bashir, J. Synthesis and structural refinement of $LiAl_xCo_{1-x}O_2$ system. <u>Mater. Res. Bull.</u> 41 (2006): 1589–1595.

[20] Madhavi S.; Subba Rao, G.V.; Chowdari, B.V.R.; Li, S.F.Y. Effect of Cr dopant on the cathodic behavior of $LiCoO_2$. <u>Electrochim. Acta</u> 48 (2002): 219-226.

[21] Needham, S.A.; Wang, G.X.; Liu, H.K.; Drozd, V.A.; Liu, R.S. Synthesis and electrochemical performance of doped $LiCoO_2$ materials. <u>J. Power Sources</u> 174 (2007): 28–831.

[22]   Julien, C.; Camacho-Lopeza, M.A.; Mohanb, T.; Chitrab, S.; Kalyanib, P.; Gopukumar, S. Combustion synthesis and characterization of substituted lithium cobalt oxides in lithium batteries. Solid State Ionics 135 (2000): 241–248.

[23]   Kim, H.S.; Ko, T.K.; Na, B.K.; Cho, W.I.; Chao B.W. Electrochemical properties of $LiM_xCo_{1-x}O_2$ [M = Mg, Zr] prepared by sol–gel process J. Power Sources 138 (2004) 232–239.

[24]   Caballero, A.; Hernán, L.; Morales, J.; Rodr´ıguez Castellón, E. Santos, J. Enhancing the electrochemical properties of $LT\text{-}LiCoO_2$ in lithium cells by doping with Mn. J. Power Sources 128 (2004): 286-291.

[25]   Waki, S.; Dokko, K.; Itoh, Nishizawa, T.; Abe, M.; Uchida, T. I. High-Speed voltammetry of Mn-doped $LiCoO_2$ using a microelectrode technique. J. Solid State Electrochem. 4 (2000): 205-209.

[26]   Suresh, P. Rodrigues, S. Shukla, A.K. Vasan, H.N. Munichandraiah, N.Synthesis of $LiCo_{1-x}Mn_xO_2$ from a low-temperature route and characterization as cathode materials in Li-ion cells. Solid State Ionics 176 (2005): 281-290.

[27]   Chen, X. T.; Tu, J. P.; Yang, Y. Z.; Wu, H. M.; Xiang, J.Y. Effect of $LiCoO_2$ coating on the electrochemical performance of $LiMn_{0.9}Co_{0.1}O_2$ cathode materials for Li-ion batteries. Phys. Scr.T129 (2007): 49–52.

[28]   Sukpirom, N.; Lerner M. M. Preparation of oranic-inorganic nanocomposites with a layered titanate. Chem. Master. 13 (2001): 2179-2185.

[29]   Sukpirom, N.; Lerner M. M. Rapid syntheses of nanocomposites with layered tetratitanate using ultrasound. Mater. Sci. Eng. A354 (2003): 180-187.

[30]   Shiguihara A.L.; Bizeto M.A.; Constantino V.R.L. Exfoliation of layered hexaniobate in tetra(n-butly)ammonium hydroxide aqueous solution. Colloids and surfaces A: Physicochem. Eng. Aspect 295 (2007) 123-129.

[31]   Wang, L.; Omomo, Y.; Sakai, N.; Fukuda, K.; Nakai, I.; Ebina, Y.; Takada, K.; Watanabe, M.; Sasaki, T. Fabrication and characterization of multilayer ultrathin films of exfoliated MnO_2 nanosheet and polycations. Chem. Mater. 15 (2003): 2873-2878.

[32]   Zhang, X.; Wang, Y.; Chen, X.; Yang, W. Fabrication and characterization of a novel inorganic MnO_2/LDHs multilayer thin film via a layer-by-layer self-assembly method. Materials Letters 62 (2008):1613–1616.

[33]   Wang, L.; Sakai, N.; Ebina, Y.; Takada, K.; Sasaki, T. Inorganic multilayer films of manganese oxide nanosheets and aluminum polyoxocations: Fabrication, structure, and electrochemical behavior. Chem. Mater. 17 (2005): 1352-1357.

[34]   Z.S. Wang, T. Sasaki, M. Muramatsu, Y. Ebina, T. Tanaka, L. Wang, M. watanabe, Self-Assenbled multilayers of titania nanoparticles and nanosheet with polyelectrolytes. Chem. Mater. 15 (2003) 807.

[35]   Sasaki, T.; Ebina, Y.; Watanabe, M.; Decher, G. Multilayer ultrathin film of molecular titaia nanosheets showing highly effectent UV-light absorption. Chem. Commun. (2000): 2163-2164.

[36]   Kim, D. W.; Blumstein, A.; Tripathy, S. K. Nanocomposite films derived from exfoliated functional aluminosilicate through electrostatic layer-by-layer assembly. Chem. Mater. 13 (2001): 1916-1922.

[37]   Fang, M.; Kim, C.H.; Saupe, G.B.; Kim, H.N. Waraksa, C.C.; Miwa, T.; Fujishima, A.; Mallouk, T. E. Layer-by-layer growth and condensation reactions of niobate and titanoniobate thin films. Chem. Mater. 11 (1999):1526-1532.

[38]   Ollivier, P.J.; Kovtyukhova, N.I.; Keller, S.W.; Mallouk, T.E. Self-assembled thin films from lamellar metal disulfides and organic polymer. Chem. Commun. (1998): 1563-1564.

[39]   Yu, X.; Rajamani, R.; Stelson, K.A.; Cui, T. Fabrication of carbon nanotube based transparent conductive thin films using layer-by-layer technology. Surf. Coatings Technol. 202 (2008): 2002–2007.

[40]   Shin, Y.J.; Zhang, Q.; Hua, F. Time dependent conductive behavior of the layer-by-layer self-assembled SnO_2 nanoparticle thin film. Thin Solid Films 516 (2008):3167–3171.

[41]   Sukpirom, N.; Lerner M. M. Rapid exfoliation of a layered titanate by ultrasonic processing. Mater. Sci. Eng. A333 (2002): 218-222.

[42]   Sasaki, T.; Ebina, Y.; Tanaka, T.; Harada, M.; Watanabe, M. Layer-by-layer assembly of titania nanosheet/polycation composite films. Chem. Mater. 13 (2001): 4661-4667.

[43]   Abe, R.; Shinohara, K.; Tanaka, A.; Hara, M.; Kondo, J.N.; Domen, K., Preparation of thin film of a layer titanate by the exfoliation of $Cs_xTi_{(2-x/4)}\square_{x/4}O_4$. Chem.Mater. 10 (1998): 329-333.

[44]   Prasad, G.K.; Takei, T.; Arimoto, K.; Yonesaki, Y.; Kumada, N.; Kinomura, N. Nanocomposites based on exfoliated $NbWO_6$ nanosheets and ionic polyacetylenes. Solid State Ionics 177 (2006): 197-201.

[45]   Du, G.H.; Yu, Y.; Chen, Q.; Wang, R.H.; Zhou, W.; Peng, L.M. Exfoliating $KTiNbO_5$ particles into nanosheets. Chem. Phys. Lett. 377 (2003): 445–448.

[46]   Masuda, Y.; Hamada, Y.; Seo, W.S.; Koumoto, K. Exfoliation of layer in Na_xCoO_2. J. Nanosci. Nanotechnol. 6 (2006): 1632-1638.

[47]   Ramachandran, K.; Oriakhi, C.O.; Lerrner, M.M. Intercalation chemistry of cobalt and nickel dioxides: A facile route to new compounds containing organocations. Mater. Res. Bull. 31(1996): 767-772.

[48]   Clemencon, A.; Appapillai, A.T.; Kumar, Shao-Horn, S. Y. Atomic force microscopy studies of surface and dimensional changes in Li_xCoO_2 crystals during lithium de-intercalation. Electrochem. Acta. 52 (2007) 4572–4580.

[49]   Shao, H.; Croguennec, Y. L.; Delmas, C.; Nelson, C.; O'Keefe, M. A. Atomic resolution of lithium ions in $LiCoO_2$. Nature Materials 2 (2003): 464-467

[50]   Gabrisch, H.; Yazami, R.; Fultz, B. Electrochemical and the character of dislocations in $LiCoO_2$. Solid State Lett. 5-6 (2002): A111-A114.

[51]   Choi, S.H.; Kim, J.; Yoon, Y. S. Self-discharge analysis of $LiCoO_2$ for lithium batteries. J. Power Sources 138 (2004): 283–287.

[52]   Okubo, M.; Hosono, E.; Kim, J.; Enomoto, M.; Kojima, N.; Kudo, T.; Zhou, H.; Honma, I. Nanosize Effect on High-rate Li-ion intercalation in $LiCoO_2$ electrode. J. Am. Chem. Soc.129 (2007): 7444-7452.

[53]   Gupta, U.N.; Samuel, V.; Muthurajan, H.; Kumar, H.H.; Patil, S.D.; Ravi, V.
         A co-precipitation method for preparation of Bi_3TiNbO_9 powders.
         <u>Ceramics International</u> 34 (2008): 675–677.

[54]   Fonseca, C.P.; Pallone, E.M.J.A.; Neves, S. Electrochemical properties of
         $LiMn_2O_4$ films produced by combustion reaction. <u>Solid State Sci.</u> 6
         (2004): 1353–1358.

[55]   Fu, L.J.; Liu, H,; Li, C.; Wu, Y.P.; Rahm, E.; Holze, R.; Wu, H.Q. Electrode
         materials for lithium secondary batteries prepared by sol–gel methods.
         <u>Progr. Mater. Sci.</u> 50 (2005): 881–928.

[56]   Schoonheydt, R. A.; Vaia, T.P.; G. Lagaly,; Gangas, N. Pillared clays and
         pillared layered solids. <u>Pure Appl. Chem.</u> 71 (1999): 2367-2371.

[57]   Tagaya, H.; Takeshi, K.; Ant, K.; Kadokawa, J.; Karasu, M.; Chiba, K.
         Preparation of new orgaic-inorganic nanocomposite by intercalation of
         organic compounds into MoO_3 by ultrasound. <u>Mater. Res. Bull.</u> 30
         (1995): 1161-1171.

[58]   Nakano, S.; Sasaki, T.; Takemura, K.; Watanabe, M. Pressure-Induced
         Intercalation of Alcohol Molecules into a Layered Titanate. <u>Chem.
         Mater.</u> 10 (1998): 2044-204.

[59]   Lai, K.; Kong, A.; Yang, F.; Chen, B.; Ding, Shan, H.Y.; Huang, S.
         Intercalation of alkylviologen dications into the layered vanadium
         Pentoxide. <u>Inorg. Chim. Acta</u> 359 (2006): 1050–1054.

[60]   Ma, R.; Bando, Y.; Sasaki, T. Nanotubes of lepidocrocite titanates. <u>Chem.
         Phys. Lett.</u> 380 (2003): 577–582.

[61]   Wang, L.; Sasaki, T.; Ebina, Y.; Kurashima, K.; Watanabe, M. Fabrication of
         controllable ultrathin hollow shells by layer-by-layer assembly of
         exfoliated titania nanosheets on polymer templates. <u>Chem. Mater.</u> 14
         (2002): 4827-4832.

[62]   Ma, R.; Bando, Y.; Sasaki, T. Directly rolling nanosheets into nanotubes. <u>J.
         Phys. Chem. B</u> 108 (2004): 2115-2119

[63]   Wang, J.; Yin, S.; Sato, T. Characterization of $H_2Ti_4O_9$ with high specific
         surface area prepared by a delamination/reassembling process. <u>Mater
         Sci. Eng. B</u> 126 (2006): 53–58.

[64]   Liu, Z.H.; Yang, X.; Makita, Y.; Ooi, K. Preparation of a polycation-intercalated layered manganese oxide nanocomposite by a delamination/reassembling process. Chem. Mater. 14 (2002): 4800-4806.

[65]   Kim, K.Y.; Byun, K.T.; Kwak, H.Y. Temperature and pressure fields due to collapsing bubble under ultrasound. Chem. Eng. J. 132 (2007): 125–135.

[66]   Suslick, K.S.; Price, G.J. Applications of ultrasound to materials chemistry. Annu. Rev. Mater. Sci. 29 (1999): 295–326.

[67]   Kennedy, J.E. High-intensity focused ultrasound in the treatment of solid tumours. Nature Reviews Cancer 5 (2005): 321-327.

[68]   Kawaoka, H.; Hibino, M.; Zhou, H.; Honma, I. Sonochemical synthesis of amorphous manganese oxide coated on carbon and application to high power battery. J. Power Sources 125 (2004): 85–89.

[69]   Shaw, D. J. Introduction to colloid and surface chemistry. Gillingham: Butterworth &Co, 1980.

[70]   Everett, D.H. Basic priciples of colloid science. London: the Royal Society of Chemistry, 1988.

[71]   Omomo, Y.; Sasaki, T. Wang, l.; Watanabe, M. Redoxable nanosheet crystallites of MnO_2 derived via delamination of a layered manganese oxide. J. Am. Chem. Soc. 2003, 125 (2003): 3568-3575.

[72]   Liu, Z.; Ma, R.; Osada, M.; Iyi, N.; Ebina, Y.; Takada, K.; Sasaki, T. Synthesis, anion exchange, and delamination of Co−Al layered double hydroxide: assembly of the exfoliated nanosheet/polyanion composite films and magneto-optical studies. J. Am. Chem. Soc. 128 (2006): 4872-4880.

[73]   Wallard, H.H.; Merritt, L.L.; Dean, J.A. Instrumental methods of analysis. Canada: D.Van Nostand company, 1958.

[74]   Instruction Manual TN-100/T-100 Portable Turbidimeter (online). Avaliable from: http://www.4oakton.com/manuals/Turbidity/35635-00.pdf [2009, February 23]

[75]   Kim J.H.; Kim S. H.; Shiratori, S. Fabrication of nanoporous and hetero structure thin film via a layer-by-layer self assembly method for a gas sensor. Sensors & Actuators B 102 (2004): 241–247.

[76]   Zhanga, S.; Shena, J.; Fua, H.; Donga, W.; Zhenga, Z.; Shi L. Bi_2WO_6 photocatalytic films fabricated by layer-by-layer technique from Bi_2WO_6 nanoplates and its spectral selectivity. J. Solid State Chem. 180 (2007): 1456–1463.

[77]   Hua, F.; Lvov, Y. M. Layer-by-layer assembly. The New Frontiers of Organic and Composite Nanotechnol. (2008): 1-44.

[78]   Microscope (online). Available from: http://www1.stkc.go.th/stportal Document/stportal_1170654028.doc.[2009, February 12]

[79]   Choi, K.S. Band Gap Tuning of Zinc Oxide Films for Solar Energy Conversion (online). Available from: http://papadantonakis.com/ images /9/91/ Band_Gap_Module.pdf.[2009, March 14]

[80]   Nipaka Sukpirom, "Intercalation, Exfoliation, and nanocomposites of layered inorganic compounds," (Doctor disserttation, Department of Chemistry and Center for Advanced Materials Research, Oregon State University, 2001).

[81]   Omomo, Y.; Sasaki, T. Wang, 1.; Watanabe, M. Redoxable nanosheet crystallites of MnO_2 derived via delamination of a layered manganese oxide. J. Am. Chem. Soc. 2003, 125 (2003): 3568-3575.

[82]   Ko, M.J.; Plawsky, J. Surface Plasmon resonances of metal colloidal particles synthesisized by a photo-chemical process. J. Korean Chem. Soc. 43 (1999):1-7.

[83]   Bubert, H.; Jenett, H. Surface and thin film analysis. Weinheim, Wiley-VCH Verlag GmbH, 2002.

[84]   Atomic force microscope (online). Avaliable from: http://www.edinformatics .com/nanotechnology/atomic_force_microscope.htm.[2009, April 2]

[85]   Smith, A. Atomic force microscopy (online). Avaliable from: http://www.sgm.ac.uk/pubs/micro_today/pdf/smith.pdf.[2009, April 2]

[86]   General concept and defining characteristics of AFM (online). Avaliable from: http://ipc.iisc.ernet.in/~ipcafm/about%20us.html. [2009, April 2]

[87]   Gupta, R.; Manthiram, A. Chemical extraction of lithium from layered LiCoO$_2$. J. Solid State Chem. 121 (1996): 483-491.

[88]   Wu, M.; Rongqing, A.C.; Li, X.Y. Nanocrystalline LiNi$_{1-x}$Co$_x$O$_2$ cathode materials prepared by gel-combustion process. Mater. Sci. Eng. B99 (2003): 336-339.

[89]   Rao, K. J.; Benqlilou-Moudden, H.; Desbat, B.; Vinatier, P.; Levasseur, A. Infrared spectroscopic study of LiCoO$_2$ thin films. J. Solid State Chem. 165 (2002): 42–47.

[90]   Tao, S.; Wu, Q.; Zhan, Z.; Meng, G. Preparation of LiMO$_2$ (M=Co, Ni) cathode materials for intermediate temperature fuel cells by sol-gel processes. Solid State Ionics 124 (1999): 53–59.

[91]   Li, X.; Xu Y. Spinel LiMn$_2$O$_4$ active material with high capacity retention. Appl. Surf. Sci. 253 (2007): 8592–8596.

[92]   Amdouni, N.; Zarrouk, H.; Soulette, F.; Julien C. LiAl$_y$Co$_{1-y}$O$_2$ ($0.0 \leq y \leq 0.3$) intercalation compounds synthesized from the citrate precursors. Mater. Chem. Phys. 80 (2003): 205–214.

[93]   Stoyanova, R.; Zhecheva E.; Zarkova, L. Effect of the Mn-substitution for Co on the crystal structure and acid delithiation of LiMn$_y$Co$_{1-y}$O$_2$ solid solutions. Solid State Ionics 73 (1994): 233-240.

[94]   Stoyanova, R.; Zhecheva, E.; Bromiley, G.; Ballaran, T.B.; Alcantara, R.; Corredor, J.I.; Tiradoc, J.L. High-pressure synthesis of Ga-substituted LiCoO$_2$ with layered crystal structure. J. Mater. Chem. 12 (2002): 2501–2506.

[95]   Takagaki, A.; Sugisawa, M.; Lu, D.; Kondo, J.N.; Hara, Domen, M. K.; Hayashi,S. Exfoliated nanosheets as a new strong solid acid catalyst. J. Am. Chem. Soc. 125 (2003): 5479-5485.

[96]   Sasaki, T.; Watanabe, M.; Michiue, Y.; Komatsu, Y.; Izumi, F.; Takenouchi. S. Preparation and acid-base properties of a protonated titanate with the lepidocrocite-like layer structure. Chem. Mater. 7(1995): 1001-1007.

[97]   Kim, J.J.; Ryu, K.H.; Sakaue, K.;Terauchi, H.; Yo, C.H. Structural characterization for the chemically Li^{+} ion extracted Li_yCoO_2, $Li_yCo_{0.95} Ga_{0.05}O_2$, and $Li_yCo_{0.9}Ga_{0.1}O_2$ compounds. <u>J. Phy. Chem.</u> 63 (2002): 2037-2045.

[98]   Liu, Z.H.; Wang, Z.M.; Yang, X.; Ooi, K. Intercalation of organic ammonium ions into layered graphite oxide. <u>Langmuir</u> 18 (2002): 4926-4932.

[99]   Mercer, K.L.; Tobiason, J.E. Removal of arsenic from high ionic strength solutions: effects of ionic strength, pH, and preformed versus in situ formed HFO. <u>Environ. Sci. Technol.</u> 42 (2008): 3797-3802.

[100]   Lvov, Y.; Decher, G.; Moehwald, H. Assembly, structural characterization, and thermal behavior of layer-by-layer deposited ultrathin films of poly(vinyl sulfate) and poly(allylamine). <u>Langmuir</u> 9 (1993): 481-486.

[101]   Bizeto, M.A.; Constantino, V.R.L. Layered $H_2K_2Nb_6O_{17}$ exfoliation promoted by n-butylamine. <u>Mater. Res. Bull.</u> 39 (2004):1811–1820.

[102]   Claesson, P.M.; Poptoshev, E.; Blomberg, E.; Dedinaite, A. Polyelectrolyte-mediated surface interactions. <u>Adv. Colloid Interface Sci.</u> 114–115 (2005): 173-187.

[103]   Wang, Z.S.; Sasaki, Muramatsu, T. M.; Ebina, Y.; Tanaka, T.; Wang, L.; Watanabe, M. Self-assembled multilayers of titania nanoparticles and nanosheets with polyelectrolytes. <u>Chem. Mater</u> 15 (2003): 807- 812.

Appendices

1. The calculation of synthesis $LiCo_{1-x}Mn_xO_2$ by citric acid assisted sol gel method

Table A-1 Molecular weight of reactant for $LiCo_{1-x}Mn_xO_2$ synthesis

Chemicals	Molecular weight (Mw)
$LiNO_3$	68.94
$Co(NO_3)_2 6H_2O$	291.03
$Mn(NO_3)_2 4H_2O$	251.01
Citric acid	192.13
$LiCo_{0.8}Mn_{0.2}O_2$	97.07

Example Preparation of 0.010302 mole $LiCo_{0.8}Mn_{0.2}O_2$ (LCM0.2; 1g)

$LiNO_3$

LCM0.2 with 1 mole, Li	=	1 mole
LCM0.2 0.010302 mole , Li	=	$\dfrac{0.010302 \text{ mole x 1 mole}}{1 \text{ mole}}$
	=	0.010302 mol
g	=	n x MW
	=	0.010302 x 68.94
	=	**0.7102 g**

$Co(NO_3)_2 6H_2O$

LCM0.2 with 1 mole, Co	=	0.8 mole
LCM0.2 0.010302 mole, Co	=	$\dfrac{0.010302 \text{ mole x 0.8 mole}}{1 \text{ mole}}$
	=	0.00824 mole
g	=	n x MW
	=	0.00824 x 291.03
	=	**2.3981 g**

$Mn(NO_3)_2 4H_2O$

LCM0.2 with 1 mole, Mn	=	0.2 mole
LCM0.2 0.010302 mole, Co	=	$\dfrac{0.010302 \text{ mole x } 0.2 \text{ mole}}{1 \text{ mole}}$
	=	0.002060 mole
g	=	n x MW
	=	0.002060×251.01
	=	**0.5172 g**

Citric acid

Citric acid (mole ratio of citrate/nitrate = 1)

Mole nitrate of $LiNO_3$	= 1 x 0.010302 = 0.010302 mole
Mole nitrate of $Co(NO_3)_2 6H_2O$	= 2 x 0.008240 = 0.016480 mole
Mole nitrate of $Mn(NO_3)_2 4H_2O$	= 2 x 0.002060 = 0.004120 mole
Total mole nitrate	= 0.010302+0.016480+0.004120
	= 0.03090 mole
Mole ratio of citrate/ nitrate = 1	
So, Moles of mole citrate	= 0.03090 mole
Weight of citric acid	= n x MW
	= 0.03090 mole x 192.13 g/mole
	= 5.9372 g

2. The calculation of lattice parameters

Bragg's Law $\quad n\lambda = 2d\sin\theta$

Cubic $\qquad \dfrac{1}{d^2} = \dfrac{h^2 + k^2 + l^2}{a^2}$

Tetragonal $\qquad \dfrac{1}{d^2} = \dfrac{h^2 + k^2}{a^2} + \dfrac{l^2}{c^2}$

Orthorhombic $\qquad \dfrac{1}{d^2} = \dfrac{h^2}{a^2} + \dfrac{k^2}{b^2} + \dfrac{l^2}{c^2}$

Hexagonal $\qquad \dfrac{1}{d^2} = \dfrac{4}{3}\left(\dfrac{h^2 + hk + k^2}{a^2}\right) + \dfrac{l^2}{c^2}$

Monoclinic $\qquad \dfrac{1}{d^2} = \dfrac{1}{\sin^2\beta}\left(\dfrac{h^2}{a^2} + \dfrac{k^2\sin^2\beta}{b^2} + \dfrac{l^2}{c^2} - \dfrac{2hl\cos\beta}{ac}\right)$

Triclinic $\qquad \dfrac{1}{d^2} = \dfrac{1}{V^2}\begin{pmatrix} h^2b^2c^2\sin^2\alpha + k^2a^2c^2\sin^2\beta + l^2a^2b^2\sin^2\gamma \\ + 2hkabc^2(\cos\alpha\cos\beta - \cos\gamma) \\ + 2kla^2bc(\cos\beta\cos\gamma - \cos\alpha) \\ + 2hlab^2c(\cos\alpha\cos\gamma - \cos\beta) \end{pmatrix}$

$V = abc\left(1 - \cos^2\alpha - \cos^2\beta - \cos^2\gamma + 2\cos\alpha\cos\beta\cos\gamma\right)^{1/2}$

Hexagonal system

$$\frac{1}{d^2} = \frac{4}{3}\left[\frac{h^2 + hk + k^2}{a^2}\right] + \frac{l^2}{c^2}$$

For example The calculation of the 003 and 104 plane of an hexagonal cell with $d_{003} = 4.6621$ Å and $d_{104} = 2.0001$ Å (B), as shown Figure A-1

From 003 plane

$$\frac{1}{d^2} = \frac{4}{3}\left[\frac{h^2 + hk + k^2}{a^2}\right] + \frac{l^2}{c^2}$$

$$\frac{1}{4.6621^2} = \frac{4}{3}\left(\frac{0^2+0+0^2}{a^2}\right) + \frac{3^2}{c^2}$$

$$\frac{1}{21.7352} = \frac{9}{c^2}$$

c   =   **13.9863** Å (As shown in Figure A-1 (C))

From 104 plane

$$\frac{1}{d^2} = \frac{4}{3}\left(\frac{h^2+hk+k^2}{a^2}\right) + \frac{l^2}{c^2}$$

$$\frac{1}{2.0001^2} = \frac{4}{3}\left(\frac{1^2+0+0^2}{a^2}\right) + \frac{4^2}{c^2}$$

$$\frac{1}{4.0004} = \frac{4}{3}\left(\frac{1}{a^2}\right) + \frac{16}{13.9863^2}$$

a   =   **2.8156** Å (As shown in Figure A-1 (D))
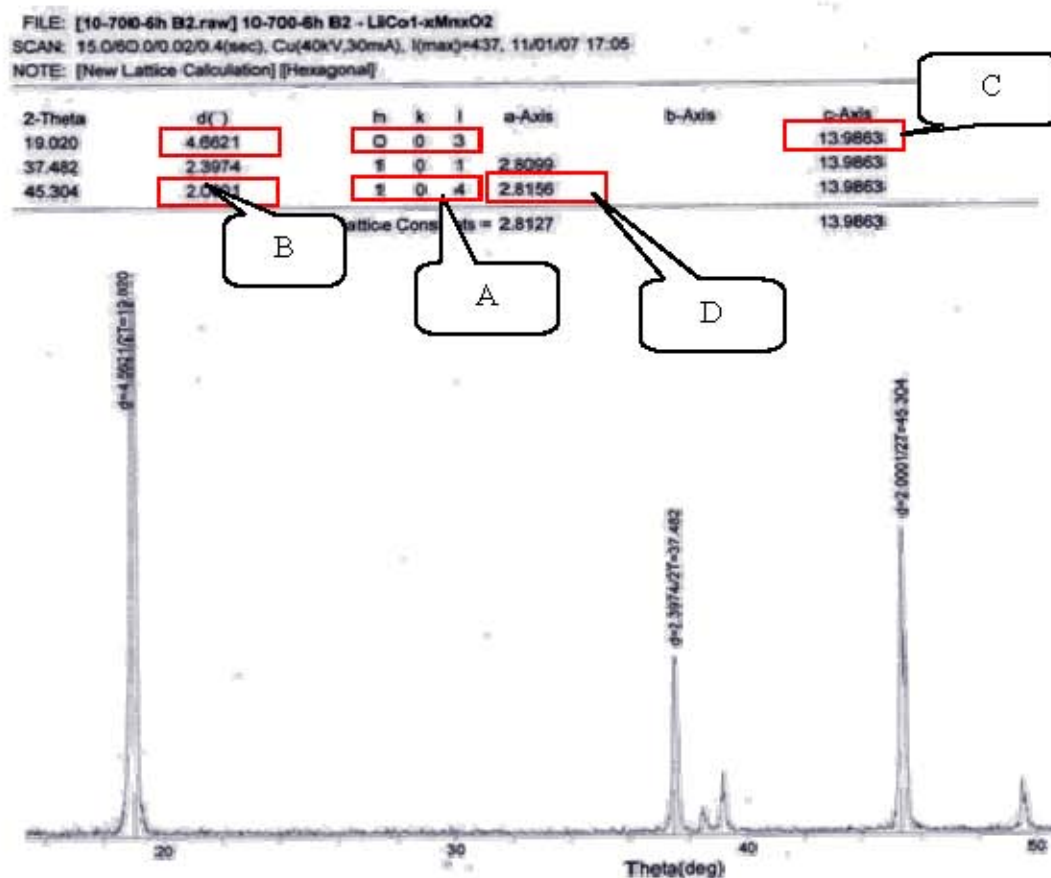
FigureA-1 Calculate lattice constants from locations and miller indices of LCM0.0.

FigureA-2 An example of PDF-file from 50-0653 database.

3. Calculation of d-spacing from TEM technique
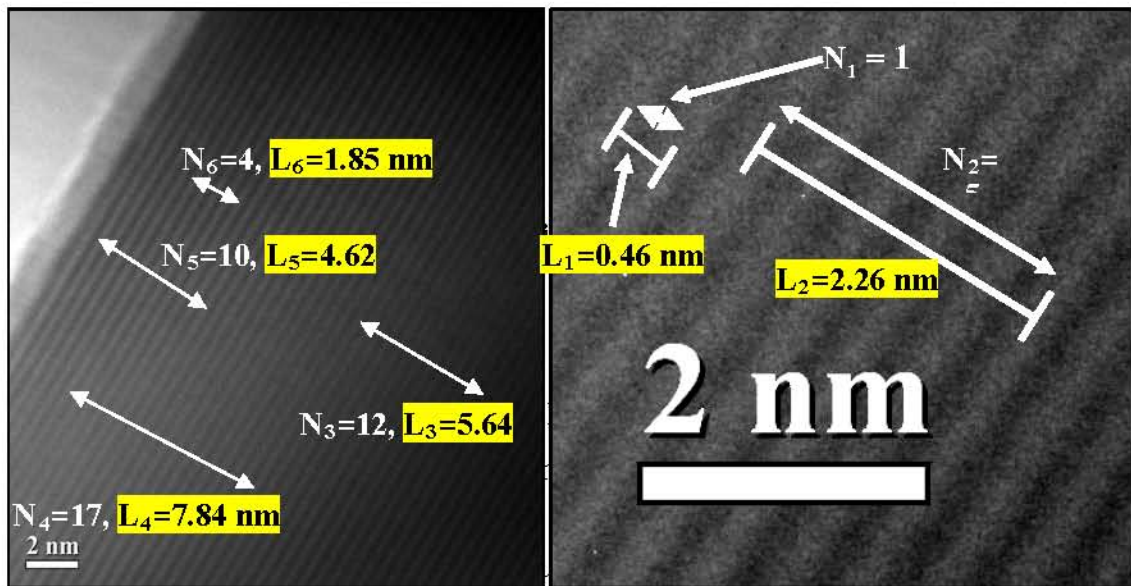
FigureA-3 High resolution TEM image of LCM0.0.

For example LCM0.0-0 from FigureA-3

$$\text{d-spacing average} \quad = \sum_{i=1}^{n} (L_i/N_i)$$

Where
L_i = the length of arrow line (nm)

N_i = Number of spacing between cobalt oxide layers

n = Number of sampling arrow line

Thus, d-spacing average $= \dfrac{(L_1/N_1) + (L_2/N_2) + (L_3/N_3) + \ldots + (L_i/N_i)}{n}$

$= ((0.46/1)+(2.26/5)+(5.64/12)+(7.84/17)+(4.62/10)+(1.85/4)+\ldots+(L_i/N_i))n$

$= (0.4600 + 0.4520+0.4700+0.4618+0.4620+0.4625+\ldots+(L_i/N_i))/n$

d-spacing average $= $ **0.4633 nm**

4. Calculation of Standard deviation

4.1 Standard deviation of crystallite sizes of calcined $LiCoO_2$ at 400 $^{\circ}C$

Table A-2 Crystallite sizes of calcined $LiCoO_2$ samples at 400 $^{\circ}C$

Calcined condition	Crystallite size (nm)*			
	L_{003}	L_{101}	L_{104}	$L_{average}$
400 $^{\circ}C$, 6 h	21.5	21.1	22.3	21.6±0.6
400 $^{\circ}C$, 12 h	23.4	22.5	23.2	23.0±0.5

* The data were calculated, based on the Scherer method by the MDI Jade software.

$$\text{Standard deviation (S.D.)} = \sqrt{\Sigma(x-\bar{x})^2/N\text{-}1}$$

$$\underline{\text{Example}} \text{ S.D. } LiCoO_2 \text{ at } 400\ ^{\circ}C \text{ for 6 h} = \sqrt{\Sigma(x-\bar{x})^2/N\text{-}1}$$

$$= \sqrt{((21.5\text{-}21.6)^2 + (21.1\text{-}21.6)^2 + (22.3\text{-}21.6)^2)/2}$$

$$= \sqrt{((-0.1)^2 + (-0.5)^2 + (0.7)^2)/2}$$

$$\textbf{S.D.} = \textbf{0.6}$$

4.1 Standard deviation of crystallite sizes of LCMx at 700 $^{\circ}C$ for 6 h

Table A-3 The crystallite sizes of LCMx calcined at 700 $^{\circ}C$ for 6 h

Samples	Crystallite size (nm)*			
	L_{003}	L_{101}	L_{104}	$L_{average}$
LCM0.0	66.9	89.8	58.2	71.6±16.3
LCM0.1	39.6	39.8	32.3	37.2±4.3
LCM0.2	26.4	29.4	23.6	26.5±2.9

*The data were calculated, based on the Scherer method by the MDI Jade software.

Example S.D. LCM0.2 $= \sqrt{\Sigma(x-\bar{x})^2/N-1}$

$$= \sqrt{((26.4-26.5)^2 + (29.4-26.5)^2 + (23.6-26.5)^2)/2}$$

S.D. = **2.9**

4.3 Standard deviation of lattice parameters and d-spacings of LCMx calcined at 700 °C for 6 h

Table A-4 Lattice parameters and d-spacings of single-phased $LiCo_{1-x}Mn_xO_2$ calcined at 700 °C for 6 h

Samples	d_{003}(Å)	Lattice parameter (Å)		
		a	*c*	*c/a*
LCM0.0 (1)	4.6621	2.8127	13.9863	4.9726
LCM0.0 (2)	4.6822	2.8141	14.0466	4.9915
LCM0.0 (3)	4.6523	2.8081	13.9569	4.9702
average	4.6655±0.0152	2.8116±0.0031	13.9966±0.0457	4.9781±0.0117
LCM0.1 (1)	4.7065	2.8158	14.1195	5.0144
LCM0.1 (2)	4.7063	2.8128	14.1188	5.0195
LCM0.1 (3)	4.7011	2.8111	14.1034	5.0170
average	4.7046±0.0031	2.8132±0.0024	14.1139±0.0091	5.0151±0.0026
LCM0.2 (1)	4.7016	2.8122	14.1048	5.0158
LCM0.2 (2)	4.7203	2.8155	14.1611	5.0297
LCM0.2 (3)	4.7065	2.8152	14.1034	5.0155
average	4.7095±0.0097	2.8143±0.0018	14.1285±0.0292	5.0202±0.0082

Standard deviation (S.D.) $= \sqrt{\Sigma(x-\bar{x})^2/N-1}$

Example S.D. LCM0.0 $= \sqrt{\Sigma(x-\bar{x})^2/N}$

$$= \sqrt{((4.6621-4.6655)^2 + (4.6822-4.6655)^2 + (4.6523-4.6655)^2)/2}$$

$$= \sqrt{((-0.0034)^2 + (0.0167)^2 + (-0.0132)^2)/2}$$

S.D. = **0.0152**

7.4 Standard deviation of d-spacings of LCMx calcined at 700 $^{\circ}$C for 6 h

Table A-5 the d-spacings of LCMx calcined at 700 $^{\circ}$C for 6 h, analyzed by TEM

Line (sample)	d-spacing (003) of LCMx (nm)		
	LCM0.0	LCM0.1	LCM0.2
L1	0.4615	0.4808	0.4868
L2	0.4688	0.4761	0.4774
L3	0.4615	0.4821	0.4947
L4	0.4701	0.4786	0.4912
L5	0.4615	0.4743	0.5000
L6	0.4615	0.4701	0.4825
L7	0.4743	0.4872	0.4803
L8	0.4615	0.4872	0.4737
L9	0.4513	0.4821	0.4842
L10	0.4615	0.4786	0.4912
Average	**0.4633**	**0.4797**	**0.4862**
S.D.	**0.0063**	**0.0054**	**0.0082**

Example S.D. LCM0.0 $= \sqrt{\Sigma (x-\bar{x})^2/N-1}$

$$= \sqrt{((0.4615-0.4633)^2 + (0.4688-0.4633)^2 + \ldots + (0.4615-0.4633)^2)/9}$$

S.D. = **0.0063**

5. Calculation of oxidation mumber of Mn in LCMx

Table A-6 Chemical composition and oxidation number of Mn in LCMx

Samples	Stoichiometry			Composition	Ox. No. (Mn)
	Li Li/(Co+Mn)	Co Co/(Co+Mn)	Mn Mn/(Co+Mn)		
LCM0.0	1.00	1.00	0.00	$Li_{1.00}Co_{1.00}O_2$	-
LCM0.1	0.98	0.90	0.10	$Li_{0.98}Co_{0.90}Mn_{0.10}O_2$	3.20
LCM0.2	0.97	0.80	0.20	$Li_{0.97}Co_{0.80}Mn_{0.20}O_2$	3.15

Oxidation Number of O = -2, Co = +3, Li = +1

For example Oxidation Number of Mn in LCM0.2

$$(0.97 \times 1) + (0.80 \times 3) + (0.20 \times Mn) + (2 \times (-2) = 0$$
$$(0.97 \times 1) + (0.80 \times 3) + (0.20 \times Mn) = 4$$
$$\textbf{Mn} = \textbf{3.15}$$

6. Calculation of mole proton of HCMx

6.1 Calculate from the residue mole of Li after proton exchange.

For example LCM0.2 = $Li_{0.97}Co_{0.80}Mn_{0.20}O_2$

HCM0.2 = $H_xLi_{0.16}Co_{0.82}Mn_{0.18}O_2$
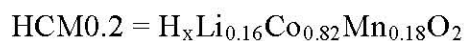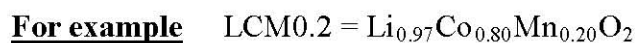
Mole H^+ (x) = mole Li of LCM0.2 - mole Li of HCM0.2

= 0.97 - 0.16

Mole H^+ = **0.81**

6.2 Calculate from oxidation number

For example   HCM0.2 = $H_xLi_{0.16}Co_{0.82}Mn_{0.18}O_2$

$$x \quad = \quad (0.16x1)+(0.82x3)+(0.18x3.15)+(2x(-2))$$

$$= \quad 4 - [0.16 + 2.46 + 0.57]$$

$$= \quad 4 - 3.19$$

Mole H^+ (x) = **0.81**

7. Calculation of percentage mass of HCMx in dispersion phase (Mass-HCMx)

$$\text{Mass-HCMx (\%wt)} \quad = \quad \frac{A - B}{A} \quad x \quad 100$$

Where   A = Weight of HCMx before exfoliation process (0.20xx g)

B = Weight of deposited solid HCMx after exfoliation process

Table A-7 Turbidity of the colloidal suspension of HCMx in TBAOH soluiton

Samples	Turbidity (NTU)						
	0 day	1 day	2 day	3 day	5 day	7 day	10 day
HCM0.1	3765	3495	2900	2980	2415	1610	1440
HCM0.2	7850	7650	6800	6500	5400	4320	2660

Table A-8 Absorbance at λ_{max} of Up-HCM0.1 and Up-HCM0.2

Samples	Absorbance						
	0 day	1 day	2 day	3 day	5 day	7 day	10 day
HCM0.1, 254 nm	0.229	0.220	0.234	0.215	0.177	0.189	0.175
HCM0.2, 244 nm	0.824	0.824	0.829	0.781	0.806	0.739	0.730
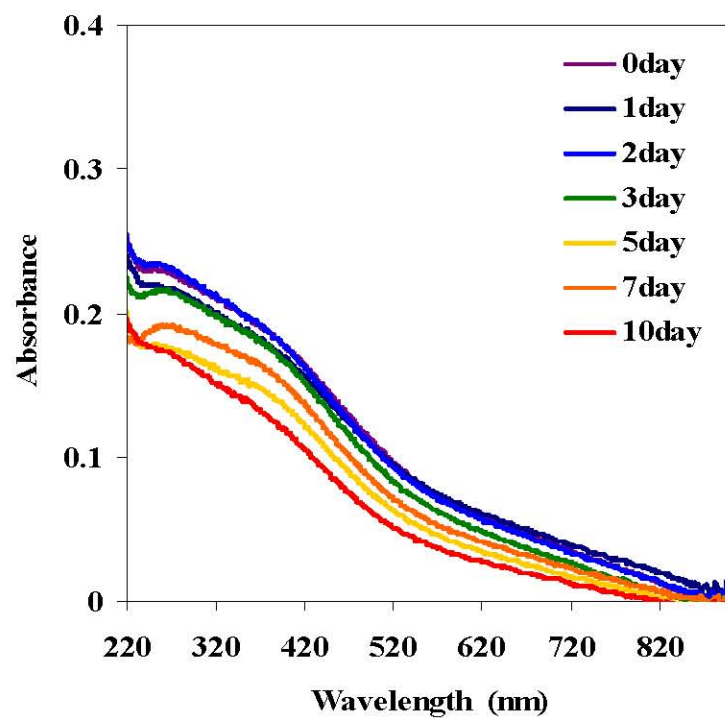
Figure A-4 UV-Vis spectra of the colloidal suspension HCM0.1 with various suspension times.

Figure A-5 UV-Vis spectra of the colloidal suspension HCM0.2 with various suspension times.

Figure A-6 XRD pattern of LCMx-400 and HCMx-400.

Peak Search Report

[LCO13 400 6h.raw] LCO13 400 6h - LiCoO2

SCAN: 15.0/60.0/0.02/0.4(sec), Cu(40kV,30mA), I(max)=196, 08/01/07 02:05

PEAK: 25-pts/Parabolic Filter, Threshold=3.0, Cutoff=0.1%, BG=3/1.0, Peak-Top=Summit

NOTE: Intensity = Counts, 2T(0)=0.0(deg), Wavelength to Compute d-Spacing = 1.54056? (Cu/K-alpha1)

#	2-Theta	d(?)	BG	Height	Height%	Area	Area%	FWHM	XS(?)
1	19.179	4.6239	18	178	100.0	4059	100.0	0.388	215
2	37.282	2.4099	17	64	36.0	1540	37.9	0.409	211
3	38.939	2.3110	16	26	14.6	459	11.3	0.300	298
4	45.262	2.0018	15	136	76.4	3189	78.6	0.399	223
5	49.522	1.8391	13	17	9.6	384	9.5	0.361	252

1:d=4.6239/2T=19.179/100.0%

2:d=2.4099/2T=37.282/36.0%

3:d=2.3110/2T=38.939/14.6%

4:d=2.0018/2T=45.262/76.4%

5:d=1.8391/2T=49.522/9.6%

Two-Theta (deg)

FigureA-7 XRD pattern of LiCoO$_2$ calcined at 400 °C for 6 h.

Peak Search Report

[LCMO10 400C 12h.raw] LCMO10 400C 12h - LiCoO2

SCAN: 15.0/60.0/0.02/0.4(sec), Cu(40kV,30mA), I(max)=214, 08/15/07 19:07

PEAK: 25-pts/Parabolic Filter, Threshold=3.0, Cutoff=0.1%, BG=3/1.0, Peak-Top=Summit

NOTE: Intensity = Counts, 2T(0)=0.0(deg), Wavelength to Compute d-Spacing = 1.540562 (Cu/K-alpha1)

#	2-Theta	d(?)	BG	Height	Height%	Area	Area%	FWHM	XS(?)
1	19.219	4.6143	17	197	100.0	4151	100.0	0.358	234
2	37.319	2.4075	15	76	38.6	1728	41.6	0.387	225
3	39.157	2.2987	15	25	12.7	542	13.1	0.369	238
4	45.418	1.9953	18	128	65.0	2892	69.7	0.384	232
5	49.774	1.8304	12	30	15.2	657	15.8	0.372	244

1:d=4.6143/2T=19.219/100.0%
2:d=2.4075/2T=37.319/38.6%
3:d=2.2987/2T=39.157/12.7%
4:d=1.9953/2T=45.418/65.0%
5:d=1.8304/2T=49.774/15.2%

Two-Theta (deg)

FigureA-8 XRD pattern of LiCoO$_2$ calcined at 400 $^\circ$C for 12 h.

Peak Search Report

[10-700-6h B2.raw] 10-700-6h B2 - LiCo1-xMnxO2

SCAN: 15.0/60.0/0.02/0.4(sec), Cu(40kV,30mA), I(max)=437, 11/01/07 18:05

PEAK: 15-pts/Parabolic Filter, Threshold=3.0, Cutoff=0.1%, BG=3/1.0, Peak-Top=Summit

NOTE: Intensity = Counts, 2T(0)=0.0(deg), Wavelength to Compute d-Spacing = 1.540562? (Cu/K-alpha1)

#	2-Theta	d(?)	BG	Height	Height%	Area	Area%	FWHM	XS(?)
1	19.020	4.6621	3	434	100.0	3997	100.0	0.157	669
2	37.482	2.3974	4	139	32.0	1119	28.0	0.137	898
3	38.482	2.3374	3	18	4.1	143	3.6	0.135	927
4	39.162	2.2984	2	47	10.8	428	10.7	0.155	713
5	45.304	2.0001	2	245	56.5	2574	64.4	0.179	582
6	49.505	1.8397	2	41	9.4	383	9.6	0.159	709
7	59.697	1.5476	6	37	8.5	324	8.1	0.149	831

Peak labels:
1: d=4.6621/2T=19.020/100.0%
2: d=2.3974/2T=37.482/32.0%
3: d=2.3374/2T=38.482/4.1%
4: d=2.2984/2T=39.162/10.8%
5: d=2.0001/2T=45.304/56.5%
6: d=1.8397/2T=49.505/9.4%
7: d=1.5476/2T=59.697/8.5%

Two-Theta (deg)

FigureA-9 XRD pattern of LCM0.0 calcined at 700 °C for 6 h.

Peak Search Report

[91-700-6h B2.raw] 91-700-6h B2 - LiCo1-xMnxO2

SCAN: 15.0/60.0/0.02/0.4(sec), Cu(40kV,30mA), I(max)=369, 11/01/07 18:21

PEAK: 19-pts/Parabolic Filter, Threshold=3.0, Cutoff=0.1%, BG=3/1.0, Peak-Top=Summit

NOTE: Intensity = Counts, 2T(0)=0.0(deg), Wavelength to Compute d-Spacing = 1.540562 (Cu/K-alpha1)

#	2-Theta	d(?)	BG	Height	Height%	Area	Area%	FWHM	XS(?)
1	18.840	4.7063	4	365	100.0	4864	100.0	0.227	396
2	37.421	2.4013	5	108	29.6	1483	30.5	0.233	398
3	39.059	2.3042	5	34	9.3	376	7.7	0.188	529
4	45.200	2.0044	4	195	53.4	3264	67.1	0.285	323
5	49.380	1.8441	3	30	8.2	383	7.9	0.217	454
6	59.540	1.5514	6	26	7.1	447	9.2	0.292	333

Two-Theta (deg)

1:d=4.7063/2T=18.840/100.0%
2:d=2.4013/2T=37.421/29.6%
3:d=2.3042/2T=39.059/9.3%
4:d=2.0044/2T=45.200/53.4%
5:d=1.8441/2T=49.380/8.2%
6:d=1.5514/2T=59.540/7.1%

FigureA-10 XRD pattern of LCM0.1 calcined at 700 °C for 6 h.

Peak Search Report

[82-700-6h B2.raw] 82-700-6h B2 - LiCo1-xMnxO2

SCAN: 15.0/60.0/0.02/0.4(sec), Cu(40KV,30mA), I(max)=244, 11/01/07 18:38

PEAK: 23-pts/Parabolic Filter, Threshold=3.0, Cutoff=0.1%, BG=3/1.0, Peak-Top=Summit

NOTE: Intensity = Counts, 2T(0)=0.0(deg), Wavelength to Compute d-Spacing = 1.540562 (Cu/K-alpha1)

#	2-Theta	d(?)	BG	Height	Height%	Area	Area%	FWHM	XS(?)
1	18.859	4.7016	5	239	100.0	4508	100.0	0.321	264
2	37.455	2.3991	6	81	33.9	1441	32.0	0.302	294
3	39.138	2.2998	6	17	7.1	169	3.7	0.159	682
4	45.200	2.0044	4	133	55.6	2953	65.5	0.377	236
5	49.320	1.8462	2	19	7.9	417	9.3	0.351	260
6	59.458	1.5533	5	19	7.9	463	10.3	0.390	243

Peak labels:
1:d=4.7016/2T=18.859/100.0%
2:d=2.3991/2T=37.455/33.9%
3:d=2.2998/2T=39.138/7.1%
4:d=2.0044/2T=45.200/55.6%
5:d=1.8462/2T=49.320/7.9%
6:d=1.5533/2T=59.458/7.9%

Two-Theta (deg)

FigureA-11 XRD pattern of LCM0.2 calcined at 700 $^{\circ}$C for 6 h.

VITAE

Mr. Karuna Nonthawissarut was born on June 5, 1982 in Loei, Thailand. He graduated with Bachelor's Degree in General Scinece from Faculty of Liberal Art and Science, Kasetsart University in 2005. He continued his study in Petrochemistry and Polymer Science Program, Faculty of Science, Chulalongkorn University in 2006.

PRESENTATIONS

11 - 12 Sep 2008

Poster Presentation "Synthesis and Characterization of Nano-size $LiCO_{1-x}Mn_xO_2$ Powers Prepared by Sol-gel Method" The 10nd National Graduate Research Conference, Sukhothai Thammathirat University, Nonthaburi.

18 - 19 Jun 2008

Poster Presentation "Preparation of Colloid and Thin Film of Layered doped Cobalt Oxide" The 2nd Joint Symposium Between Yonsei University, Korea and Chulalongkorn University, at Yonsei University, Korea.

22 - 25 Apr 2008

Poster Presentation "Preparation of Colloid and Thin Film of $LiCo_{1-x}Mn_xO_2$" The smart/intelligent materials and nanotechnology 2008 (SmartMat'08), Chiang Mai University, Chiang Mai

His present address in 87/7 Tambon Nongkhun, Ampoe Phuluang, Loei, 42230 Tel; 042-879103, Mobile: 084-927-0690, E-mail : karuda262@hotmail.com.